Fatigue Sensitivity of Monopile-supported Offshore Wind Turbines

by

Ramtin Rezaei

Supervised by:

Dr Philippe Duffour

&

Dr Paul Fromme

A Dissertation Submitted in Partial Fulfilment of the Requirements for the

Degree of Doctor of Philosophy

in

Department of Civil, Environmental and Geomatic Engineering

University College London (UCL)

[2017]

Declaration

I, Ramtin Rezaei, confirm that the work presented in this thesis is my own. Where information has been derived from other sources, I confirm that this has been indicated in the thesis.

Signature:

Date: 07.03.2017

Abstract

Offshore wind energy is increasing in the UK to meet renewable energy targets. A literature review on the most commonly used offshore wind turbine support structures (i.e. monopiles) has been compiled. The dynamic behaviour of offshore wind turbines is highly dependent on the stiffness and damping. Scour and damping have been researched recently, but their long-term influence on the fatigue life are not completely understood. This research aims to better understand their effect using finite element (FE) simulations.

The influence of soil-structure interaction was studied using beam element and 3D solid element models and a good agreement was found. The natural frequency and dynamic amplification of the wind turbine were found to be sensitive to soil stiffness. The influence of the transition piece on the offshore wind turbine was examined using 3D models, and its effect on the static and dynamic responses was found to be minor.

A full fatigue analysis was performed using a combination of different simulation packages (TurbSim, FAST, ABAQUS and MATLAB). Damping and operational regime influences were studied using time-domain implicit dynamic analysis of beam element models. The fatigue life of the non-operational turbine was found to be significantly lower than the operational turbine. Almost linear increase in the fatigue life of operational turbines was observed with increasing damping. In addition, a simplified method to predict the fatigue life for variations in the damping was proposed.

Scour and backfilling influences were studied using the beam element model. The magnitude and location of the maximum bending moment changed depending on the scour level. The modal properties experienced minor changes, while fatigue life showed a considerable reduction. The backfilling process led to the recovery of the first natural frequency. However, fatigue life recovery was dependent on the backfilling timing. Finally, it was demonstrated that fatigue life variations due to scour could be predicted from the static response of offshore wind turbines.

Impact Statement

This research investigated the influence of key parameters, such as damping and scour, on the fatigue life of offshore wind turbine structures in operation. In addition, the influence of some of the commonly applied methods for modelling the soil-structure interaction and the transition piece on the stiffness, stress, and modal properties were studied, giving an insight into the possible influence of their application in the fatigue design of offshore wind turbines in practice.

The uncertainties in the design of offshore wind turbines are mostly compensated by over-conservatism in practice. This research aimed to fill the gap in our knowledge of the damping and scour effects on the fatigue life of offshore wind turbines in operation. The significant increase of fatigue life for increased damping levels was calculated, allowing quantification of the benefits of added damping in practice. The insight given can set a benchmark for the researchers and designers to consider and assess possible design optimisations from added damping in offshore wind turbines. The proposed simplified fatigue analysis method can be employed to save a significant amount of computational costs and time to evaluate the effects of damping variations at the early stages of the design.

In addition, this research gave an insight into the influence of scour variation on the fatigue life of wind turbines in operation. The quantification of the influence of natural or artificial backfilling of the scour hole on the fatigue life of wind turbines gives the designers the chance to realise the possible benefits of considering this option in practice. The proposed approximate fatigue analysis method, which takes a fraction of the time and computational effort required for the time-domain fatigue analyses, can be implemented in practice to assess the remaining fatigue life or the possible life extension from backfilling.

Acknowledgements

I am very grateful to my supervisors, Dr Philippe Duffour and Dr Paul Fromme, for their support and valuable advice over the course of my research. I would like to thank them for encouraging my research and for allowing me to grow as a research scientist.

I am very thankful to my parents, Negar and Sassan, for their unconditional love, continuous patience and endless support through my difficult times. Without their love, this research would have not been made possible.

I would like to thank my girlfriend, Kimia, who has been an inspiration to me, for her boundless love, patience and support. Kimia never stopped believing in me and stayed right beside me at every step of the way.

I have deep appreciation for Dr Pedro Ferreira for being available for discussion and his contribution to my research.

At last, I would like to thank all my friends and colleagues who supported me in every possible way and made my days more enjoyable.

Table of Contents

List of Figures

12

List of Tables

1 Introduction

1.1 Offshore wind

Oil and gas have dominated the power generation industry for decades as one of the most useful and widespread means of providing energy. However, the environmental impact associated with greenhouse gases emissions has emphasised the dangers of an excessive dependence of human beings on fossil fuels. Therefore, alternative clean energy supplies are vital for the future. One of these alternatives is large-scale wind-powered energy production, which started onshore and has more recently been exploited offshore. Large-scale developments of offshore wind turbines began about two decades ago, mostly off the coasts of north European countries (Gaudiosi, 1999). The interest in offshore wind was due in part to the stronger wind resource at sea. Land saturation and the almost inevitable resistance of local residents to onshore wind farms are also considered key factors (Halfpenny, 1998; Gaudiosi, 1999; Adhikari and Bhattacharya, 2011; Esteban *et al.*, 2011). As a result, offshore wind has become one of the fastest growing industries in the energy sector in the world. Europe has focused extensively on the development of offshore wind energy, to the extent that almost 90% of the largest offshore wind farms in the world are located in Europe (Kaldellis and Zafirakis, 2011; Sun, Huang and Wu, 2012). The UK is one of the leading countries in this field. Figure 1-1 shows the distribution of installed offshore wind power capacity in Europe.
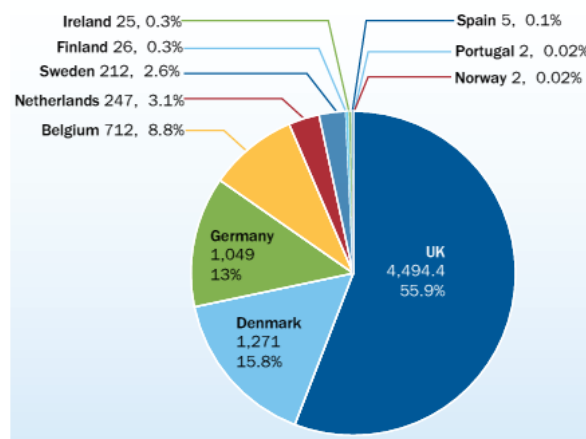
Figure 1-1. Cumulative installed offshore wind capacity (MW) in Europe (Corbetta *et al.*, 2015)

With the increasing focus on offshore wind power, there has been a constant tendency towards larger wind turbines to maximise production. This is evident in Figure 1-2, which shows the evolution of wind turbines' size in the past decades. As a result, there is a constant need for larger support structures to resist the higher environmental loads on the offshore wind turbines, which creates challenges in their construction, installation, operation and maintenance.
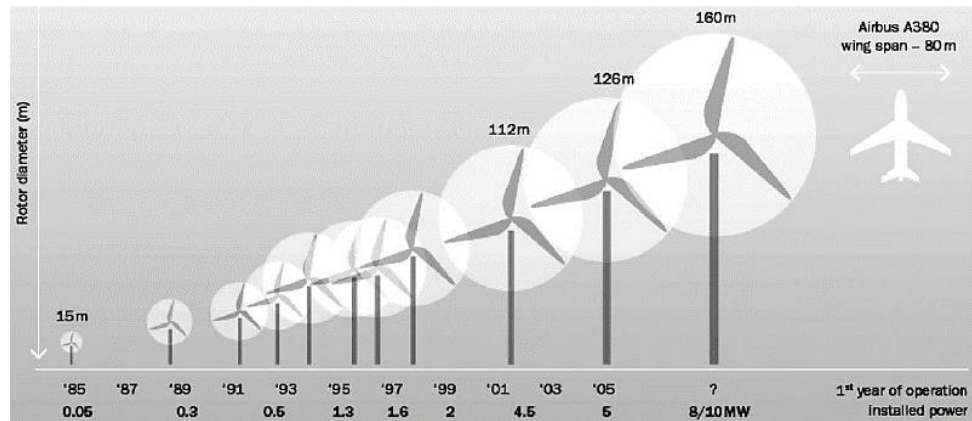
Figure 1-2. Evolution of wind turbines' size (Bilgili, Yasar and Simsek, 2011)

Moving wind generation technology offshore has proven to be challenging. The offshore wind energy industry has evolved from the experience gained from offshore oil and gas industry and onshore wind turbines to tackle the challenges involved in developing offshore wind production. Offshore wind is comparatively new and the differences between wind turbines and oil and gas structures required adapting the experiences from oil and gas to fully meet the needs of the offshore wind industry. For instance, offshore wind turbines are significantly lighter structures than oil and gas platforms and the ratio of the lateral to vertical loads is higher for offshore wind turbines.

Similar to oil and gas platforms, the support structure of offshore wind turbines are extremely vital components in their design, as damage or failure of them can lead to the loss of the complete wind turbine. The majority of offshore wind turbines (more than 75%) have been installed on monopiles so far (Corbetta *et al.*, 2015). The slenderness of monopile-supported offshore wind turbines, combined with the highly dynamic nature of the offshore environment have resulted in structures which must be carefully designed against dynamic and fatigue failures. Their dynamic response is sensitive to changes in stiffness, inertia and damping of the system. As the fatigue depends on the range of stresses experienced during the system's life, factors that change these ranges can in turn lead to a different fatigue life than that designed for.

There are numerous uncertain factors in the design of offshore wind turbines, such as scour and damping, which lead to uncertainties in their fatigue design. These uncertainties are usually compensated by conservatism in practice. However, a more in-depth understanding of the fatigue life sensitivity to these factors could lead to a less conservative and yet, safe fatigue design for offshore wind turbines.

1.2 Research objective

The objective of this research is to investigate the long-term fatigue performance of offshore wind turbines mounted on monopile by studying in some detail the factors that affect its dynamic

behaviour. To this end, an integrated finite element analysis of monopile-supported offshore wind turbines was developed and used to systematically evaluate the influence of various factors such as damping, turbine operational regime and scour.

1.3 Thesis structure

Chapter 2 offers first a general overview of offshore wind turbine support structures, focussing later on monopile foundation. A basic description of monopile-supported wind turbines and their characteristics is presented. This is followed by a literature review of the factors affecting their dynamics. These factors include soil-structure interaction, transition piece, damping, and scour effects. Finally, an overview of various studies on the fatigue influences of damping and scour is given. Chapter 3 describes the reference offshore wind turbine used as well as the methodology followed to study its fatigue life. A full description of the finite-element modelling process and an outline of the environmental loads and fatigue damage calculation methods used are provided. In Chapter 4, results are presented from a set of sensitivity analyses on the effects of soil-structure interaction on the static response and modal properties of the reference wind turbine using p-y curves and 3D soil-block models. This is followed by a similar sensitivity analysis for the 3D finite element models of the transition piece in Chapter 5. In both chapters, the effects of nonlinearities, such as surface interactions and material plasticity in the models, are thoroughly discussed and some conclusions drawn. Chapter 6 presents the study of fatigue life sensitivity to the turbine operational regime and damping present in the system. This is followed by the proposal of an approximate method for the calculation of fatigue life, which can be used to quickly assess the fatigue life variations for various damping levels. Chapter 7 provides the analysis of the fatigue life in the presence of various levels of scour/backfilling. The scour levels are determined based on typical and recommended scour levels that could occur during the service life of offshore wind turbines. Similar to Chapter 6, an approximate method for the prediction of fatigue life is proposed. The conclusions on the observations arising from the analyses are provided in Chapter 8. This is followed by a critical review of the results and recommendations for further work in Chapter 9.

2 Literature Review

2.1 Support structures

Offshore structures can be categorised into bottom-supported (i.e. fixed) and floating structures. Water depth is one of the determinant factors that controls the decision on the type of support structure. Floating structures are considered to be more suited for deeper waters. In general, floating structures are either naturally or positively buoyant (Chakrabarti, 2005). Floating structures have been used extensively in the oil and gas industry, but this support configuration is still at the research and development stage in the wind sector (Musial, Butterfield and Boone, 2004; Collu, Brennan and Patel, 2014). One of the main issues regarding floating offshore wind turbine structures is that the structure should provide enough buoyancy not only to support the weight of the structure, but also to counteract the roll, pitch and yaw motions produced by the large lateral wind loading. Floating wind turbines are currently an active field of research and prototypes have been built and tested at sea (Saleem, 2011; Collu, Brennan and Patel, 2014). However, it is unlikely they will be deployed on a large scale in the short-to-medium term, especially as the size of wind turbines keeps increasing (Henderson and Vugts, 2001; Saleem, 2011).

Fixed offshore structures can be kept in place by friction (gravity-base), piling or suction to the seabed. Gravity-base structures principally rest on the seabed and are stabilised by the friction force produced by their weight at the seabed. There are different types of piled structures (e.g. jackets, monopiles, tripiles and tripods) as illustrated in Figure 2-1.

Jackets are the most commonly used type of structure for oil and gas platforms (Chakrabarti, 2005). With the increasing size of wind turbines and exploration of offshore wind in deeper water, jackets may also become more common in the offshore wind industry.
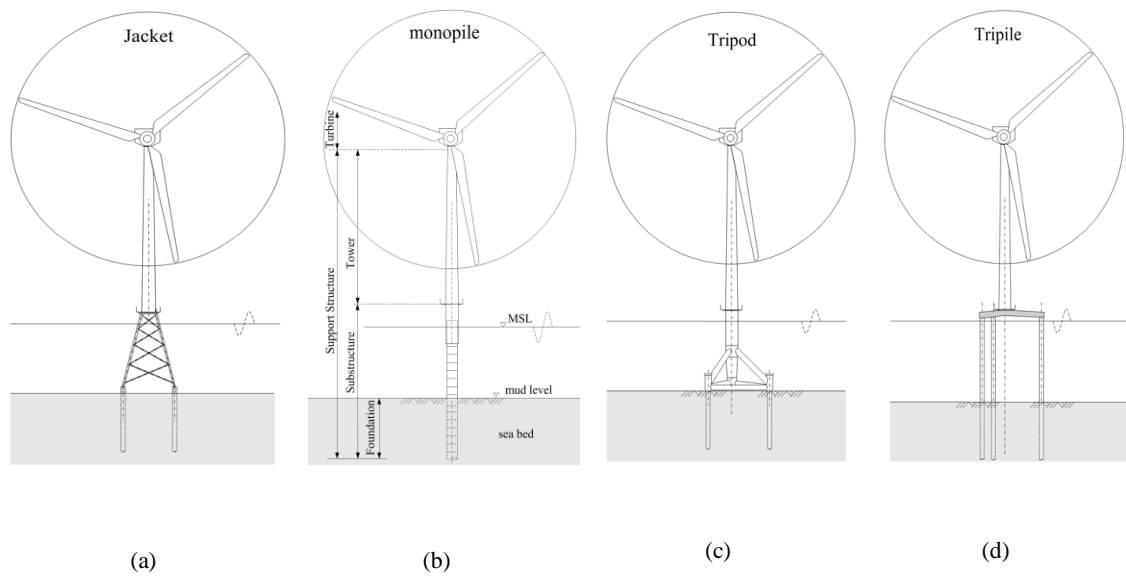
Figure 2-1. Bottom-supported offshore wind support structures; (a) jacket, (b) monopile, (c) tripod, and (d) tripiles (Schaumann, Lochte-Holtgreven and Steppeler, 2011)

To date, monopiles have by far been the most economical, environmentally friendly and, hence, commonly used support structure for offshore wind turbines (Malhotra, 2010; Lozano-Minguez, Kolios and Brennan, 2011; Matutano *et al.*, 2013). They are essentially large cylindrical steel tubes driven into the seabed. A monopile-supported wind turbine consists of a monopile, which is partly underground, the J-tube that supports cabling for power transmission, and above water, the transition piece that connects the monopile to the turbine tower, access platform as well as the rotor nacelle assembly. Figure 2-2 illustrates these components.

Figure 2-2. Different components of a typical offshore wind turbine mounted on monopile foundation (Sheppard and Puskar, 2011)

The main advantage of monopiles, compared to other supporting structures, is in their simplicity, which means that they are relatively inexpensive, quick to design, fabricate and install (Schaumann and Böker, 2005). Their main drawback (from the structural point of view) is their slenderness, which results in high flexibility. Monopiles are mostly used for 0-30m of water depths (Kurian and Ganapathy, 2010). At deeper water, the height of the support structure needs to be increased. However, increasing the height also tends to increase the vibration period of the structure. To provide a higher stiffness, larger diameter piles are used. Also, the increasing size of wind turbines requires larger monopiles. Larger monopiles can be designed without much difficulty but installing such large pieces in water deeper than 30m presents challenges. However, this seems to be the preferred option in the near-to-mid-term (Seidel, 2014). There is a significant amount of interest from industry and academia in the short and long-term performance of monopile-supported offshore wind turbines. Accordingly, this research concentrates on monopile-supported offshore wind turbines. The following section gives an overview of the design of monopiles according to the commonly used DNV design recommendations.

2.2 Design limit states

Design limit states are the requirements that must be met to ensure the safety and functional use of a structure during its design life. Offshore wind turbines are designed to be in service for 20-25 years (Bhattacharya, 2014). Their design limit states are adapted from oil and gas guidelines. DNV (2013) suggests that all components in offshore wind turbines must be designed for ultimate, fatigue, accidental and serviceability limit states. In ultimate limit state, offshore wind turbines must be able to resist extreme environmental loads with 50 or 1-year return period, depending on the load case. Accidental limit state ensures the safety and integrity of offshore wind turbines due to impact loads such as ship or ice impacts. The effects of excessive operational deflections are investigated in the serviceability limit state. In practice, one of the main structural design criteria is the permanent pile rotation at the seabed which is considered to be limited to $0.5°$ to ensure a safe serviceable life (Achmus, Kuo and Abdel-Rahman, 2009). Fatigue limit state requires the accumulated damage in monopiles to be checked against operational and non-operational wind and wave load time histories in order to ensure the fatigue life for the structure is longer that the design life.

In a drive to compete with other renewable energy sources, the offshore wind industry continuously aims to create safe and cost-effective solutions. Therefore, further research is needed to better understand the uncertainties in offshore wind turbines' design so that they can be delivered more cost-effectively without compromising their safety. In addition, from the practical point of view, the establishment of simplified design procedures, which could be used at an early design stage, is important for the wind energy industry as various modifications (e.g. changing

the turbine size and support structure type) can occur during the development phase of the project (Arany *et al.*, 2017).

2.3 Dynamics of offshore wind turbines

Monopile-supported wind turbines are subjected to complex dynamic loads, so a detailed analysis of their dynamics is critical to ensuring the serviceability and fatigue limit states have been met. Like any (linear) dynamics system, the response of offshore wind turbines depends on the relative position of their natural frequencies with respect to the forcing frequencies. The main dynamic forces on the offshore wind turbine structure are:

- Dynamic environmental loads, such as wind and wave, that are random in nature.
- Rotor load which is commonly known as 1P. The frequency of this load is dependent on the rotational frequency of the rotor.
- Blade-passing loads which is caused by the motion of the blades passing the tower and is dependent on the number of blades. This is commonly referred to as 2P for 2-bladed or 3P for 3-bladed wind turbines respectively.

Design guidelines for offshore wind turbines recommend that the natural frequency of the wind turbine be away from these forcing frequencies by a margin of 10% (Det Norske Veritas, 2013). Figure 2-3 shows an example plot of the spectral densities of the relevant forcing frequencies and the possible positions for the fundamental natural frequency of the system.
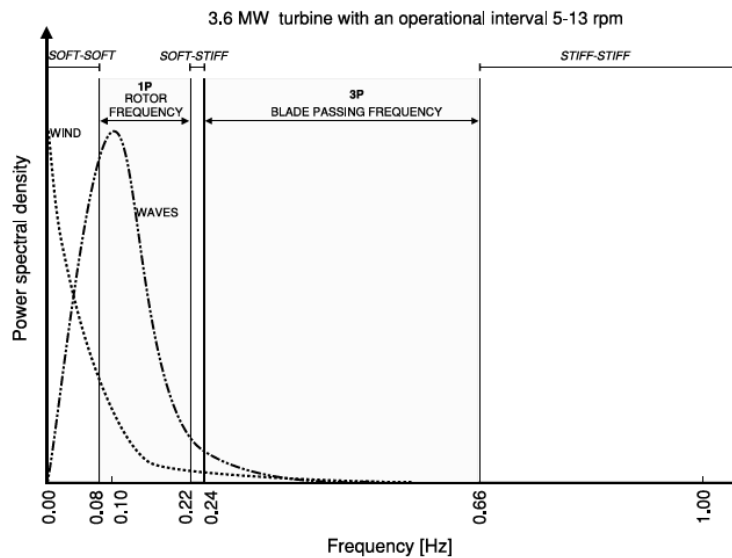
Figure 2-3. Power spectral density of the forcing frequencies and the possible positions for the natural frequency of an example 3.6 MW wind turbine (Lombardi, Bhattacharya and Muir Wood, 2013).

The first natural frequency of a monopile-supported wind turbine is typically in the range of 0.1Hz to 1Hz, which overlaps with the range of frequencies associated with the wind, waves, rotor (1P) or blade passing frequencies (2/3P) as shown in Figure 2-3 (Bhattacharya, Lombardi and Muir

Wood, 2011). As can be seen in Figure 2-3, the allowable frequencies leave the designers with the following design strategies: soft-soft, soft-stiff and stiff-stiff approach. Soft-soft design is the most cost-effective by using the least amount of material, however, it comes with the risk of resonance due to wave loads (Tempel, 2006). The soft-soft approach results in a fairly flexible structure while the stiff-stiff approach leads to a stiffer structure, but it tends to use more material and be more expensive to build. Monopile wind turbines are commonly designed to be in the soft-stiff region (Lombardi, Bhattacharya and Muir Wood, 2013). The soft-stiff design strategy balances the stiffness of the wind turbine with the associated costs for construction and is more cost-effective than the stiff-stiff approach (Bhattacharya *et al.*, 2013). From the design point of view, the constant increase in the size of offshore wind turbines creates the following challenges: longer monopiles and towers, larger top-masses, lower rotor and blade passing frequencies (Tempel, 2006). The 1P rotational frequency of a wind turbine is given by Equation (2-1).

$$f_{1P} = \frac{\lambda V_w}{\pi D_{rotor}}, \qquad (2\text{-}1)$$

where λ is the tip speed ratio, V_w is the wind speed and D_{rotor} is the rotor diameter. As can be seen, f_{1P} is inversely proportional to the rotor diameter, so larger wind turbines, due to their increased structure and turbine size, possess natural and rotor frequencies that are closer to wind and wave loads, thereby increasing the dynamic response of the system.

To design the system adequately, its natural frequencies must be determined. Tempel and Molenaar (2002) proposed idealising the monopiles and tower as a fixed-base cantilever beam with a lumped mass on top for preliminary assessment. From these assumptions, the first natural frequency can be estimated using Equation (2-2):

$$f_{nat} \cong \frac{D_{av}}{L^2} \sqrt{\frac{E}{104(a+0.227)\rho_{steel}}}, \qquad (2\text{-}2)$$

where D_{av} is tower average diameter, ρ_{steel} is the density of steel, generally taken as 7850 kg/m³, L is the tower length and a is $\frac{M}{\rho_c \pi D_{av} t L}$, where M is the top mass and t is the tower wall thickness.

The simple approach suggested by Tempel and Molenaar (2002) was further developed by Adhikari and Bhattacharya (2011, 2012) to take into account the effects of foundation flexibility. They modelled the monopile-supported wind turbine as an Euler-Bernoulli beam with a concentrated mass at the top, which was supported on an elastic soil modelled by lateral and rotational springs, and found an approximation of the fundamental natural frequency defined by Equation (2-3):

$$\omega_1 \approx c_0 \sqrt{\frac{3\gamma_k}{\alpha+\gamma_m}}, \tag{2-3}$$

where $c_0 = \sqrt{\frac{EI}{mL^4}}$, m is turbine mass, γ_k is the stiffness correction factor defined as $\frac{k_e}{k_{CL}}$, where k_e is the equivalent stiffness of the first mode of the monopile and k_{CL} is $\frac{3EI}{L^3}$, γ_m is a mass scaling parameter found by solving the dynamic equation of motion of the monopile. These approximate methods are mainly oriented towards preliminary design. Finite element analysis including a more realistic foundation flexibility and mass distribution along the system is required in practice for an accurate dynamic analysis of offshore wind turbines.

Offshore wind turbines support structures represent approximately a third of the total planning and commissioning cost of the wind turbines, including transportation and installation costs (Bakmar, 2009). As explained, a proper prediction of the dynamic response of wind turbines is critical to their design. Failure of individual components, such as the foundation support, transition piece, rotor and blades, could have a considerable effect on the dynamics of the wind turbine. Therefore, the global integrity of the structure depends on the health of different structural components. Dynamics and vibration of offshore wind turbines are driven by their inertia, damping and stiffness, which can also affect their fatigue life. The following sections provide an overview of the literature on the current knowledge of these parameters.

2.4 Inertia

Inertia in offshore wind turbines is fairly easily characterised from the materials and dimensions. In a typical 5MW wind turbine, the monopile weighs around 600 tons, while an 80m tower has a mass between 200-400 tons and the nacelle assembly can weigh around 350 tons (BVG Associates, 2010). However, exact values are dependent on the detailed dimensions. Over the life of the structure, marine growth on the submerged section of the monopile adds to the overall mass of the structure (Carswell, 2012). This is usually taken into consideration by increasing the density of the submerged part of the monopile in their design.

2.5 Damping

According to Petersen et al. (2010), the overall damping in offshore wind turbines is comprised of aerodynamic, hydrodynamic, structural and soil damping, and supplemental damping from damping devices such as tuned mass dampers. For fatigue calculations, the contribution of each damping source is considered and added to form an overall damping factor for the wind turbine at a given mode, which is typically expressed as a percentage of critical damping. Aerodynamic damping is the highest contributor to the overall damping for the fore-aft modes (front to back plane) when the turbine is in operation. However, its contribution drops significantly when the

turbine is idle. The overall damping in a parked offshore wind turbine consists of the structural, hydrodynamic and soil damping. Also, aerodynamic damping affects the side-side modes only slightly. Shirzadeh et al. (2013, 2015) found a good agreement between onsite measurements of overall damping ratios and numerical simulation results using the HAWC2 aeroelastic code and reported 1.05% damping for the fore-aft bending mode and 1.27% for the side-side bending mode in a non-operational turbine. Damping was measured through two types of tests in the work of Shirzadeh et al. (2013): an over-speed stop test of a wind turbine and ambient excitation measurements where the wind turbine is rotating very slowly. Shirzadeh et al. (2013, 2015) concluded that estimating the damping in operational conditions and the effects of various elements such as wind speed on the overall damping and dynamics of the offshore wind turbine should be the subject of further investigation. On-site measurements by El-Kafafy et al. (2014) and Devriendt et al. (2012) also showed total damping values in agreement with the results of Shirzadeh et al. (2013) in parked conditions. Hansen et al. (2006) and Koukoura, Natarajan and Vesth (2015) measured the aerodynamic damping in offshore wind turbines mounted on monopiles in operation. They measured approximately 8% of total damping (ζ) in the fore-aft mode, which included the effects of a passive tower damper. However, Hansen et al. (2006) concluded that experimental measurement of aerodynamic damping is difficult as it varies with blade pitch, which changes with wind speed.

Salzmann and Tempel (2005) theoretically investigated aerodynamic damping in operation. In their study, a theoretical approach was developed specifically for frequency-domain simulations to match the results of time-domain analysis of variable speed offshore wind turbines. It was shown that at low wind speeds, constant rotor speed turbines show higher damping than variable speed turbines. However, at high wind speeds the opposite was shown. A similar drop in the aerodynamic damping was seen in both turbine types at the rated wind speed, as changes in wind speed causes smaller variations in the wind thrust. Valamanesh and Myers (2014) used numerical simulations with FAST to estimate both operational and non-operational aerodynamic damping levels. They showed that aerodynamic damping is variable within the turbine operational range and was found to lie mostly in the range of 2% to 8% of critical damping depending on the wind speed, and the size and operation of the wind turbine.

Apart from the aerodynamic damping, soil damping is the next most significant contributor to the total damping in offshore wind turbines. However, direct estimation of soil damping in practice is difficult due to the complexities in the soil behaviour and uncertainties in site characterisation (Fontana *et al.*, 2015; Koukoura, Natarajan and Vesth, 2015). The presence of soil damping is especially important as it could reduce fatigue damage in the side-side direction (Damgaard *et al.*, 2015; Fontana *et al.*, 2015). Tarp-Johansen et al. (2009) used numerical simulations to show that approximately 1% of critical damping is present in the offshore wind turbine due to soil damping.

This value is in agreement with the estimated and measured 0.53% to 1% by Germanischer Lloyd as stated by Carswell et al. (2015). Carswell et al. (2015) further showed that the mudline bending moment during an extreme wind and wave event is decreased by 7-9% due to added soil damping, which may have significant fatigue reduction implications. By contrast, Versteijlen et al. (2011) suggested a higher value of 1.5% for soil damping according to on-site measurement of a test pile.

Structural and hydrodynamic damping have been reported to be relatively smaller than the aerodynamic and soil damping. Approximately 0.2% of critical damping is typically reported for structural steel based on offshore oil and gas industry and onshore wind experience. Damping from grouted connections can add to this value. Arany et al. (2016) suggests that it could increase to 1.5% depending on the connection details, however, no exact approximation exists in the literature. Tarp-Johansen et al. (2009) reported 0.25% of hydrodynamic damping which was estimated using WAMIT (Wave Analysis MIT) for a 4.7m diameter monopile. The suggested values by Arany et al. (2016) are also in good agreement with Tarp-Johansen et al. (2009).

In summary, in most studies, an overall damping of 1-2% is a common figure for a parked offshore wind turbine, which is a combination of hydrodynamic, structural and soil damping. However, separate studies on soil damping effects reported slightly higher foundation damping. In an operational offshore wind turbine, the aerodynamic damping is reported to be between 2% to 8% depending on the wind speed and turbine size. This leads to a range of 3% to 10% for the total damping in an operational wind turbine, which can have significant fatigue implications.

2.6 Soil-structure interaction

Monopiles are driven into the seabed in order to support the tower, nacelle and blades. The surrounding soil provides the necessary resistance through compression, shear and friction at the interface with the pile.

Soil resistance is important in three different conditions. Primarily, the soil provides the wind turbine structure with sufficient bearing capacity and lateral resistance, which prevents sinking of the monopile under gravity loads and permanent leaning of the wind turbines due to environmental loads respectively. This aspect is purely geotechnical and is not in the scope of this research. Secondly, dynamically, the soil has a finite, nonlinear stiffness, which has a strong influence on the dynamic behaviour of the system. This leads to difficulties in the prediction of dynamic properties of the wind turbine support structure (i.e. natural frequencies, damping). Finally, the cyclic nature of the environmental loads causes a secondary long-term effect on the soil behaviour, which leads to additional changes to the dynamic properties of the wind turbine structures. Idealisation of the soil behaviour in the long term and under different loading conditions is a complex task. The current guidelines for monopile design are based on the experience of the oil and gas industry. The nature of wind turbine loading has made the relevance

of these guidelines questionable. This is due to the significantly larger piles used for offshore wind turbines which are under dominant and highly dynamic lateral loads, as opposed to the gravity dominated loading of the oil and gas structures. Accordingly, the dynamic nature of the loads, low stiffness and high slenderness of monopiles brings challenges in the design of offshore wind turbines. To date, the standard practice to take into account the effect of soil-structure interaction on the dynamic behaviour of the monopile-mounted turbines is to include layer-by-layer discretised horizontal springs along the embedded length of the monopile. These springs usually have a nonlinear stiffness which is given by so-called p-y curves, as shown in Figure 2-4 (Van Buren and Muskulus, 2012; Sørensen and Ibsen, 2013).
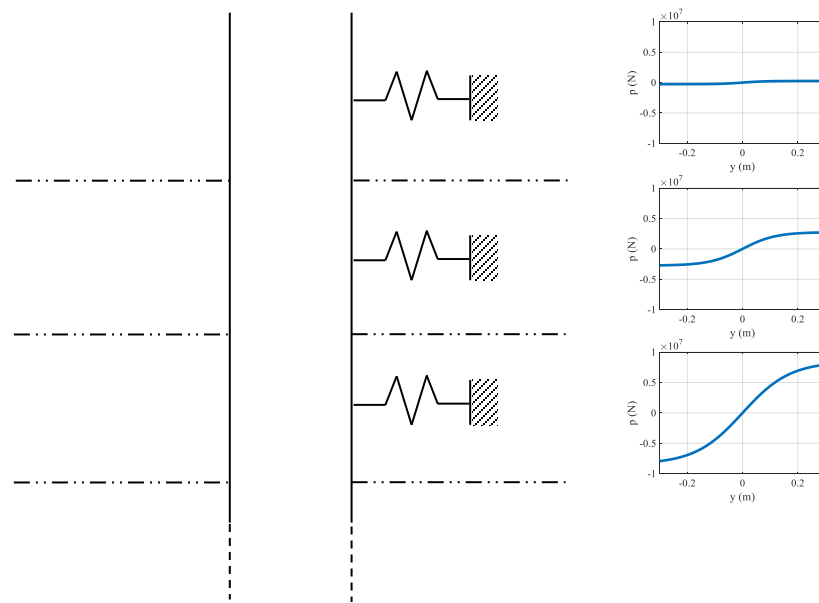
Figure 2-4. An example representation of p-y curves for three representative discretised layers of a pile.

This method was first proposed by Reese, Cox and Koop (1974, 1975) and was later modified by Murchison and O'Neil (1983, 1984) for homogeneous soil and then by Georgiadis (1983) for layered soil. P-y curves are used to define the relation between lateral loading and deformation in the soil. However, the p-y curve methodology was originally developed for oil and gas structures. These curves are formed by laboratory test results conducted on a specific soil sample. A range of horizontal loads "p" is applied to the top of the pile in the soil and the corresponding lateral displacements "y" of the pile are recorded. The results are then plotted to form p-y curves. The experimental tests that produce the p-y curves can be carried out with a static or a cyclic load (quasi-static), depending on the nature of the problem. For cohesionless soils, the nature of loading is considered using an experimentally defined parameter ("A"), whose value is 0.9 for cyclic and larger than 0.9 for static loads. P-y curves for cohesive soils are defined based on undrained conditions, and the ultimate soil resistance is reduced by a factor of 0.72 to account for

the cyclic nature of loading in the soil. Bisoi and Haldar (2014) studied the effect of applying static and cyclic factors on the response of monopile-supported offshore wind turbines and they concluded that the cyclic factors have a marginal influence on the pile top deflection and rotation. Nevertheless, they found that applying the widely used static p-y curves to offshore wind turbines leads to an underestimation of the monopile displacements under large loads. From a statics point of view, Abdel-Rahman and Achmus (2005), Zdravković et al. (2015) and Byrne et al. (2015) suggested that conventional p-y curves (API standards) are most suitable for small diameter piles typically used in offshore oil and gas. For larger diameter piles, as the loading increases, there is a larger deviation from deformations predicted by p-y curves. The lateral and rotational stiffness of the pile at the mudline was also found to be more nonlinear with loading than what was predicted by p-y curves (Achmus and Abdel-Rahman, 2005). Alexander and Bhattacharya (2011), Dou and Bryne (1996) and Van Buren and Muskulus (2012) suggested that p-y curves are based on static or quasi-static loading conditions and application of p-y curves to dynamic systems under strong shaking events (e.g. seismic action) can underestimate the lateral resistance of the system. However, Dou and Bryne (1996) found a good agreement between experimental and backbone p-y curves under low amplitude loads.

In addition, soil damping which results from cyclic stress or stress wave propagation through soil is not captured in nonlinear p-y curves (Bhattacharya, Lombardi and Muir Wood, 2011; Bisoi and Haldar, 2014). Shadlou and Bhattacharya (2016) suggest that this damping is dependent on the forcing frequency, soil stiffness and foundation aspect ratio. Also, formation of gaps between the soil and pile that open and close with the cyclic load, as a result of slippage between the two, is not included in the provision of current practice. Slippage is partially considered using t-z curves in cohesive soils and unit skin friction in cohesionless soils in the design guidelines, but it does not take this phenomenon into account (Van Buren and Muskulus, 2012). Similar to p-y curves, t-z curves define the force-displacement relationship, but between axial loading on the pile and pile vertical displacement, and it is dependent on the skin friction between the soil and pile (Det Norske Veritas, 2013).

The natural frequency is commonly used as a parameter to study the changes in the offshore wind turbines dynamics. In general, soil-structure interaction has a direct impact on the natural frequency of offshore wind turbines. Arany et al. (2016) studied the natural frequency prediction of various reference wind turbines using an FE model with soil springs applied at the mudline level. The first natural frequencies were normalised by the fixed base frequencies of the same turbines in their work. It was shown that the introduction of foundation flexibility could change the natural frequency of the wind turbine predicted by Equation (2-2) by 4-15%. It was also concluded by Arany et al. (2015) that the rotational stiffness of the soil at mudline has a significantly higher impact than its lateral stiffness on the 1st natural frequency. Foundation

flexibility tends to have very little influence on the first natural frequency once it reaches a certain level of stiffness. Zaaijer (2006) used a stiffness matrix method for soil stiffness at the mudline to predict the natural frequencies of various offshore wind turbines and reported up to 37% difference in the natural frequency in the Lely wind farm compared to the frequency measurements at the turbine site. It was argued that this large difference stems from insufficient data for input parameters. In other reference cases, the difference between the predictions and measurements was less than 10%. Alexander and Bhattacharya (2011) used a system of p-y curves with nonlinear damping to compare analytically the linear and nonlinear resonant frequencies of monopile-mounted offshore wind turbines. They reported that the nonlinear resonant frequency tends to reduce with increasing forcing amplitude.

Damgaard et al. (2014) studied the effect of pore water pressure in soil and concluded that pore water pressure build-up stiffens the soil and causes the natural frequencies of offshore wind turbines to be variably higher than those predicted using p-y curves. This is in agreement with the conclusions of Bhattacharya et al. (2013) for monopiles in sand. Cuellar et al. (2014) stated that during heavy storms, the high levels of pore water pressure can lead to permanent displacements in the soil.

A 1:100 scaled monopile model was tested by Bhattacharya, Lombardi and Muir Wood (2011) for foundation stiffness in cohesive soil. The results of the tests showed that the first natural frequency of the system changes by mostly 10%, depending on the cyclic stress in the soil. However, these changes increased to 35% for a specific cyclic stress setting in laboratory. Bhattacharya, Lombardi and Muir Wood (2011) suggested that the first natural frequency variations are due to the following criterion:

- Strain level in soil,
- Relative position of the natural frequency to forcing frequencies,
- The number of cycles.

Guo et al. (2015) measured the change in the natural frequency of a scaled wind turbine in sand experimentally and found that the natural frequency of the wind turbine increases with the number of cycles, but the rate of increase showed a gradual reduction as the accumulated strain in the soil increased. Cui and Bhattacharya (2016) suggests that this is caused by an increase in the stiffness due to the densification of soil around the pile.

Current methods of calculation could lead to erroneous dynamic response of the system and this can also affect the long-term performance of the structures (Alexander and Bhattacharya, 2011). Long-term soil evolution under cyclic loads is not considered in p-y curves. Achmus, Kuo and Abdel-Rahman (2009) state that cyclic p-y curves are formed based on less than 200 load cycles

in field tests. This limits the capability of p-y curves to correctly describe the long-term behaviour of monopiles under cyclic loads in the range of 10^7 cycles (Pappusetty and Pando, 2014). Bhattacharya et al. (2013) suggested that the dynamics of offshore wind turbines can be changed due to the following:

- The vibration of the pile induces cyclic strain in the neighbouring soil. This can cause higher reduction in the natural frequency, as the strain in the soil increases. However, for very small strain levels no reduction has been observed.
- Changes in soil stiffness (i.e. densification or degradation depending on soil type) due to cyclic loading.

The change in soil behaviour as a result of cyclic loading has recently been a major topic of research and as a result, several methodologies have been proposed to model the soil-structure interaction under cyclic loading (El Naggar and Novak, 1995; Achmus, Kuo and Abdel-Rahman, 2009; Depina *et al.*, 2015). Achmus, Kuo and Abdel-Rahman (2009) devised a stiffness degradation parameter based on the stresses in the solid element FE model of soil and pile. Depina et al. (2015) also adopted this technique in conjunction with Monte Carlo simulations to study the effects of soil and pile variability in properties and dimensions. In both studies, the increasing strain level in the soil was predicted in the FE models. El Naggar and Novak (1995) studied the use of near and far-field soil springs and dampers to account for soil straining under cyclic loading. Adhikari and Bhattacharya (2011) suggest that the issue concerning offshore monopiles is the dependence of their design on empirical data regarding stiffness degradation of soil under cyclic loading and emphasised that relying on the recommended pile design methods does not take this into considerations.

Achmus, Kuo and Abdel-Rahman (2009) studied the stiffness degradation of soil under relatively high amplitude of cyclic loading numerically. It was shown that for a large diameter monopile embedded in the seabed, the lateral deflection of monopile could increase significantly when subject to high load cycles. Nikitas et al. (2017) also reported a constant increase in strain accumulation using simple shear tests. Figure 2-5 shows the change in pile lateral deflection for various load cycles for two embedded lengths. As can be seen, the longer embedded length of the monopile also reduces the cyclic strain of the soil. However, it is argued that the accumulated displacement depends significantly on the magnitude of loading. Arshad and O'Kelly (2015) state that the actual severity of strain accumulation under the low-amplitude high-cycle loads and their possible influence on the dynamics of offshore wind turbines are still unclear. Numerical analysis by Pappusetty and Pando (2014) also emphasised the influence of embedded length of pile on the accumulated deformation of the pile. An optimum ratio for embedded length to pile diameter (L/D) of eight was suggested to minimise the accumulative straining effect of the piles.
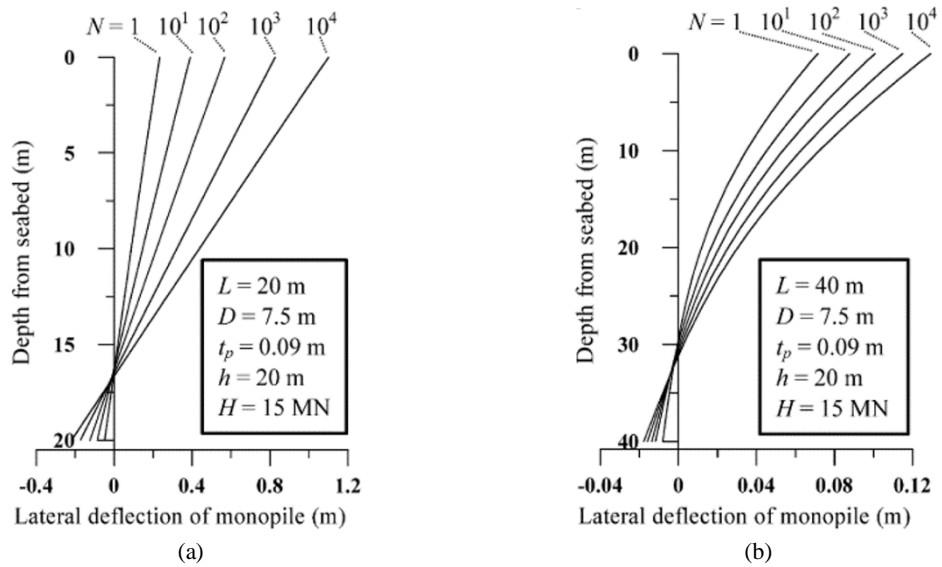
Figure 2-5. Pile deflections as a result of the stiffness degradation of the soil under cyclic loading with N number of cycles in a (a) pile with embedded length of $L=20$ and (b) pile with embedded length of $L=40$m (Achmus, Kuo and Abdel-Rahman, 2009).

In this section, it was shown that the current practice for idealisation of soil-structure interaction captures some important features. However, the influence of cyclic loading applications in offshore wind turbines is not captured well in p-y curves. From the dynamics point of view, the vibration of offshore wind turbines can vary over time, due to variations in soil behaviour under cyclic loads. The cyclic load effects have been shown to become more relevant at higher load amplitudes. Nevertheless, soil-structure interaction and application of p-y curves for monopile-supported offshore wind turbines requires more research.

2.7   Scour

Scour occurs around bottom-fixed structures constructed in a marine (offshore) environment, such as jacket oil and gas platforms and wind turbine monopiles. When an offshore structure is constructed at sea, currents and wave flows around the structure drag up soil particles (sand, clay, etc.) and deposit them further away. This results in conical holes around the structure at the mudline and a deposit of seabed soil away from it. From the dynamics point of view, the primary effect of scour is to change the embedded length and soil stiffness, which could lead to variations in the natural frequency. Scour is typically compared to some scale of the structure (e.g. pile diameter). Scour is categorised into local scour, which is the lowering of the seabed around the structure in the shape of a cone as a result of currents or a combination of currents and waves, and global scour, which corresponds to the lowering of the seabed over a larger area (Sumer and Fredsøe, 2002). Figure 2-6(a) illustrates the difference between local and global scour.

(a)	(b)
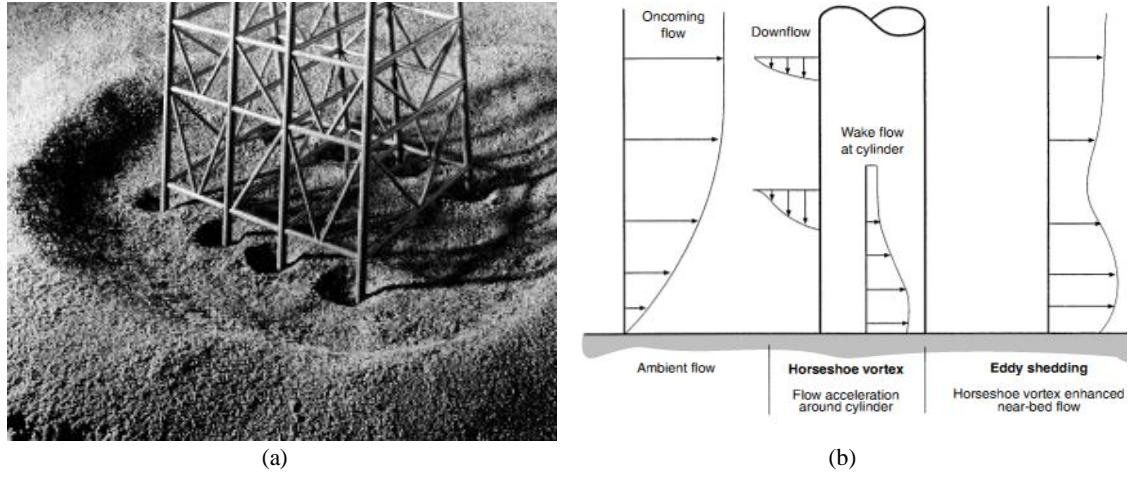
Figure 2-6. (a) An example of the local and global scour around a jacket (Whitehouse, 1998) and (b) formation of horseshoe vortex around the pile causing deposition of soil particles elsewhere (Whitehouse, 1998).

In Figure 2-6(a), local scour has occurred around each pile, while there is a large area of global scour around the group of piles. Figure 2-6(b) shows the flow around the pile. As the oncoming flow is forced around the structure, it creates a downflow at the front of the pile and a horseshoe vortex near the mudline (Tempel, Zaaijer and Subroto, 2004). Occurrence of horseshoe effect around the pile results in higher velocity of flow at the bottom, leading to the deposition of soil particles further down-stream.

Global scour can occur around an entire wind farm. However, monopile foundations mainly experience local scour, given that they are sufficiently spaced (Prendergast, Gavin and Doherty, 2015). Scour effects must be considered in the design of offshore monopiles and the DNV code (2013) recommends the use of the maximum local scour. Various researchers have investigated the prediction of equilibrium scour depth (Breusers, Nicollet and Shen, 1977; Sumer, Fredsoe and Christiansen, 1992; Høgedal and Hald, 2005; Whitehouse *et al.*, 2011; Sørensen and Ibsen, 2013). Breusers, Nicollet and Shen (1977) described the equilibrium scour ($S_{\infty,c}$) around a pile in steady current as a function of pile diameter (D_{pile}), depth-independent equilibrium scour depth (α) and sea depth (h) using Equation (2-4).

$$\frac{S_{\infty,c}}{D_{pile}} = \alpha \tanh\left(\frac{h}{D_{pile}}\right). \qquad (2\text{-}4)$$

A scour depth of $S/D_{pile}=1.3$ is suggested by Sumer, Fredsoe and Christiansen (1992) based on the work of Breuser, Nicollet and Shen (1977). Arneson et al. (2012) suggested a different approach to scour prediction which is mainly used for bridge pier design. There are limitations to this approach in large water depths, where scour depth never appears to reach a stable equilibrium (Jensen *et al.*, 2006). The estimated scour depth by Sumer, Fredsoe and Christiansen (1992) is adopted by DNV (2013) for the design of offshore monopiles.

Høgedal and Hald (2005) compared on-site measurements with design values and showed that a scour depth of $1.3D_{pile}$ is a rather conservative estimate and cost-savings could be achieved by adopting a lower scour level. Wave action, as opposed to currents, is thought to have backfilling effect in the scour process. Whitehouse et al. (2011) studied the scour and backfilling process around monopiles by monitoring sediment transportation data at different locations in European seas. Their work emphasised that scour is a process that occurs over time and never tends to stop. However, growth of scour depth slowed down to an almost negligible rate, which can be considered to be at the equilibrium scour. In one exceptional case they investigated, the increase in the scour depth did not show a clear sign of slowing down over a period of almost 4 years (from 9 months to 5 years). The scour data also indicated a periodic variation in the scour depth depending on the time in the year, which could presumably be related to the time-varying nature of scour over un-surveyed periods. Whitehouse et al. (2011) also compared measurements with the DNV recommended value of $1.3D_{pile}$ and found a slightly higher scour depth in multiple cases. However, it was argued that the measured data in most cases were too limited to draw any general conclusions. The lateral extent of scour is reported to be in the range of $4\text{-}5D_{pile}$ without scour protection. Even with the placement of scour protection, secondary scour can still occur around the pile. This was further investigated by Petersen et al. (2015). In spite of all the research, scour is a complex phenomenon and the backfilling process is not considered in design guidelines.

Scour can affect different components of offshore wind turbines. The J-tube, which supports the cable connecting the wind turbine to the energy grid, can be affected by scour. Figure 2-7 shows the configuration of a J-tube in a wind turbine with scour protection. The J-tube is designed and constructed to be laid on the seabed. When scour occurs, it leaves the installation with no vertical support so that the J-tube experiences large bending. This can cause it to fail, requiring costly disconnection from the power grid (Zaaijer and Tempel, 2004).
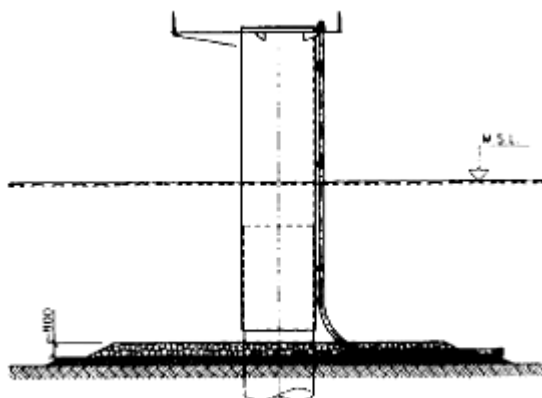
Figure 2-7. J-tube installation on a wind turbine (Tempel, Zaaijer and Subroto, 2004).

Failure of the J-tube due to scour should be considered and avoided in the design of these sections. Various new techniques have been suggested for J-tubes in order to overcome scour related issues.

Figure 2-8 illustrates some of the solutions proposed. An extended J-tube with a hinge is one of the proposed solutions, as shown in Figure 2-8(a). Rock dumping and extra supporting piles are other proposed solutions, as shown in Figures 2-8(b) and (c).
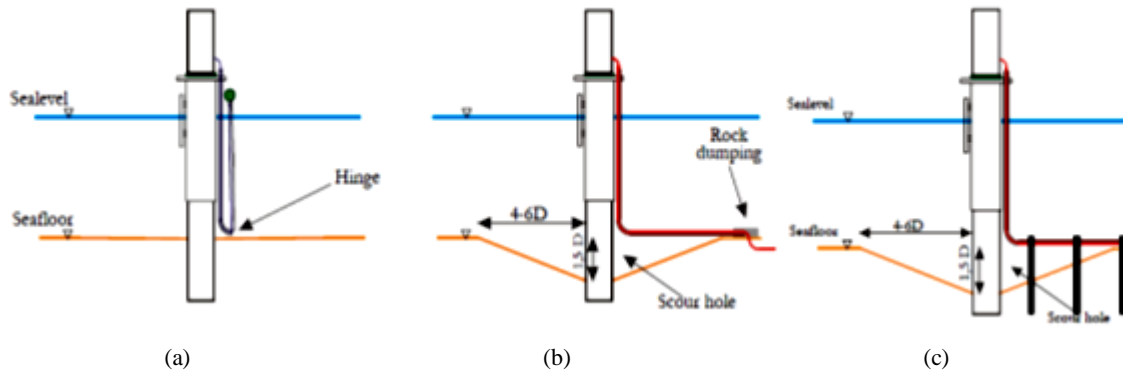
Figure 2-8. Extended J-tube concepts: (a) Hinged J-tube, (b) rock dumping at the end of J-tube and (c) anchoring J-tube to deep depths. (Zaaijer and Tempel, 2004).

More importantly, scour can have two major physical influences on the structure. Firstly, it reduces the depth of foundation fixity. This can have both static and dynamic consequences. Statically, it increases the free height of the system so that the structure experiences larger moments and displacements. Scour also reduces the resistance of the soil, as it reduces the burden pressure on the lower levels of soil (Camp *et al.*, 2003; Mostafa, 2012). Figures 2-9(a) and (b) show the effects of the scour width on a pile loaded by a lateral load of 0.5MN at the mudline, while, Figures 2-9(c) and (d) show the influence of local scour depth with a lateral extent of zero on a pile loaded by a relatively low lateral load of 0.1MN (Mostafa 2012). It can be observed that global scour causes higher increases in the bending moment in the pile than local scour.
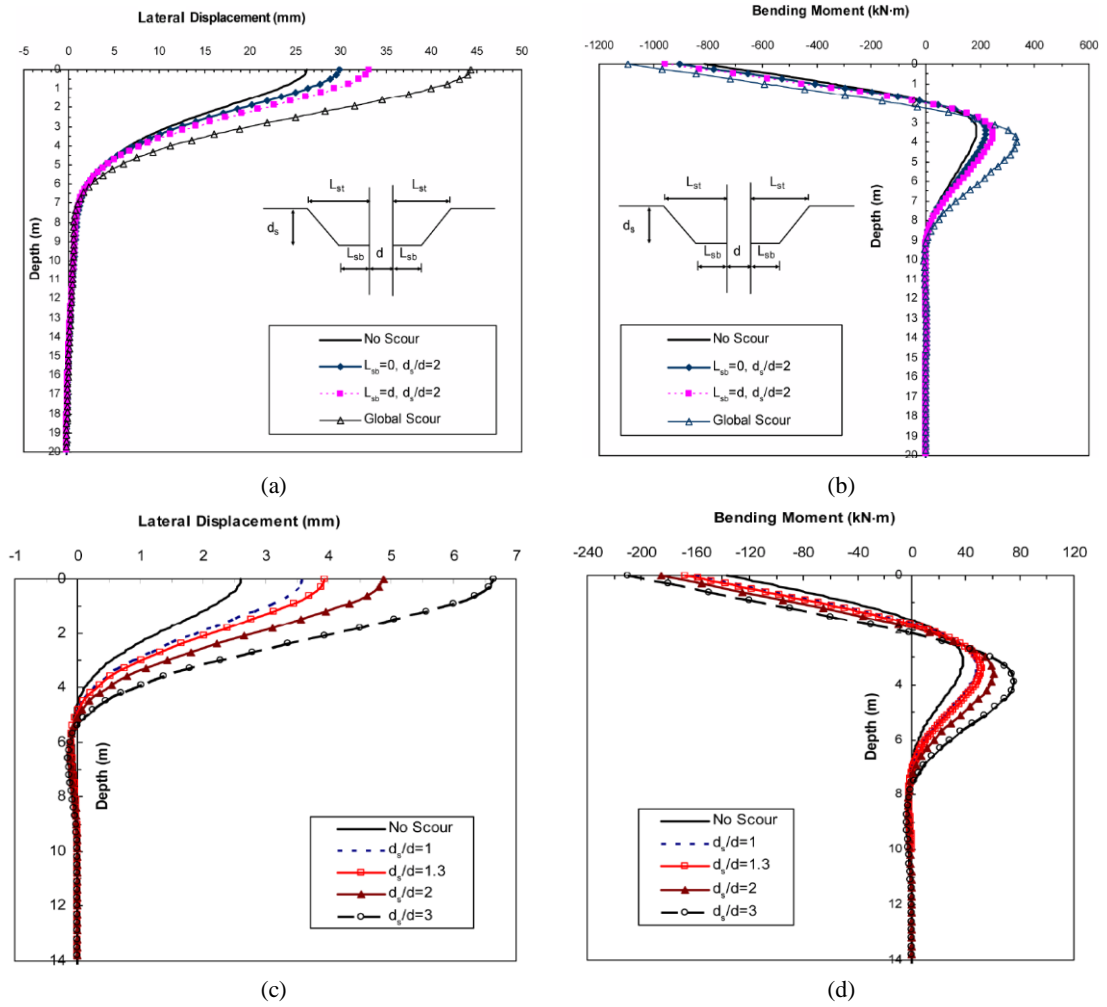
Figure 2-9. (a) Displacement for global scour and different lateral extents of local scour, (b) bending moment in the pile for global scour and different lateral extents of local scour, (c) displacement for different local scour depths and (d) bending moment in the pile for different local scour depths along the embedded length (Mostafa 2012).

According to Figure 2-9(c), for the local scour depth of 3 times the diameter of the pile ($3D_{pile}$), the pile head displacement is increased by 155%. Apart from an increase in the maximum bending moment, the location of the maximum bending moment moves down by approximately $2D_{pile}$ for global scour, as shown in Figure 2-9(b). Similarly, the location of maximum bending moment shows a shift by $2D_{pile}$ for local scour depth of $3D_{pile}$, as shown in Figure 2-9(d). The lateral extents of the scour hole does not result in a significant change in the location of maximum bending moment.

According to Zaaijer and Temple (2004), monopiles are more susceptible to scour than other wind turbine structure types. Dynamically, a maximum of 4.4% reduction in the first natural frequency of offshore wind turbines is reported in a study by Zaaijer and Tempel (2004). Sorensen and Ibsen (2013) reported a 5% and 10% decrease in the first and second natural frequencies, respectively. Prendergast et al. (2013; 2015) and Damgaard, Andersen and Ibsen (2015) also investigated the change in the natural frequency of monopile offshore wind turbines due to scour and their results

36

were in agreement with the conclusions from previous studies. However, depending on the wind turbine dimensions and soil profile some variation in the modal effects of scour can be expected. Figure 2-10 shows an example reduction in the first and second natural frequencies of monopile and tripod-supported offshore wind turbines computed using FE simulations by Zaaijer (2002).
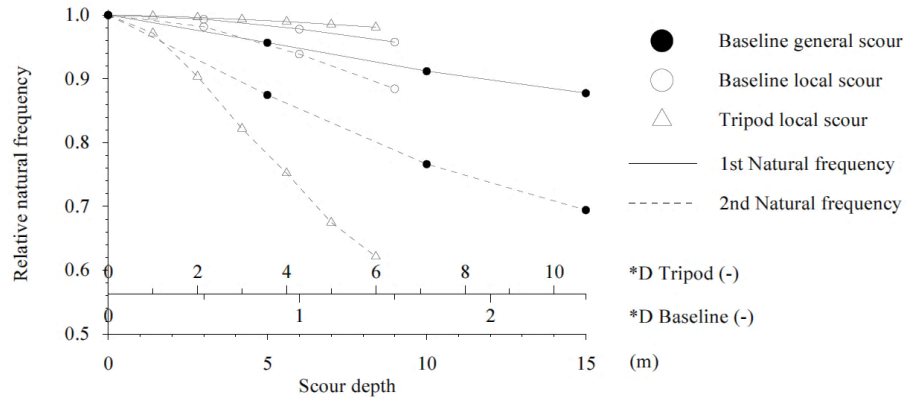
Figure 2-10. Changes in natural frequencies due to scour for offshore wind turbines supported on monopile (with outer diameter of 5.6m) and tripod (outer diameter of 1.04m) foundations. (Zaaijer, 2002).

As can be observed, the wind turbine's first natural frequency is more sensitive to general scour than to local scour. However, in the worst case (general scour depth of 2.5D), the second natural frequency experiences up to 30% reduction, while the first natural frequency reduces by approximately 10%. It is also important to note that the scour depth increases with the monopile pile diameter. The reduction in the natural frequencies of wind turbines affects the dynamic performance of the structures. The effect of backfilling on the natural frequency of the structure was studied by Damgaard et al. (2013). The compensating effect of backfilling on the natural frequency is clearly shown in Figure 2-11.
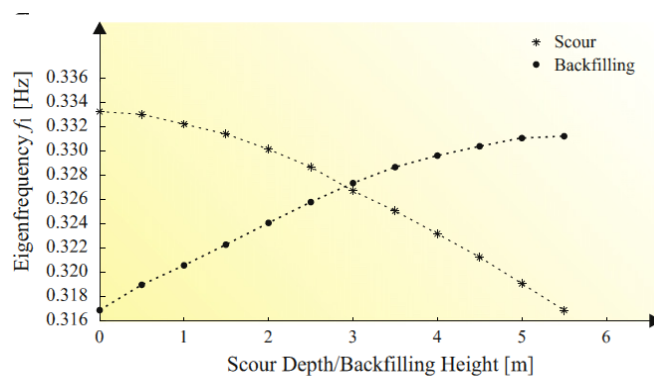
Figure 2-11. Changes in natural frequency due to scour and backfilling (Damgaard *et al.*, 2013).

Scour protection is a possible solution to limit the occurrence of scour, which benefits both the monopile and J-tube, but, as mentioned, does not stop completely the occurrence of scour. Whitehouse et al. (2011) stated that there is a high level of uncertainty in the scour depth prediction, despite all the research done. They suggested that this uncertainty implies that all offshore wind turbine structures should be protected. On the other hand, Zaaijer and Temple

(2004) argue that although the application of scour protection is common practice, it is not specifically a necessity as the costs associated with scour protections are similar to the ones for sustaining the scour hole, if they were accurately accounted for in the design. In conclusion, research has been carried out in order to predict the occurrence and extent of scour and its effects on offshore wind turbines. However, the range of measured scour depths is still quite wide from zero to higher than $1.4D_{pile}$. Also, there is always a lag between scour and backfilling (Prendergast, Gavin and Doherty, 2015). These uncertainties translate into the prediction of the dynamic response and fatigue life of the structure, which require full fatigue analysis to clarify.

2.8 Transition piece

Grouted connections are an established solution for connecting the monopile to the tower using the transition piece. These connections are mainly cast in-situ and left to cure while the tower is supported until sufficient strength is gained by material bonding. A typical grouted connection setup is shown diagrammatically in Figure 2-12.

<div align="center">(a)   (b)</div>
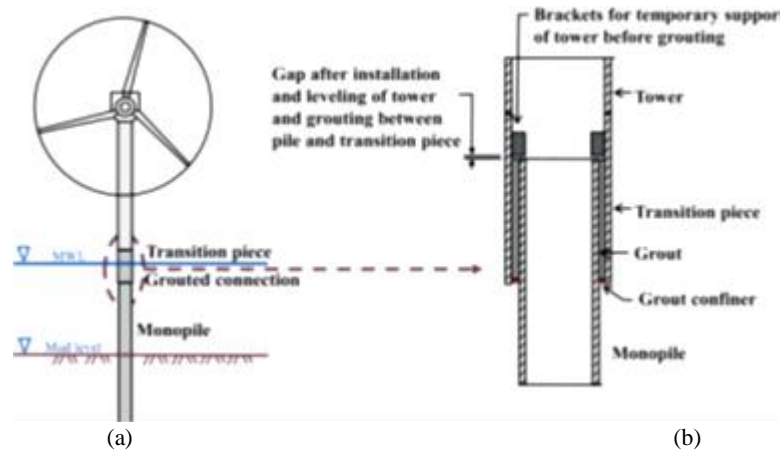
Figure 2-12. Sketch of an offshore wind turbine showing: (a) approximate location of transition piece in the wind turbine support structure, (b) grouted connection components and installation features (Lotsberg *et al.*, 2012).

Grouted connections have the advantage of allowing adjustments in verticality to be made during construction when necessary. They are mainly subjected to shear due to the weight of the tower, bending due to the wind, and torsion from blades passing the structure. Torsional stresses seem to be insignificant compared to other stresses, although they should not be ignored in their detailed design (Prakhya, Zhang and Harding, 2012). There is limited knowledge regarding the behaviour of the connections under combined shear and cyclic bending and in practice, these connections have performed fairly poorly in operating offshore wind turbines (Dallyn *et al.*, 2015), whereas they were considered reliable in oil and gas platforms. This is because the latter are primarily jacket structures supported on several well-spaced smaller piles so that they are primarily loaded by gravity, mainly inducing static shear in the connection. By contrast, the grouted connection in a wind turbine experiences significant cyclic bending. Lee et al. (2014) state that the structural reliability of grouted connections for monopiles are mostly linked to their long-term performance.

According to Stancich (2011) more than 66% of grouted connections in service have been reported as failed, indicating the importance of this type of failure in maintaining the integrity of offshore wind turbines during their service life. Figure 2-13 shows the mechanism that forms in the grout in the transition piece to resist bending loads.
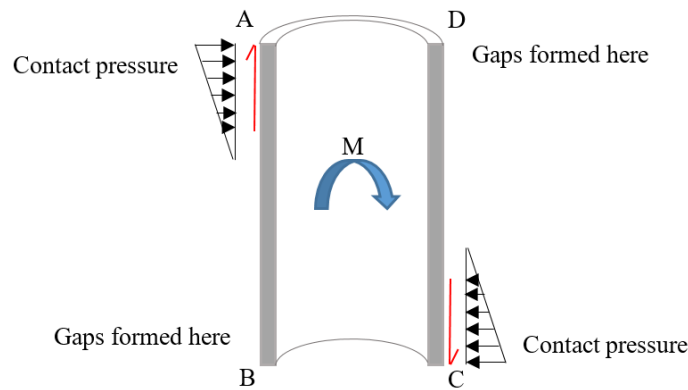
Figure 2-13. Bending resistance mechanism in an illustration of the cross section of the grout in a transition piece.

By contrast to the axial resistance mechanism, which is from surface tolerance between steel and grout, bending resistance is less well understood. Schaumann, Wilke and Lochte-Holtgreven (2008), Dedić (2009) , Andersen and Petersen (2004) and Prakhya, Zhang and Harding (2012) suggested that a push and pull mechanism takes place in the grout, due to the presence of a force couple on either side of the grout. In addition, weakness of grout in tension has proven to lead to radial and vertical cracking. Lotsberg et al. (2012; 2013) argued that there is a second order effect, especially in connections with low slenderness, which is caused by the formation of gaps and cracks. Depending on the degree of severity of these effects, a progressive cracking and crushing of the grout and/or sliding between the grout and pile sleeve can occur (Stancich, 2011). Prakhya, Zhang and Harding (2012) stated that using higher grout elastic modulus results in an increase in the stresses in the grout, which can lead to circumferential and longitudinal cracking. A maximum reduction of 40% in the coefficient of friction due to the presence of water (compared to dry samples) was recorded by Dallyn et al. (2016). The relative sliding of grout and steel could wear the grout surface. It was stated by Dallyn et al. (2016) that the offshore environment, and especially presence of water, speeds up the process of wearing by up to 18 times. This effect could be problematic for the fatigue of offshore wind turbines and should be considered in their design.

The effects of increasing the pile diameter on the resistance of grouted connections has been studied thoroughly by Prakhya, Zhang and Harding (2012) and Lee et al. (2014) and they argued that this is one of the main reasons for their poor performance and it is not addressed properly in the design guidelines. Stancich (2011) stated that being subject to such high bending from the turbines is a disadvantage of light weight wind turbines. Furthermore, this can eventually lead to

crushing of the grout at boundary regions and a progressive failure afterwards, causing slight tilt and drop of the tower (Stancich, 2011).

The behaviour of the grouted connections in the long-term is also an important issue. The cyclic loading of the transition piece in the context of jacket structures (mainly oil and gas) has been studied more extensively. Dallyn et al. (2015) stated that cyclic axial loading of grouted connections results in increased grout deformation due to the reduction of grout-pile skin friction. Schaumann, Wilke and Lochte-Holtgreven (2008) found an increasing gap size between the grout and pile with the number of cycles through four point bending tests of scaled laboratory specimens. Schauman, Wilke and Lochte-Holtgreven (2008) studied the influence of various transition piece parameters (e.g. grout elastic modulus, grout and steel slenderness, and overlap length) and suggested that overlap length, contact friction and slenderness of steel section can affect the first natural frequency of monopile supported offshore wind turbines more than the others.

In 2009, after a joint industry project, the DNV guidelines were modified regarding the design of grouted connections and the use of conical connections has been advocated since. These have a very similar force transfer mechanism, but vertical slippage is limited due to geometry. The London Array has adopted this concept (Deign, 2012). However, it is argued that these connections have the drawback of having higher contact stresses in the grout and this implies that the design of these connections involves crushing of the grout at these points (Stancich, 2011). There is also limited experience from those installed. Nevertheless, Lee et al. (2014) stated that conical grouted connections tend to be the preferred option for the transition piece from fatigue viewpoints, as this type of connections tends to reduce the mass and increase the fatigue strength compared to normal connections. The use of shear keys in the transition piece is left open to the designer. However, most of the recent designs consider shear keys. The effects of shear keys was studied by Schaumann, Wilke and Lochte-Holtgreven (2008) and a 20% increase in bending stiffness and 50% decrease in gap size was reported. Lotsberg (2013) recommended that grouted connections without shear keys are unsuitable for use due to the low long-term axial capacity of these connections. However, the presence of shear keys is thought to increase fatigue damage in the transition piece due to higher stress concentrations around the weld-beads.

The influence of grouted connections on the dynamics of offshore wind turbines is less researched and the influence of grouted connections on the fatigue of steel monopiles is less understood. Dallyn et al. (2015) states that the voids in our knowledge on the long-term performance of the transition piece under operational environmental conditions still remain.

2.9 Fatigue of monopile-supported offshore wind turbines

Fatigue design is done by comparing the fatigue demand, which is a combination of all the load cycles, on the structure or a component to the fatigue strength of that element, which is the number of cycles that the component or structure can tolerate before failure. In welded steel structures, fatigue damage is mainly caused by micro cracks, which can grow during loading cycles (Gupta and Singh, 1986).

S-N curves provided in DNV (2014) guidelines are typically used in the design of offshore wind turbines. Prediction of fatigue strength is commonly done using the nominal stress approach, in which the fatigue demand on the structure is compared to the nominal permissible stress using S-N curves for the considered structural detail, including stress concentrations factors (SCFs) when necessary to account for possible higher stresses at structural discontinuities (e.g. hot-spot locations of maximum local stress) (Schaumann *et al.*, 2011). Figure 2-14 shows the S-N curves for different structural details in seawater.
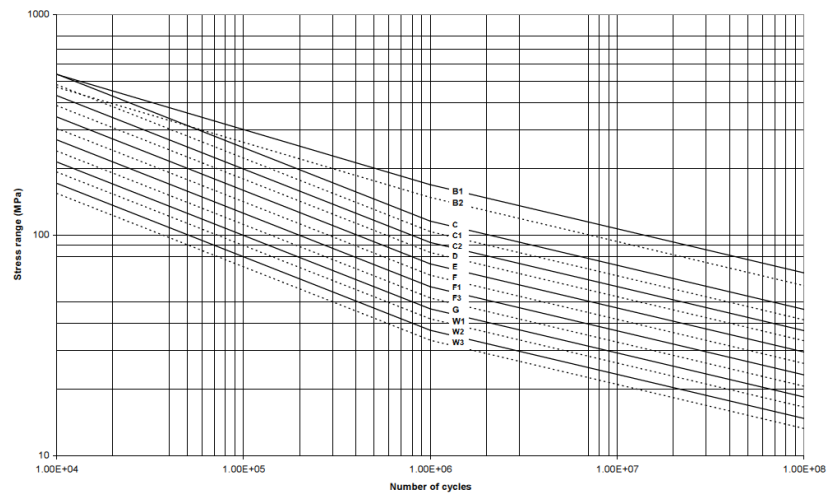
Figure 2-14. S-N curves for constant amplitude loading of a structural detail in sea water with cathodic protection (Det Norske Veritas, 2014).

A realistic fatigue analysis of an offshore wind turbine requires a comprehensive model that has three main components: environmental conditions model (wind profile and sea state), an aerodynamic model of rotor blades and the structural dynamic model of the turbine and foundation (Schaumann *et al.*, 2011). Figure 2-15 shows an example of an idealised model of an offshore wind turbine for finite element simulations. The transient wind and wave loads in an FE simulation can be modelled as lateral point loads for simplicity.
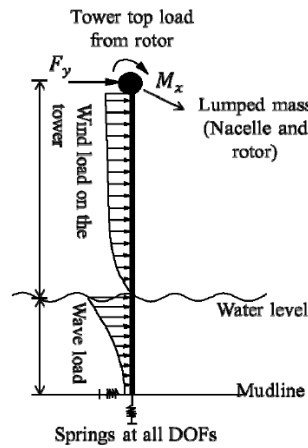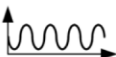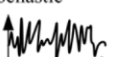
Figure 2-15. Integrated model of offshore wind turbine for fatigue analysis (Sheng and Chen, 2010).

The American Bureau of Shipping (2014) suggests four methods for the fatigue analysis of structures: simplified method, deterministic method, spectral method (in frequency-domain) and time-domain method. Simplified assessment techniques do not provide a fatigue life or damage and are mostly a pass/fail check against a cyclic stress. In the deterministic method, the stress demand in the structure is calculated using deterministic environmental conditions, as opposed to the environmental states' energy content characterisation in spectral and time-domain methods. Spectral method has been commonly used for the design of offshore structures. However, its application in the design of offshore wind turbines does not go a long way (Yeter, Garbatov and Guedes Soares, 2016). As the dynamic response to the aerodynamic loading in offshore wind turbines has a wide bandwidth, damage calculation methods in the frequency domain, which mostly work well on narrow-band signals, show extremely conservative estimates (Du *et al.*, 2015). This conservativism is usually overcome by correction factors to account for the wide bandwidth of the response. However, the formulas for the calculation of the correction factor are fairly complicated and they are not always accurate in the prediction of the fatigue damage in offshore wind turbines (Low, 2011; Du *et al.*, 2015; Mohammadi *et al.*, 2016; Yeter, Garbatov and Guedes Soares, 2016). Spectral method (frequency-domain) is used when the structural response to the environmental loads is linear. Alternatively, the time-domain analysis of the structure is recommended for structures experiencing non-linear structural response (American Bureau of Shipping (ABS), 2014). For wind turbines and components such as grouted connections and welded joints, a time-domain analysis is more widely used as it allows more complex loading simulations on the system. The time-domain fatigue analysis method is considered to be highly accurate, but they are significantly computationally expensive. Different fatigue analysis techniques are benchmarked against the time-domain method (Halfpenny, 1999; Low, 2011; Du *et al.*, 2015). Rain-flow counting is commonly employed for cycle counting and calculation of fatigue damage for variable amplitude cyclic loading in the time-domain. This method defines closed stress/strain loops, which are used to find the damage induced by each cycle (Downing

and Socie, 1982). The dynamic loads on the structure are typically modelled in short intervals and the results are extrapolated to the lifetime of the wind turbine using cycle counting methods to estimate the mean load levels and load ranges (Sheng and Chen, 2010; Schaumann, Lochte-Holtgreven and Steppeler, 2011; Blasques and Natarajan, 2013). IEC international standards (2005) suggest that multiple (6 runs) 10-minute simulations are required for the fatigue analysis in order to achieve statistically stable results. Alternatively, a single 1-hour simulation is considered to be sufficiently long to ensure statistical stability of the results. Stieng et al. (2015) suggested that statistical treatment of 10 minute signals using linear regression can be carefully used to extrapolate damage accumulations to match the results of 1-hour simulation. However, it is stated that further research is required to confirm the robustness of their approach.

During the 20 to 30-year lifetime of an offshore wind turbine, the rotor load typically exceed 10^9 cycles (Dong, Moan and Gao, 2011, 2012). Table 2-1 categorises these various loads by type and time-dependence. The most relevant loads for fatigue are the periodic and stochastic ones. Accidental (transient) loads can also have an adverse effect.

Table 2-1. Example of loads on a wind turbine in dependence of time variation and source (Schaumann, Lochte-Holtgreven and Steppeler, 2011).

Origin / Time Variation	Type of loading	Source Area	Operating Mode
Quasi-stationary	Gravitational Force, Centrifugal Force, Mean Shear	Mass, Rotation of Rotor, Mean Wind	Normal Operation Conditions
Periodic	Unbalanced Mass, Aerodynamic Forces	Unbalance, Pre-flow of Tower, Inclined Flow, Blade Pass	Normal Operation Conditions, Troubles
Stochastic	Aerodynamic and Hydrodynamic Forces	Wind Turbulence, Sea State, Earthquake	Normal Operation Conditions
Transient	Friction and Brake Forces, Aerodynamic Forces	Turbine Stop, Yaw of Nacelle	Manoeuvre, Troubles, Extreme Operation Conditions

In practice, real environmental conditions are too complex so they have to be simplified for numerical simulations (Schaumann et al. 2011). Also, the environmental loads can be variable from one wind turbine to another in a wind farm, as the aerodynamic loading is affected by the formation of wakes depending on the position of the wind turbine in a wind farm (Ashuri *et al.*, 2016). Blasques and Natarajan (2013) state that wind turbines are generally affected by rotor loads but the role of marine loads also increases with sea depth. In shallow to intermediate water depths, the aerodynamic loads are typically dominant compared to hydrodynamic loads for an operational wind turbine. However, in deeper waters the role of hydrodynamic load is significantly more pronounced, leading to a higher contribution to the fatigue damage of the wind turbine (Blasques and Natarajan, 2013).

In fatigue analysis, most damages occur due to the rotor and hydrodynamic loads in operation, when the wind speed is between the cut-in and cut-out speeds of the wind turbine (Borri, Biagini and Marino, 2011; Arshad and O'Kelly, 2015). According to Schaumann, Lochte-Holtgreven and Steppler (2011), the wind profile comprises a mean wind speed and a turbulence which is a stochastic variation around the mean speed over a period of time. The rotor thrust is the resultant of the forces caused by the flow of air through the rotor disk. Blade element momentum theory (BEM) is commonly used for the calculation of the rotor thrust. According to this theory, the drag and lift forces are calculated for each elemental segment of the blades for the in-flow wind. Aerodynamic modelling software, such as AeroDyn by the National Renewable Energy Laboratory (NREL), employ additional measures, known as Generalised Dynamic Wake (GDW), also known as Method of Acceleration Potential, to improve the pressure distribution on the rotor disk calculated by the BEM method (Moriarty and Hansen, 2005). The turbulent wind is a major contributor in the fatigue of wind turbine support structures.

Wave loads are defined based on the type and characteristics of the immersed structure. There are various wave theories available to simulate these loads. Linear or nonlinear irregular wave kinematics is commonly used for wave load simulation on wind turbines, depending on the water depth and wave height. However, Ziegler et al. (2015) suggested that hydrodynamic fatigue loads are significantly sensitive to the wave period. Veldkamp and Tempel (2005) studied the influence of wave kinematics on the fatigue loads on a reference offshore wind turbine and showed that the deviation of fatigue loads between the predictions by 1st and 2nd order waves is minor (up to 5%). However, a closer spectral shape was observed between the 2nd order waves and site measurements. Marino, Giusti and Manuel (2017) examined the influence of linear and nonlinear wave kinematic theories for different turbine operational regimes and found that consideration of nonlinear wave theory has a more significant effect on the fatigue damage when the wind turbine is parked. However, when the turbine is in operation the influence of wave kinematics used for the fatigue analysis is overridden by the higher aerodynamic loads and damping. In the calculation of wave loads, currents add to the overall wave load on the structure which in turn increases the fatigue damage in the wind turbine (Schaumann, Lochte-Holtgreven and Steppeler, 2011; Blasques and Natarajan, 2013).

The relative directionality of wave and wind loads has been the subject of research. Sheng and Chen (2010) state that fatigue damage is generally more liable to occur in the prevailing wind and wave direction. Damgaard et al. (2015) suggested that from the fatigue design perspective, at sites where wave and wind misalignments are significant, the fatigue damages in the side-side direction can be reduced by moving the first natural frequency of the wind turbine away from environmental loads in a soft-stiff design. The influence of environmental load directionality on the cross-wind fatigue damage of the wind turbine was studied by Koukoura et al. (2016), using

on-site measurements and simulations of a reference wind turbine. Onsite measurements showed minor influence on the fatigue damage in the tower, while the simulations showed a higher sensitivity as a result of misalignment. However, it was concluded that this was a result of higher than anticipated damping values in the real wind turbine. The sensitivity of fatigue damage in the offshore wind turbines became less sensitive to wind and wave misalignment for higher damping values in the wind turbine. As stated before, soil stiffness and damping can have a significant influence on the dynamic response, and hence the fatigue of offshore wind turbine. Sheng and Chen (2010) stated that the stiffness of soil can decrease the fatigue load considerably, however its influence varies with water depth. It is further suggested that the effects of soil stiffness can be ignored when the soil has a high level of stiffness. The resultant fatigue loads (shear and bending) at the mudline due to soil stiffness variations are shown in Figure 2-16. It should be noted that the test cases in the study by Sheng and Chen (2010) are limited and the changes in fatigue damage require clarification for lower soil stiffness values.

| (a) | (b) |
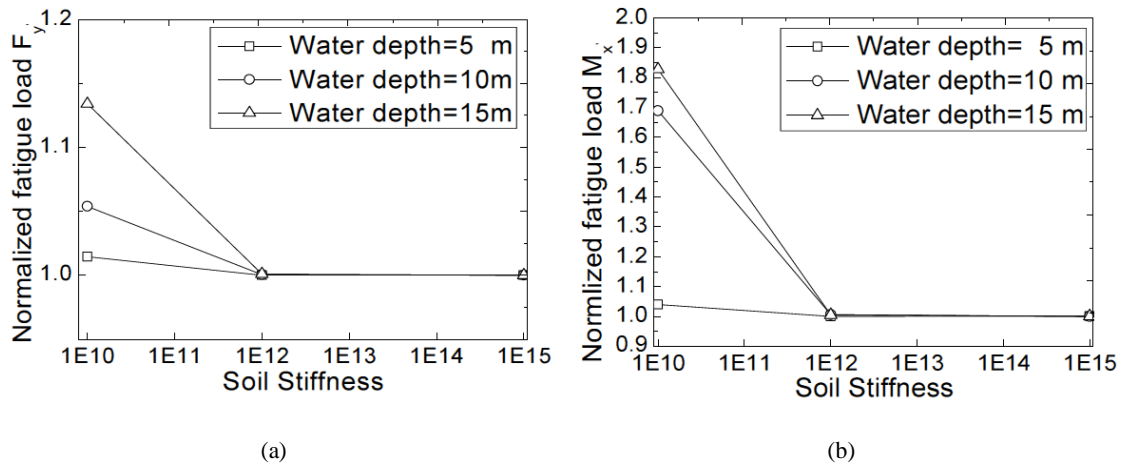
Figure 2-16. Effects of soil stiffness (for various water depths) on (a) the normalised fatigue shear load F_y, and (b) overturning moment M_x, at the mudline (Sheng and Chen, 2010). Results are in fore-aft direction and normalised against the lower values.

In addition, long-term variability of soil can have a negative impact on the fatigue damage in the monopile. Schafhirt et al. (2016) investigated the influence of soil stiffness variability in sand on the fatigue life of the offshore wind turbine and found that fatigue life reduces by 9% for softening, while it increases by 4% for stiffening of the soil. It was also suggested that a more accurate modelling than conventional p-y curves is required for a better understanding of fatigue influences of soil variability.

Fatigue damage due to scour around the turbine in parked conditions was studied by Weinert (2015) and Damgaard, Andersen and Ibsen (2015). An increase of up to 60% in the fatigue damage was reported for scour levels of up to $1.3D_{pile}$. Higher levels of scour were studied by Tempel (2006), who considered the effect of scour on the fatigue damage of monopiles using a frequency-domain approach. A considerable change of up to 100% in the fatigue damage was

reported for a 2.5D$_{pile}$ scour level at the mudline. However, it was suggested that this is a relatively high scour depth to be considered for fatigue limit states. Sørensen and Ibsen (2013) conducted simple fatigue checks for various levels of scour and suggested that by considering backfilling processes in the fatigue design of monopiles, the stress demand on the monopile below the seabed is reduced by up to 37%. A complete study of the scour and backfilling effects in an operational wind turbine remains outstanding in the literature.

Because wind turbines are lightly damped structures, the estimation of damping in these structures is crucial for the prediction of fatigue life, as the amplitudes of vibrations at resonance are inversely proportional to damping ratios (Shirzadeh *et al.*, 2013). Damgaard et al. (2013; 2015) studied the effects of damping in a parked offshore wind turbine and showed that the maximum bending moment could increase by 25% as a result of 50% reduction in damping. However, increasing the damping by up to 200% resulted in approximately 10% reduction in the mudline bending moment. Fontana et al. (2015) investigated the effect of variable soil damping levels on the reduction of fatigue damage for a combination of wind and wave loads in a parked and operational wind turbine using linear time-domain simulations. It was found that increasing the soil damping has less significant effect on the fatigue damage of the wind turbine in rougher sea conditions. However, the joint probability of occurrence of the aerodynamic and hydrodynamic loads and their influence were not properly addressed. Also, a fixed boundary was considered for the bottom of the monopile, which is unrealistic. Koukoura et al. (2016) reported that doubling the non-aerodynamic damping reduces the crosswind fatigue damages in the wind turbine by 86%. However, Fontana et al. (2015) and Koukoura et al. (2016) found that when aerodynamic damping is high (i.e. in operation and fore-aft direction) non-aerodynamic damping contributions become less important. The influence of damping in an operational wind turbine using the benchmark time-domain fatigue analysis is hardly ever done in the literature. It was also suggested by Fontana et al. (2015) that a complete fatigue simulation of damping effects with correlated environmental states could clarify its influence in more details.

2.10 Summary

In this chapter, the characteristics of offshore wind turbines that affect their dynamic and fatigue performance were reviewed. Offshore wind turbines mounted on monopiles were selected as the focus of the research, as they have the largest percentage of installed capacity, and failure of offshore wind turbines was discussed. An overview of the research on the influence of damping and the uncertainties associated with it was given. Soil-structure interaction and its importance in monopile performance was discussed. This was followed by a review of the literature on scour effects on the monopiles. The weaknesses of grouted connections were outlined. Finally, fatigue was considered. The following conclusions could be drawn from the literature review:

Knowledge on offshore wind energy structures is based on the onshore wind and more mature experience and knowledge gained in the oil and gas industry. However, the two industries are considerably different concerning their loading and other details of the structural design. Monopiles are the most common type of support structures for offshore wind turbines to date. The harsh environment that surrounds monopile offshore wind turbines creates vibration concerns. Three main areas of influence exist in the vibration of offshore wind turbine: inertia, damping and stiffness. Inertia is fairly well characterised. However, damping and stiffness effects attracted higher attention in the literature due to the complexities in their prediction.

Damping is one of the main drivers in the fatigue of offshore wind turbines. Energy dissipation through aerodynamic damping has proven to be the main contributor to the total damping present in the structure in operation. However, research has shown that estimation of aerodynamic damping is a complex task and measurements show variations in the results. It was also argued that soil damping can be higher than normally anticipated. Thus, the uncertainties in the actual amount of damping present in offshore wind turbines can affect their fatigue life significantly and require further research.

Soil-structure interaction, scour and transition piece performance affect the stiffness and hence, the dynamics and fatigue of offshore wind turbines. Soil-structure interaction between the monopile and soil is critical. The theories are all adopted from oil and gas platforms, which have significantly different characteristics. The current techniques for the application of p-y curves in the design of monopiles have shown to lack integration of the long-term soil-structure interaction elements, especially under high amplitude loads, which can put the predicted life of these structures in question. Various recent approaches for the analysis of soil-structure interaction and consideration of these effects were suggested. Yet, the extent of these effects on the long-term performance of offshore wind turbines requires further research.

Scour primarily increases the bending moment in monopiles. Tower top displacement was also shown to experience significant increase as a result of scour. Additionally, monopiles are designed to have their first natural frequency in a narrow band between the blade passing frequency (2P or 3P) and the rotor frequency (1P). Scour depth of $1.3D_{pile}$ is the recommended value for the design of offshore wind turbines, which could alter the natural frequencies of monopiles. This has significant effects on the dynamic response and long-term performance of these structures. However, research has shown that scour depth can be variable and the backfilling processes were shown to compensate some of the adverse effects of scour. The uncertainties regarding the scour depth and backfilling process requires further attention to the long-term implications of scour.

A large number of monopiles with grouted connections have been reported for connection damage or failure. The design of these connections is adopted from oil and gas industry. In offshore wind

turbines, grouted connections undergo a combination of large axial and bending loads, which is different from oil and gas platforms. Moreover, the bending action in these connections is very complex and therefore better modelling and analysis of these connections is crucial. Shear keys or conical connections are now recommended to be used in offshore wind turbines to increase the strength of these connections. However, it was also shown that over the life of a monopile, the wearing of grout could occur which increases the chances of fatigue life reduction.

Monopiles experience various dynamic loads throughout their lifetime, which highlights the importance of fatigue design for these structures. The real loads are too complex for simulations and have to be simplified. Wind and wave loads are combined and analysed on the basis of time-domain analysis. Time-domain fatigue analysis of offshore wind turbine is used as a benchmark for fatigue predictions. The fatigue life of offshore wind turbine can vary due to different sources of uncertainty (damping, soil stiffness and scour). Fatigue loads were shown to be sensitive in offshore wind turbines with soft soils. The influence of damping on the fatigue life of offshore wind turbines' monopiles in parked and operational conditions showed that fatigue damage is significantly affected by the level of damping. A complete study of fatigue life changes due to different damping levels has been recommended on several occasions. In addition, scour was shown to have an influence on the fatigue of monopiles in parked condition. However, under operational conditions the effect of scour has not been studied thoroughly. Combination of scour and backfilling over the life of offshore monopiles was shown to be advantageous for their fatigue. As both scour and backfilling processes are unknown and uncertain, design of offshore wind turbines can be on the over-conservative side. Their influence on the fatigue of monopile-supported offshore wind turbines in operation still remains unclear. It is evident from the literature that knowledge of the fatigue life under operational conditions through a complete fatigue life analysis, with all the uncertainties surrounding various influential parameters in the subject such as damping, scour and backfilling, is rather limited.

2.11 Research objectives

This research is a comprehensive study of the different factors that can influence the fatigue of offshore wind turbines. The effects of variations in the soil-structure interaction and grouted connections on the stiffness of the wind turbine are investigated. In the study of soil-structure interaction, the applicability of p-y curves for the fatigue analysis of offshore wind turbines is assessed against 3D finite element models through the study of wind turbine stiffness variations in different soil types (i.e. stiffness). The influence of long-term damage in the grouted connections on the stiffness of the monopile-supported offshore wind turbines is studied through variations in the grout strength and surface resistance in 3D finite element models, and the

implication of these effects on the fatigue damage of the monopile in offshore wind turbines is discussed.

This research aims to investigate the influence of damping and scour on the fatigue life of offshore wind turbines systematically to show the extent of variations in the fatigue life accurately. The sensitivity of the fatigue life due to the absence of aerodynamic damping in a non-operational turbine and the uncertainties attached to the amount of total damping and possible benefits of added damping in operation are studied using time-domain finite element (FE) simulations on a reference offshore wind turbine supported on a monopile. The influence of variations in the seabed level (i.e. scour), backfilling depth and material density on the fatigue life of the wind turbine is investigated thoroughly using the same finite element model.

As the time-domain fatigue analysis of the wind turbine is computationally expensive, approximate methods are proposed to reduce the costs of the fatigue analysis simulations associated with the study of damping and scour variations' effects on the fatigue life of offshore wind turbines.

3   Methodology

3.1   Introduction

The study of the fatigue life of offshore wind turbines requires detailed models which are not readily available in the literature. In this project, a combination of available data from different sources was used as coherently as possible to create a single model with sufficient detail for a complete fatigue life study. This chapter introduces the reference offshore wind turbines used and presents the methodology employed for the modelling and analysis of the wind turbine. More detailed methodological features on specific aspects will be presented in the subsequent chapters (e.g. solid element modelling of the wind turbine for the study of soil-structure interaction and transition piece).

The complete fatigue analysis was carried out in different stages using different software packages. The process is schematically described in Figure 3-1.
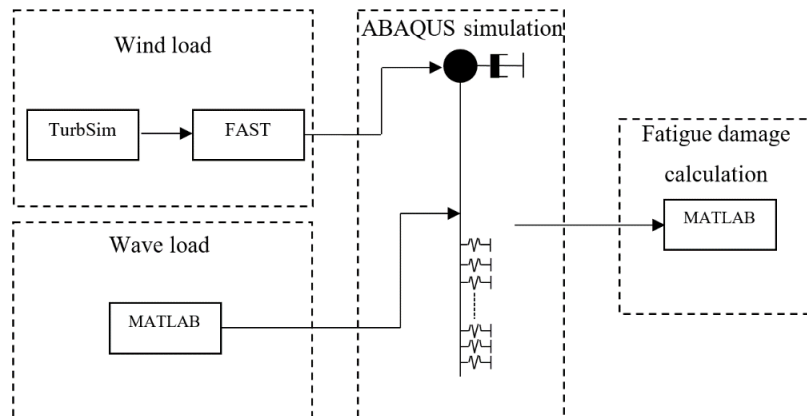
Figure 3-1. Software interactions for the study of fatigue life.

The wind load including the aerodynamic interaction with the blades was computed using FAST (Fatigue, Aerodynamics, Structures and Turbulence), a software package provided by NREL (National Renewable Energy Laboratory) which includes a model of the turbine used here. As FAST has limited capabilities for modelling soil-structure interaction, and the structural model it includes is fairly basic, the rotor loads obtained from FAST were used as input for an ABAQUS beam element model of the support structure including p-y curves for the soil-structure interaction. The wave loads were calculated using MATLAB and were implemented as input in ABAQUS. The outputs from ABAQUS are maximum stress time-histories for various characteristic wave heights/periods and wind speeds. These were post-processed in MATLAB to compute the fatigue life. This method of decoupling and combining of the environmental loads is

established in the literature, and has been applied by Tempel (2006) or Alati et al. (2014), for example.

3.2 Reference wind turbine

A wind turbine model detailed enough for the fatigue analysis of the supporting structure must consist of the following parts:

- Aero-elastic model of the turbine
- Tower
- Transition piece
- Monopile
- Soil support
- Environmental conditions data

The wind turbine used in this study is primarily based on two reference wind turbines, which combined have an adequate amount of data publicly available. According to Ferguson et al. (1998), the Opti-OWECS project is a 300MW wind farm consisting of 100 wind turbines (3MW each). The DOWEC was a project supported by the Dutch Ministry of Economic Affairs (Nehal, 2001; Kooijman *et al.*, 2003). The DOWEC wind turbine design has been extensively used as a reference in the literature and in industry for research purposes. NREL modified this design slightly and created a conceptual baseline design on FAST based on the original wind turbine (Jonkman *et al.*, 2009). From this point onwards, the DOWEC 5MW wind turbine will be referred to as "the NREL 5MW wind turbine". Table 3-1 shows the amount of the available data for these two wind turbines.

Table 3-1. Comparison of the availability of the data for the two reference wind turbine models considered in this research.

	NREL 5MW	Opti-OWECS 3MW
Tower	●●	●●
Transition piece	●	●●
Monopile	●●	●●
Soil profile	●	●
Environmental states details	●	●●
Aero-elastic model	●●	X

Notes:
X: No data
●: Incomplete/basic data
●●: Available

For the NREL 5MW wind turbine, a good amount of information regarding the structural properties and aero-elastic modelling of the turbine is available, but there is insufficient information regarding the environmental conditions, transition piece and the soil profile at the

site. The Opti-OWECS 3MW wind turbine offers good detail on the structural properties, including the transition piece, and environmental data, but has limited data on the soil properties and aero-elastic modelling of the turbine.

General specifications of the two reference wind turbines are given in Table 3-2.

Table 3-2. General properties of the NREL 5MW and Opti-OWECS 3MW wind turbines.

	NREL 5MW	Opti-OWECS 3MW
Number of blades	3	2
Rotor diameter (m)	126	80
Hub height from MSL (m)	92.4	57.6
Pile penetration (m)	45	25
Monopile diameter (m)	6	3.5
Monopile thickness (m)	0.08	0.075
Tower diameter (m)	Variable	2.8
Tower thickness (m)	Variable	Variable
Operation type	Variable rotor speed - pitch controlled	Constant speed - pitch controlled
Operational range (m/s)	3-25	5-25
Rated wind speed (m/s)	11.5	13.7
Rotor speed (rpm)	12	22
Turbine mass (t)	375	135

The 2-bladed 3MW wind turbine is supported on a monopile foundation. The wind turbine structure has a variable diameter from 3.5m to 2.5m at the pile section. The tower section diameter is 2.8m, which increases to 3.5m from 4m below the nacelle level. The transition piece has a dimeter of 2.68m and a length of 5m.

Structurally, the NREL 5MW support structure consists of a monopile and a tower section. To date, little data has been published on the transition piece of this wind turbine. The monopile is a 75m long pile with a diameter of 6m. In this study, the thicknesses of the pile and tower sections were modified from the original documents (Kooijman *et al.*, 2003; Jonkman *et al.*, 2009). This is due to uncertainties in the embedded length and soil conditions of the pile and was necessary to ensure that the natural frequency of the wind turbine lies between the 1P and 3P frequencies with a margin of 10%. Thus, the pile thickness of 80mm and variable tower thickness of 28-38mm was used.

The support structure is constructed from steel sections. The steel used for the monopile section is assumed to be similar to the tower, with an elastic modulus of 210GPa and Poisson ratio of 0.3. The density of steel is assumed to be 7850 kg/m^3. However, a higher density steel (ρ=8500kg/m^3) was used for the tower section of the NREL 5MW wind turbine to take into account the paint, bolts, flanges and other connection details on the tower (Jonkman *et al.*, 2009). Geometric details

of the two wind turbines are illustrated in Figures 3-2(a) and (b). It should be noted that these figures are not to the same scale.
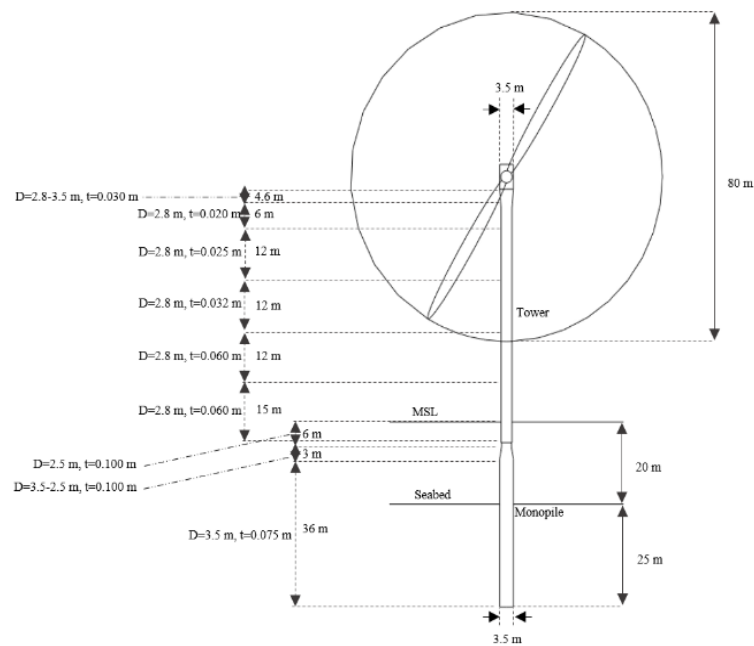
(a)
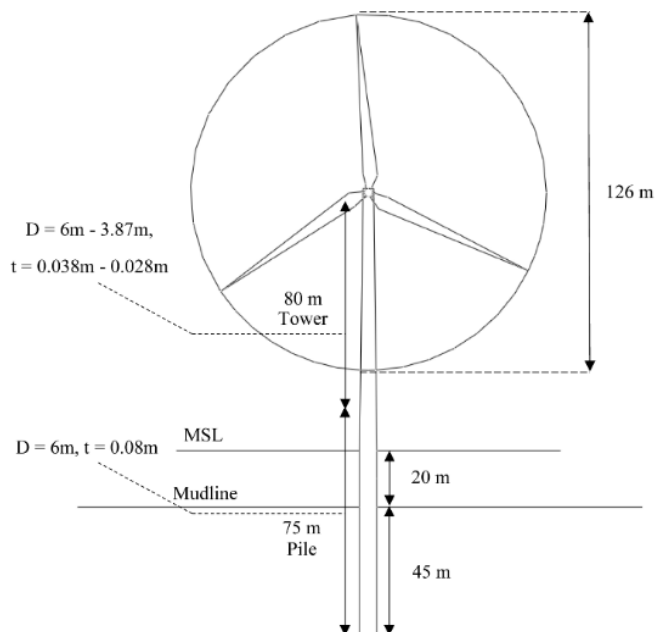
(b)

Figure 3-2. Geometric properties of the reference wind turbines and their support structures: (a) Opti-OWECS 3MW wind turbine and (b) NREL 5MW wind turbine.

The Opti-OWECS 3MW wind turbine has a rotor diameter of 80m with a rated rotational speed of 22rpm. The power output is controlled through pitching of the blades. As a result of this rotor speed, the 1P and 2P frequencies are 0.37 Hz and 0.73 Hz, respectively. Ferguson et al. (1998) selected a soft-soft approach for the design of this wind turbine, in which the first natural frequency of the monopile lies below the 1P frequency. It was stated that this approach is a more

desirable option than the conventional soft-stiff design, as the margin between the first and second blade passing frequencies are significantly narrower than for a 3-bladed turbine and the amount of material used for a soft-soft design is significantly lower for this wind turbine.

The blades in the NREL 5MW wind turbine are based on a LM-Glasfiber Holland design with a length of 62.7m, whose properties could be found in the report by Lindenburg (2002). The rotor speed at the rated wind speed is 12.1rpm with a cut-in wind rotor speed of 7rpm. The rated wind 1P and 3P frequencies for this wind turbine are 0.2Hz and 0.6Hz, and the first natural frequency of the wind turbine is designed to lie between the 1P and 3P frequencies. This leads to a soft-stiff design approach.

Both wind turbines are proposed to be built in the Dutch territories of the North Sea. As the available data for both were obtained from the predesign stage reports, several location options were considered for each wind turbine as shown in Figure 3-3.

(a)　　　　　　　　　　　　　　　　　　(b)
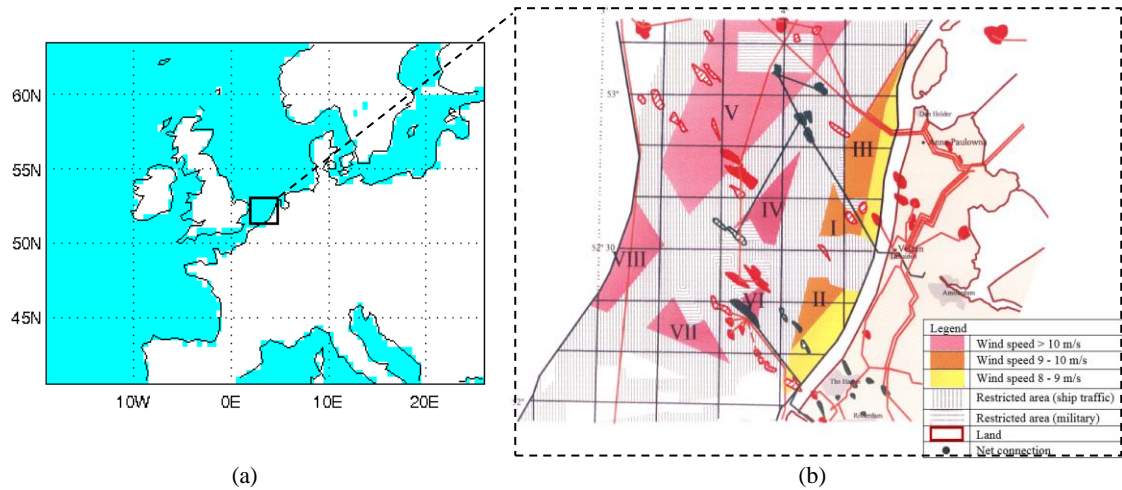
Figure 3-3. Locations considered: (a) overview of Dutch North Sea (Waveclimate.com, 2016) and (b) possible sites within the Dutch North Sea, numbered using Roman numerals (Ferguson *et al.*, 1998).

The Opti-OWECS (3MW) wind turbine with monopile foundation is proposed to be built on the NL-1 offshore site, while the NREL 5MW wind turbine is considered to be constructed on the NL-3 site. Both sites are located approximately 20km offshore. Figures 3-4(a) and (b) show the comparison of average wave height and wind speed at these locations. In these figures, the smaller black squares represent the approximate locations of the NL-1 and NL-3 sites and have an area of 50km^2 while the larger squares show an area of 200km^2.
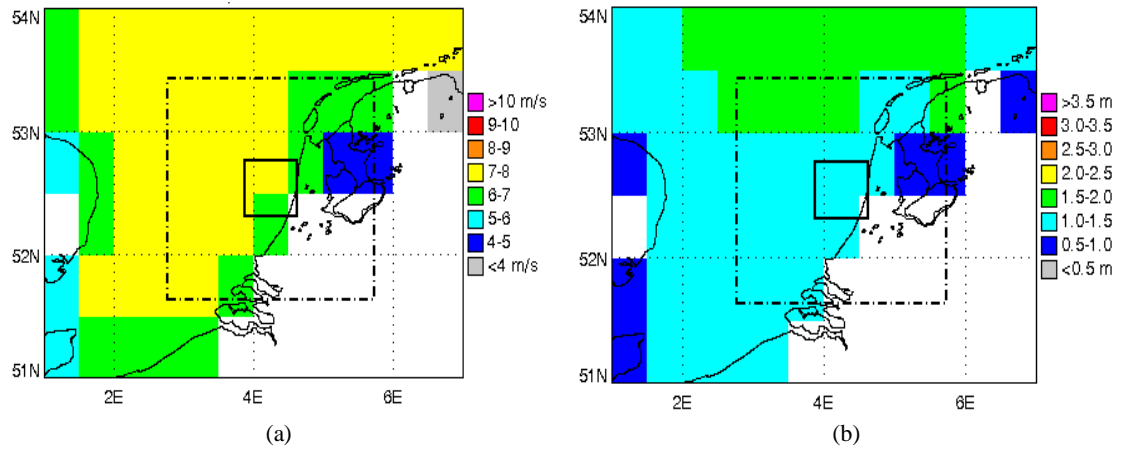
Figure 3-4. Environmental conditions in the Dutch territories of the North Sea: (a) average wind speed at the Dutch North Sea and (b) average wave height at the Dutch North Sea (Waveclimate.com, 2016).

As can be seen in Figure 3-3 and Figure 3-4, both sites are relatively close to each other and have similar environmental conditions. Also, both sites have similar water depths of approximately 20m. An established aero-elastic model is publicly available for the NREL 5MW wind turbine, which allows for aero-elastic calculations to be carried out and this is one of the reasons why the NREL 5MW wind turbine was selected as the reference for this study. Although the NREL 5MW wind turbine is considered to be located on the NL-3 site, a set of environmental states that have been proposed by Tempel (2006) for the NL-1 site, which has similar environmental conditions to this site, as shown in Figure 3-4, is adopted for the subsequent fatigue calculations.

Table 3-3 includes the soil profile data applied for the 5MW wind turbine (Nehal, 2001). Due to poor data quality for NL-3, Nehal (2001) used the soil profile obtained at a location close to NL-7 in their calculations, which is also adopted here for consistency. According to Nehal (2001), the top layer of the soil in Table 3-3 consists of loose sand and is prone to scour. The 3MW Opti-OWECS wind turbine is designed based on the borehole readings for NL-1 up to 30m depth. Table 3-4 shows the soil properties suggested by Zaaijer (2005) for this offshore wind turbine. As both sites are relatively nearby some of the parameter values are interpolated based on the values in Table 3-3, assuming that they consist of similar soil types.

Table 3-3. Soil layers' parameters for NL-7, based on the data by Nehal (2001).

Soil layer	Layer description	Υ_{sat} (kN/m^3)	c' (kN/m^2)	ϕ'	δ'	E_{50} (kN/m^2)
0m to -15m	Sand waves	17	0-1	27.5	18	n.a
-15m to -20m	Firm clay	19	5-10	20	13	7500
-20m to -25m	Fine to medium sand	19	0-1	32.5	21	60000
-25m to -65m	Fine to medium sand	19	0-1	35	23	80000

Table 3-4. Soil layers' parameters for NL-1, based on the data by Zaaijer (2005).

Soil layer	Layer description	Υ_{sat} (kN/m^3)	c' (kN/m^2)	ϕ'	δ'	E_{50} (kN/m^2)
0m to -12m	Medium sand	19	0-1	32.5	21	60000
-12m to -13m	Soft clay	19	5-10	20	13	7500
-13m to -30m	Dense sand	21	0-1	35	23	80000

The soil profile presented in Table 3-3 is used to model the soil support for the NREL 5MW wind turbine. As little to no information on the NREL 5MW turbine transition piece is available, the influence of this part on the static response and dynamic properties of the wind turbine was studied on the Opti-OWECS 3MW wind turbine, and the conclusions were cautiously broadened to the NREL 5MW wind turbine. In the following, the methodology used for the fatigue analysis of the reference wind turbine is explained.

3.3   Finite element modelling of the support structure

ABAQUS (Dassault Systèmes Simulia, 2012) was used for the structural finite element modelling and analysis. Different modelling techniques were applied in this research to study the fatigue of the reference wind turbine and investigate the effects of parameters such as soil-structure interaction, soil material nonlinearities, grout interface, and material nonlinearities under static and dynamic loads. In the following, an overview of the finite element modelling and analysis of the fatigue life is given. Details of the 3D finite element modelling and analysis procedures used in the study of soil-structure interaction and transition piece are given in the dedicated chapters (Chapters 4 and 5).

In general, the fatigue of the reference wind turbine was investigated using 2-D beam element models, which have a significant advantage in terms of computational speed for large models loaded with long load time histories.

Standard linear Timoshenko beam elements were used for the modelling of the wind turbine support structure. A convergence study was carried out to check that element size of 1/100 to 1/200 (1m to 0.5m length) yields a satisfactory convergence (i.e. an error of less than 0.5%) in the static lateral deflection and modal frequencies (1st and 2nd natural frequencies). Accordingly, element length of 0.5m was used to mesh the model.

A deformable beam was added with the length of 2.4m, corresponding to the offset distance of the rotor axis to the tower head, to account for this offset in rotor load applications. The mass of rotor and hub was modelled as a point mass at the top of this beam.

The influence of vertical soil support on the lateral modal behaviour of the wind turbine was checked, and the results led to the conclusion that the bottom of the monopile can be supported on a roller without influencing the lateral stiffness of the wind turbine structure.

In this research, the standard distributed-springs model was used to model the soil support. Soil properties were implemented on a layer-by-layer basis. The springs' stiffness were found from the standard p-y curves defined by Murchison and O'Neil (1984) and adopted by API (2007) and DNV (2013). The definition of p-y curves for cohesive and cohesionless soils can be found in Appendix-A and are discussed in Chapter 4.

The lateral soil support was modelled using 30 springs in the fatigue analysis. A detailed convergence study was carried out to determine the sensitivity of the static response and modal properties of the wind turbine to the number of springs in Chapter 4.

The distributed springs model is particularly useful when the scour effects are studied. Scour can simply be modelled by the removal of the top springs in the soil profile, depending on the scour depth. Also, the ultimate lateral resistance of soil (p_u) was reduced down to $6D_{pile}$ depth below the original seabed to consider the effects of overburden pressure reduction. For the model in which backfilling of the scour depth was considered, springs were replaced in the model with a modified p-y curve. The density of the material ($\gamma_{backfilled}$) for the backfilled portion of the scour depth was used to modify the p-y relationships.

3.4 Numerical procedures

The analysis of the reference wind turbine can be categorised into static and dynamic analyses. A static analysis was carried out to investigate the static effects of scour. Modal analysis was performed to examine the variations in the natural frequency and steady-state response of the system. The dynamic response of the nonlinear system to stochastic loading was studied using a dynamic implicit analysis. A sensitivity analysis was required to ensure the suitability of the time increments used. This study showed that a minimum increment size of 0.125s achieved convergence. To err on the side of safety, time increments of 0.1s were used for the dynamic implicit analysis in the fatigue analysis of the wind turbine. In this research, a one-hour simulation length was used. A preliminary study of fatigue damage sensitivity to simulation time confirmed that this was acceptable. Four hundred seconds were added at the start of the load time series and the corresponding simulation data was later discarded to avoid any potential initial transient effect. Numerical damping is normally applied by default in ABAQUS to stabilise the numerical scheme. This was set to zero as damping is a key factor for this study that needs to be controlled carefully. The stabilisation of the solution was achieved by applying damping explicitly in the model. Damping was applied in the model in the form of Rayleigh damping to represent the hydrodynamic, soil and structural damping and a dashpot for the aerodynamic damping, details of which are discussed further in Chapter 6. The Rayleigh parameters and constant of dashpot were tuned to obtain the desired level of damping in the first and second natural modes of the structure.

3.5 Calculation of environmental loads

Sea environments exert various types of forces on an offshore structure. These forces are mainly the wind, wave, and current loads. Wind and waves, by nature, are stochastic, while the current load is assumed to be primarily constant. Currents were included in the calculation of wave loads on the structure. However, the influence of static wind on the tower was not considered, as its effect was found to be negligible in the fatigue life. In this section, the methods used to compute the aerodynamic and hydrodynamic loads on the wind turbine is presented.

3.5.1 Aerodynamic loads

The aerodynamic load on the wind turbine can be subdivided into the drag force on the tower and the resultant rotor thrust on the nacelle. The rotor thrust is stochastic while the drag on the tower can be considered mostly static. The rotor thrust consists of a constant drag component (from mean velocity) and an unsteady component around the mean (from fluctuations about the mean velocity) (Arshad and O'Kelly, 2015).

The velocity of the wind increases with altitude due to the interaction of the wind with the surface. This phenomenon, which is known as wind shear, is present in the lower 2km of the atmosphere (Tempel, 2006). A logarithmic profile (Equation (3-1)) and a power law (Equation (3-2)) are two common methods to describe the wind shear phenomenon:

$$V_w = V_{w,r} \frac{\ln(\frac{z}{z_0})}{\ln(\frac{z_r}{z_0})}, \tag{3-1}$$

$$V_w = V_{w,r} \left(\frac{z}{z_r}\right)^{\alpha_{shear}}, \tag{3-2}$$

where z is the considered height from the mean sea level (MSL), z_r is the reference height at which $V_{w,r}$ is taken, z_0 is the surface roughness length (taken as 0.05 according to DNV (2013)) and α_{shear} is the power law coefficient (taken as 0.12 according to Burton et al. (2001)). Depending on the values used, each method leads to slightly different results, but both methods give similar results for the wind speed at the hub height. In this research, the logarithmic profile was used to interpolate the wind speed at the hub height of the NREL 5MW wind turbine, as it leads to more conservative loads.

The aerodynamic loads on the 5MW wind turbine were calculated using FAST, as it is capable of combining a model of the elastic support structure and blades with the aerodynamics and control system of the wind turbine. As a result, a high level of details of the turbine control system as well as the aerodynamic loads on the blades (called 'rotor thrust'), which are transferred from the blade roots to the rotor, could be incorporated in the time-domain dynamic analysis of the wind

turbine. The incoming wind field flow used by FAST is calculated by a turbulence simulation pre-processing module called TurbSim, also created by NREL (2015). Figure 3-5 shows the process of aerodynamic load calculation using TurbSim and FAST.
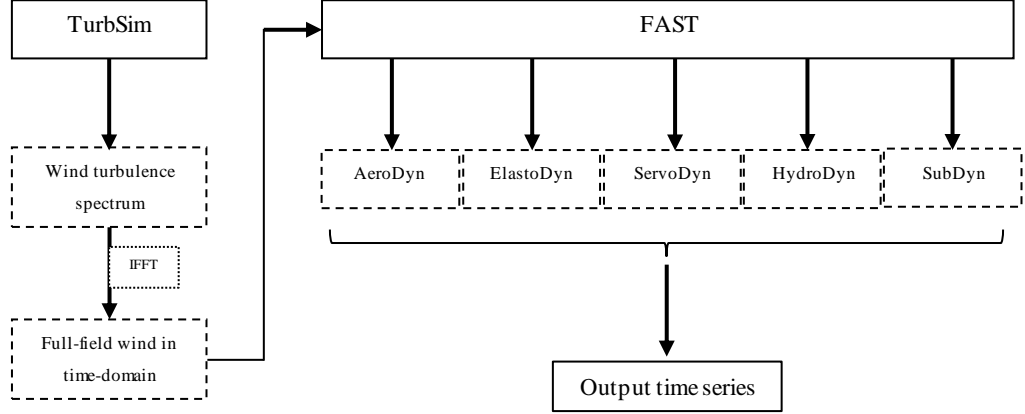
Figure 3-5. Simulation process using TurbSim and FAST for the turbulent wind thrust calculation. The solid lines represent the main simulation steps. The dashed lines in TurbSim represent the breakdown of simulations steps taken, while in FAST they represent different modules used to define the wind turbine and run the simulations.

The stochastic nature of the incoming wind is determined by specifying various input parameters in TurbSim. These include, the hub height, the reference mean wind speed and the height at which it was taken, the turbulence intensity profile and turbulence model. The Normal Turbulence Model (NTM) was used throughout, as suggested by IEC 61400-3 (2005) for power production load cases. The recommended IEC turbulence characteristic "B" was used in conjunction with the Kaimal turbulence model, defined in Equation (3-3).

$$S_{Kaimal}(f) = \frac{4\sigma_k^2 \left(L_k / V_w \right)}{\left(1 + 6f \left(L_k / V_w \right) \right)^{5/3}},$$
(3-3)

where σ_k is the standard deviation of the wind speed, L_k is the integral length scale, V_w is the mean wind speed and f is frequency (IEC, 2005).

The wind field around the rotor and blades was determined using a meshed grid of 180m, aimed at covering a 180m x 180m area around the rotor, as illustrated in Figure 3-6.
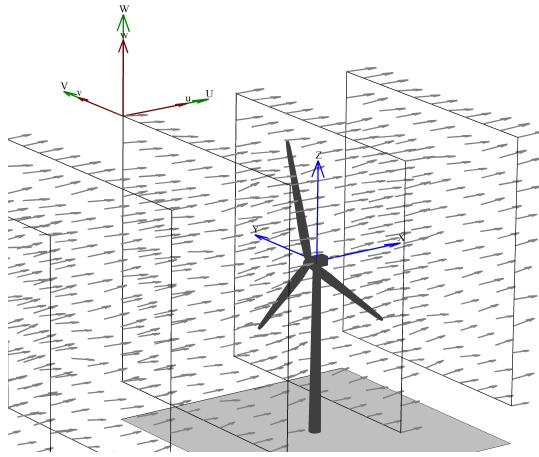
Figure 3-6. Example of TurbSim wind field grid which is used in AeroDyn (NREL, 2016).

The wind field generated by TurbSim is used by FAST for the aero-elastic simulations, as illustrated in Figure 3-5.

In practice, aerodynamic damping is the additional drag force caused by the oscillation of the support structure. The rotor thrust was calculated by constraining the tower and monopile to be rigid in FAST so that aerodynamic damping is not double counted. A similar approach has been used by various authors (Tempel, 2006; Alati *et al.*, 2014; Ziegler *et al.*, 2016). No blade pitch controlling system was allowed in the FAST analysis and, instead, the blade pitch angle was varied according to the mean wind speeds and kept constant during the simulations. Table 3-5 shows the blade pitch angles for wind/rotor speed correspondence in the 5MW reference wind turbine according to Jonkman at al. (2009). All simulations were carried out with a time increment of 0.05s. This time increment size was later interpolated by ABAQUS to match the specified increments for the dynamic analysis. In addition, simulation results were verified against the results obtained by Jonkman et al. (2009) whenever possible. In theory, the resultant wind thrust is caused by the sum of lift and drag forces on the rotating blades. The resultant rotor thrust was applied as a point load at the location of the hub (at the top of the deformable beam placed above the tower head) in the ABAQUS models.

Table 3-5. Rotor control and blade pitching properties for various wind speeds, according to Jonkman at al. (2009).

Wind speed (m/s)	Rotor speed (rpm)	Pitch angle (°)
3.0	5.7	0.00
4.0	7.0	0.00
6.0	8.0	0.00
8.0	9.0	0.00
10.0	10.0	0.00
11.4	12.1	0.00
12.0	12.1	3.83
13.0	12.1	6.60
14.0	12.1	8.70
15.0	12.1	10.45
16.0	12.1	12.06
17.0	12.1	13.54
18.0	12.1	14.92
19.0	12.1	16.23
20.0	12.1	17.47
21.0	12.1	18.70
22.0	12.1	19.94
23.0	12.1	21.18
24.0	12.1	22.35
25.0	12.1	23.47

3.5.2 Hydrodynamic loads

Sea waves result from the interaction of the wind with the sea surface. Spectral density functions of sea surface elevation can be employed to generate actual sea surface representations in the time domain (Chakrabarti, 2005). The sea surface elevation at a single point can be identified by H_s, significant wave height, and T_z, mean zero crossing period. H_s is the average height of the highest one-third waves in the short-term record and T_z is found by the ratio of the measurement time by the number of zero up-crossings (Tempel, 2006). Various spectra exist for the description of the random sea surface. Pierson and Moskowitz (1964) proposed a spectral density function of the sea surface by curve fitting the spectra on sea measurements of a fully developed sea. Equation (3-4) shows the definition of this spectral density function.

$$S_{PM}(f) = 0.3125 \cdot H_s{}^2 \cdot f_p{}^4 \cdot f^{-5} \cdot \exp\left[-1.25\left(\frac{f_p}{f}\right)^4\right],$$

$$(3\text{-}4)$$

where f_p is the peak frequency defined as $1/T_p$, and T_p for Pierson-Moskowitz spectrum is determined by $T_p=1.41T_z$. An extension to the Pierson-Moskowitz sea-surface spectral density, called the JONSWAP spectrum, was proposed by Hasselmann et al. (1973), and was precisely calibrated for North Sea conditions. The JONSWAP spectrum definition is given in Equation (3-5).

$$S_{JS}(f) = (1 - 0.287 \cdot \ln(\gamma)) \cdot S_{PM}(f) \cdot \gamma^{\exp\left[-\frac{(f-f_p)^2}{2\sigma^2 \cdot f_p{}^2}\right]}, \qquad (3\text{-}5)$$

where γ is the peak enhancement factor and σ is the spectral width parameter, both of which are defined below (Equations (3-6) and (3-7)). The definition of T_p, peak period, is different from that of Pierson-Moskowitz and is given in Equation (3-8). For the North Sea, the suggested value of γ is 3.3 (also adopted here). Using $\gamma=1$ returns this spectrum back to Pierson-Moskowitz.

$$\gamma = \begin{cases} 5 & for \ \dfrac{T_p}{\sqrt{H_s}} \leq 3.6 \\ \exp\left(5.75 - 1.15\dfrac{T_p}{\sqrt{H_s}}\right) & for \ 3.6 < \dfrac{T_p}{\sqrt{H_s}} \leq 5, \\ 1 & for \ 5 < \dfrac{T_p}{\sqrt{H_s}} \end{cases}$$

(3-6)

$$\sigma = \begin{cases} 0.7 & for \ f \leq f_p \\ 0.9 & for \ f > f_p \end{cases},$$

(3-7)

$$T_z = T_p \sqrt{\dfrac{5+\gamma}{11+\gamma}} = 0.76 T_p.$$

(3-8)

A comparison between Pierson-Moskowitz and JONSWAP spectra is given in Figure 3-7. JONSWAP spectrum with a peak enhancement factor $\gamma=3.3$ results in a higher and narrower peak than Pierson-Moskowitz in the spectra. This results in a higher sea surface elevation and leads to a higher loading on the structure. Although both spectra are widely used for the design of the offshore structures, JONSWAP spectrum is the preferred option for North Sea structures. It should be noted that various spectra for surface elevation have been developed over the past decades, and the choice of the suitable spectrum is up to the designer (Benitz, Lackner and Schmidt, 2015). Nevertheless, Pierson-Moskowitz and JONSWAP spectra are both recommended for use by DNV (2013) and other design guidelines. In this research, the JONSWAP spectrum was used.
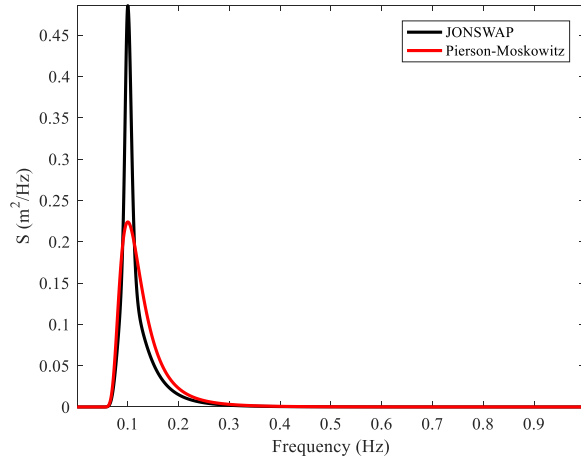
Figure 3-7. Comparison of Pierson-Moskowitz spectrum with JONSWAP spectrum with γ=3.3.

The power spectral density of the sea surface elevation can be transformed into amplitude spectrum according to Equation (3-9).

$$a_n = \sqrt{2S_{JS}(f_n)\Delta f}, \qquad (3\text{-}9)$$

where a_n is the wave amplitude, $S_{JS}(f_n)$ is the surface elevation spectra associated with the nth component of frequency and Δf is the frequency increments. Various wave theories exist to describe the motion of water particles in a random sea. Linear (Airy) wave theory is the most commonly applied theory for the description of the water particle motion, especially for the fatigue limit state analysis (Chakrabarti, 2005). In this theory, water particles follow a harmonic pattern in their motion. Particles motion is described by a linear relationship between the motion components and wave height. Other wave theories exist, which take into account the higher orders of dependency of water particle motion on the wave height. Figure 3-8 shows regions of applicability of various wave theories. In the wave load calculation, H is the wave height, T is the wave period, L corresponds to wave length and d is the sea depth.
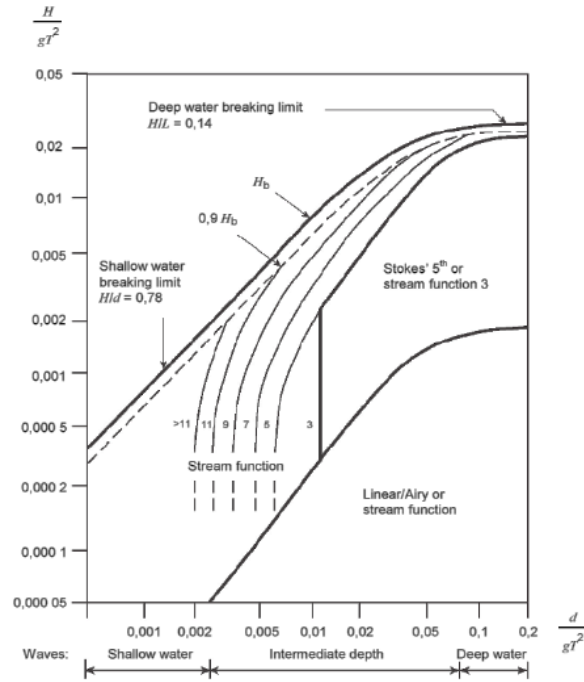
Figure 3-8. Applicability of different wave theories (IEC, 2009).

Depending on the wave theory applied, the velocity and acceleration components of the water particles may differ. Although linear wave theory is more suitable for deep waters, Veldkamp and Tempel (2005) showed that consideration of higher order waves does not show a significant advantage for fatigue load levels. However, Veldkamp and Tempel (2005) and Agarwal and Manuel (2008) showed that for extreme waves the difference between linear and nonlinear wave theories can grow to 25%. Marino, Lungi and Borri (2013) also found a good match between the linear and nonlinear wave models in an operational wind turbine. Nevertheless, linear wave theory is the most commonly practiced theory for the simulation of hydrodynamic loads and was used to calculate the wave loads on the structure in this research.
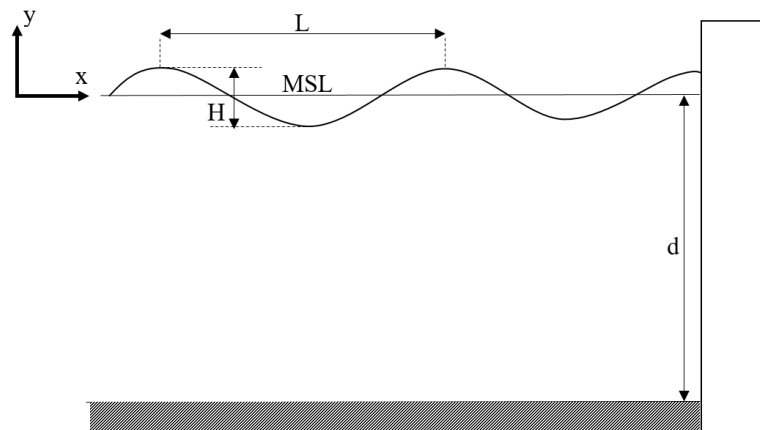
Figure 3-9. Two dimensional wave motion around a cylinder (i.e. pile) over a flat seabed showing the sea surface (mean sea level (MSL)), wave height (H) and length (L), and sea depth (d).

64

According to Chakrabarti (2005), for the linear (Airy) wave theory the wave profile, horizontal wave particle velocity, and acceleration are defined by Equations (3-10), (3-11) and (3-12):

$$\eta(x,t) = \sum_{n=1}^{N} a_n \cos[(k_n(x - c_n t)) + \varepsilon_n], \tag{3-10}$$

$$u(x,y,t) = \sum_{n=1}^{N} \frac{a_n \omega_n}{\sinh k_n d} \cosh[k_n(y + d)] \cos[k_n(x - c_n t) + \varepsilon_n], \tag{3-11}$$

$$\dot{u}(x,y,t) = \sum_{n=1}^{N} \frac{a_n \omega_n^2}{\sinh k_n d} \cosh[k_n(y + d)] \sin[k_n(x - c_n t) + \varepsilon_n], \tag{3-12}$$

where y is the depth below the mean sea level (negative downwards), t is time, c is the wave celerity, a_n is the wave amplitude (i.e. $H/2$), ω_n is the wave frequency, k_n refers to wave number, and ε_n is the random phase associated with the nth component of the surface elevation spectrum, as sketched in Figure 3-9. Wheeler stretching is also applied to these equations to account for the variation of the mean sea surface. This is done by replacing the term "y" with "$y/(1 + \eta/d)$" in the relative wave velocity and acceleration equations (i.e. (3-11) and (3-12)) for above sea depth components.

The wave force on the vertical pile was calculated by Morison's equation, which consists of a drag and an inertia component, as shown in Equation (3-13).

$$F(x,y,t) = \underbrace{\rho C_M \frac{\pi D_{pile}^2}{4} \dot{u}(x,y,t)}_{Inertia\ component} + \underbrace{\frac{1}{2} \rho D_{pile} C_D |u(x,y,t)| u(x,y,t)}_{Drag\ component}, \tag{3-13}$$

where ρ is density, C_M and C_D are inertia and drag coefficients, D_{pile} is the pile diameter, u is wave velocity and $\dot{u}$ is wave acceleration. Values of 2.0 and 1.0 were adopted following Agarwal and Manuel (2008) for the inertia and drag coefficients, respectively. The reference wind turbine in their work is the same as that in this research. According to Chakrabarti (2005), Morison's equation is valid for cases where the diameter of the structure is small relative to the wavelength. However, for large diameter structures (e.g. monopiles) in shallow to intermediate water depths, where the wavelength is significantly reduced, the presence of the structure alters the form of incident waves, called the diffraction effect. The limit for the applicability of Morison's equation is $D_{pile}/\lambda < 0.2$, where λ is the wavelength. The influence of diffraction, however, can be incorporated into Morison's equation by reducing the inertia coefficient using the MacCamy-Fuchs diffraction correction factor (Tempel, 2006). Figure 3-10 shows the reduction of the inertia

coefficient due to diffraction effects for different values of D/λ_0. As the wavelength increases relative to the monopile diameter, the inertia coefficient value approximates to the value proposed and used by Agarwal (2008) (i.e. C_m=2.0).
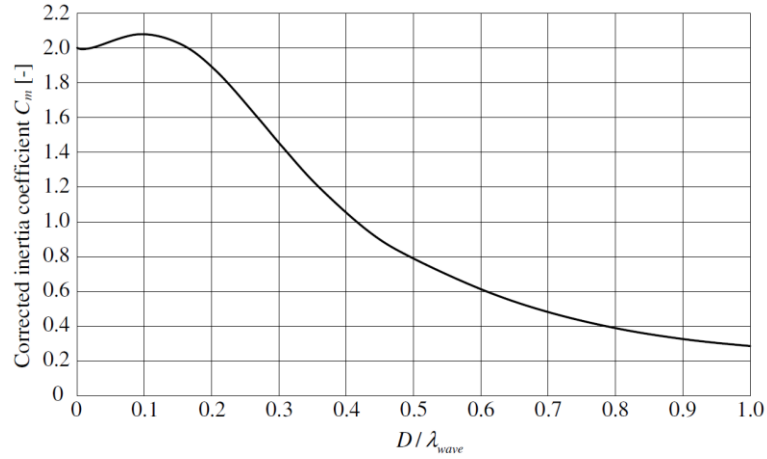
Figure 3-10. MacCamy-Fuchs inertia coefficient (C_m) correction for different ratios of pile diameter and wave length (Tempel, 2006).

For the structural configuration considered here, the inertia component of the wave loading is dominant compared to the drag component. Table 3-6 shows the ratio of the pile diameter to wavelength for different wave periods, which are likely to occur at the considered location, as shown later (Table 3-7). The over-estimation of the inertia coefficient (by assuming constant C_m=2.0), which is directly linked to the diffraction effects and increases the inertia component of the hydrodynamic loading, is shown at the right column of Table 3-6.

Table 3-6. Level of overestimation of the wave load inertia component for various wave period/length values.

T (s)	λ_0 (m)	D/λ_0	$\frac{c_m}{c_{m=2.0}}$ (%)
3	14	0.43	-50%
4	25	0.24	-13%
5	39	0.15	+2%
6	56	0.11	+3%

As shown in Table 3-6, the inertia component of the wave loading is reduced by up to 50% when the diffraction effects are considered. This corresponds to the calmer sea states when the wavelength is small compared to the pile diameter. However, for higher wavelengths (i.e. for wave periods of 5s and 6s) the assumed constant inertia coefficient is accurate to within 2-3%. Using a constant inertia coefficient of C_m=2.0 results in an over-conservative fatigue damage and will be discussed in Chapter 6 and Appendix-C.

The effect of currents on the wave force was considered by adding the mean current velocity to the water particle velocities in the drag component of the wave load, as the current results in a

static lateral force on the cylinder. Equation (3-14) shows the modified drag component in Morison's equation:

$$F_{Drag} = \frac{1}{2}\rho D_{pile} C_D |u(x,y,t) + U_c(y)|(u(x,y,t) + U_c(y)),$$

(3-14)

where U_c refers to the current velocity and is defined by Equation (3-15):

$$U_c(y) = U_{c0}(\frac{y+d}{d})^{\alpha_{current}},$$

(3-15)

where U_{c0} refers to surface current velocity, y is the depth negative downwards from the mean sea level, d is the average sea depth and $\alpha_{current}$ is the current exponent taken as 1/7 (Tempel, 2006). The wave force was calculated for every sea state based on the corresponding parameters of the sea wave. These parameters are defined along with wind parameters in section 3.6.

The hydrodynamic added mass was also applied to the submerged part of the wind turbine using the simplified method proposed by Goyal and Chopra (1989), in which the added hydrodynamic mass is determined based on the added mass for an infinitely long uniform pile defined by Equation (3-16) and the ratio r_0/d. ρ_w is water density, r_0 is the outer radius of the pile and d is the water depth.

$$m_\infty^0 = \rho_w \pi r_0^2$$

(3-16)

The influence of inertia forces caused by the added mass was initially examined using FAST and its contribution to the total hydrodynamic loads was found to be insignificant. Thus, this component of the hydrodynamic load was not considered further in the calculations.

3.6   Fatigue analysis

The fatigue analysis of the wind turbine support structure was done using the results from the time-domain dynamic simulations, based on a set of loading scenarios referred to as load cases. The description of the load cases is given in section 3.6.1. According to DNV (2014), fatigue damage must be considered in connection details (i.e. welded or bolted details) and the nominal or hotspot stresses must be compared with the appropriate S-N curves. DNV (2014) recommends a range of S-N curves based on single amplitude cyclic loads. As the loads are random, the dynamic response of the offshore wind turbine contains variable amplitude stresses. Therefore, these cycles of various amplitudes in the response must be counted to be able to calculate the cumulative fatigue damage. Rainflow counting was used for cycle counting the stress signals. Figure 3-11 shows the process associated with the fatigue life calculation for a given stress signal

in the time-domain. An overview of rainflow counting and fatigue life calculation processes is provided in sections 3.6.2 and 3.6.3.
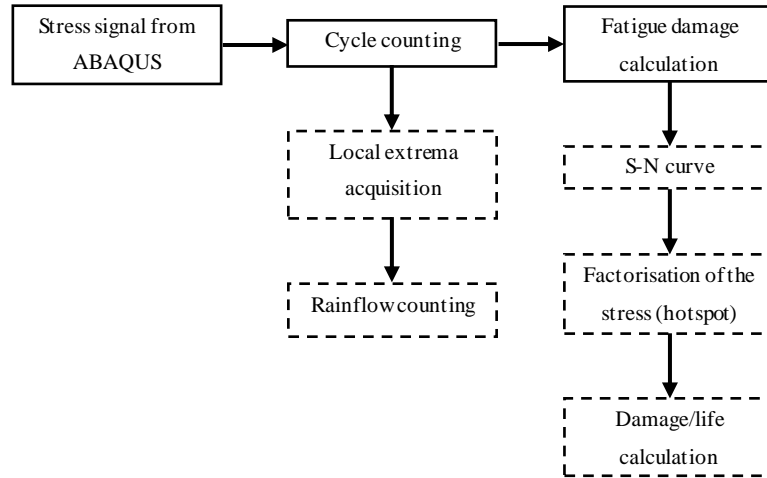
Figure 3-11. Fatigue calculations procedure overview in MATLAB. Solid lines represent the main phases involved in the fatigue life calculation process and dashed lines are the steps taken at each phase.

3.6.1 Description of the environmental conditions and load cases

The standard fatigue analysis of offshore wind turbine involves the consideration of the operational and non-operational wind and wave loads. Turbine start-up and shutdown load cases are other aspects to be considered when offshore wind turbines are designed for fatigue (IEC, 2005). However, wind turbines spend the majority of their service life in operation. Therefore, in this research, the fatigue analysis was focused on a fully operational turbine. In this case, the aerodynamic damping of the turbine is also existent which has a significant energy dissipative effect on the vibration of the system. This will be investigated in depth in Chapter 6.

Well-established sets of representative environmental states for NL-1 are provided in multiple studies (Ferguson *et al.*, 1998; Tempel, 2006). By contrast, the availability of environmental conditions for the original site for the NREL 5MW wind turbine was poor. However, as shown in Figure 3-4, the environmental conditions at NL-1 and NL-3 are very similar. This was a driving factor for adopting an alternative reference site's characteristics for the wind turbine in this research, as explained in section 3.2.

Environmental states are derived from scatter diagrams of wave periods and heights and their probability of occurrence during a representative period of time. The scatter diagrams usually produce an impractical number of correlated wave heights, periods and wind speeds, which would ideally form the number of loading scenarios considered for fatigue analysis. However, this number can be reduced by combining these environmental states into similar mean states with a joint probability of occurrence, particularly in the preliminary stages of the design. In this

research, the environmental loading scenarios were adopted from the NESS-NEXT data available to Tempel (2006), which were binned into wave heights of 0.5m and zero-crossing periods of 1s. A total of 22 environmental states are summarised in Table 3-7, which were adopted from Tempel (2006). The environmental states obtained from Tempel (2006) are in good agreement with similar environmental states tables produced by Ferguson et al. (1998). It should be noted that all environmental states are in the operational range for the NREL 5MW wind turbine, adding up to 91% of probability of occurrence. Figure 3-12(a) and (b) show the probability of occurrence of the environmental states based on the wind speeds and combined wind and wave states, respectively. According to these charts, the environmental states with wind speeds ranging from 6 m/s to 12 m/s have the highest probabilities of occurrence. Combining the wave states into Figure 3-12(a) results in the probabilities of occurrence of the complete set of environmental states, as presented in Table 3-7. It can be concluded from these figures that the majority of the remaining 9% of the environmental states' probabilities of occurrence correspond to those with a wind speed below cut-off (i.e. low wave height and period and wind speed), which should not cause significant fatigue damage.

Table 3-7. Environmental states used in this research (for NL-1), adopted from (Tempel, 2006).

State	V_W (m/s)	T_Z (s)	H_S (m)	P_{State} (%)
1	4	3	0.5	3.95
2	4	4	0.5	3.21
3	6	3	0.5	11.17
4	6	4	0.5	7.22
5	8	3	0.5	11.45
6	8	4	1.0	8.68
7	10	3	0.5	5.31
8	10	4	1.0	11.33
9	12	4	1.0	5.86
10	12	4	1.5	6.00
11	14	4	1.5	4.48
12	14	5	2.0	3.26
13	16	4	2.0	1.79
14	16	5	2.5	3.10
15	18	5	2.5	1.74
16	18	5	3.0	0.80
17	20	5	2.5	0.43
18	20	5	3.0	1.14
19	22	5	3.0	0.40
20	22	6	4.0	0.29
21	24	5	3.5	0.15
22	24	6	4.0	0.10

According to Ferguson et al. (1998), the misalignment between the wind and wave at this particular site is minor. DNV guidelines (2013) state that in some cases (e.g. perpendicular wind and wave loads), the misalignment can lead to increased cross-wind response. In the cases where the misalignment of environmental loads is small, a co-linear (i.e. unidirectional) assumption is

considered to be conservative (Tarp-Johansen *et al.*, 2009) and this was assumed throughout this project.

(a)   (b)
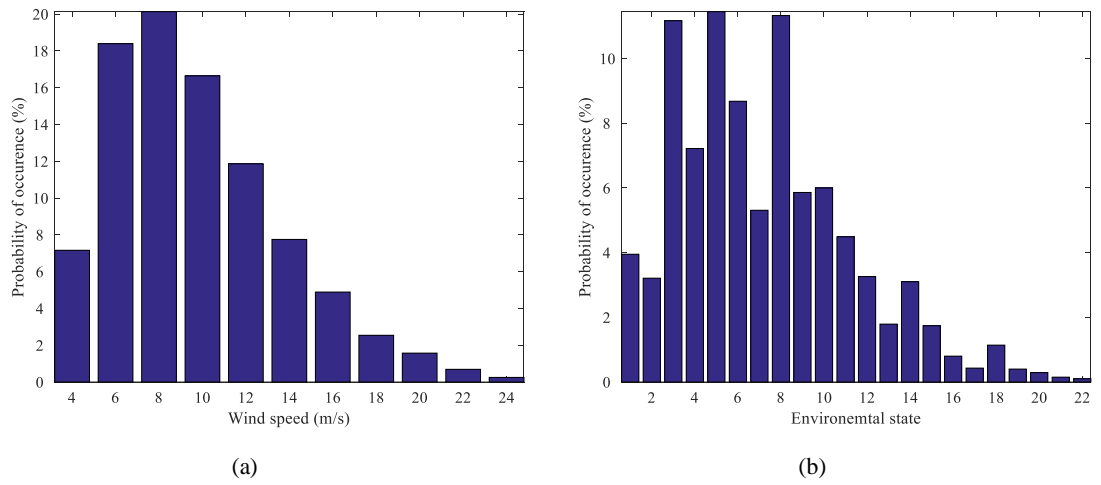
Figure 3-12. The Probability of occurrence of (a) the wind states and (b) the environmental states.

3.6.2   Rainflow counting

Rainflow counting is a tool for the cycle counting of random stress signals in the time domain. This method of cycle counting was established by Matsuishi and Endo (1968). This algorithm takes its name due to its resemblance to a drop of rain flowing down the stress history when the stress history is rotated, as shown in Figure 3-13. In rainflow counting, cycle counting starts at the beginning of the signal and the procedure is commenced from one local extreme to another. Local extremes in a signal could either be a peak or valley, as indicated in Figure 3-13(a).

(a)   (b)
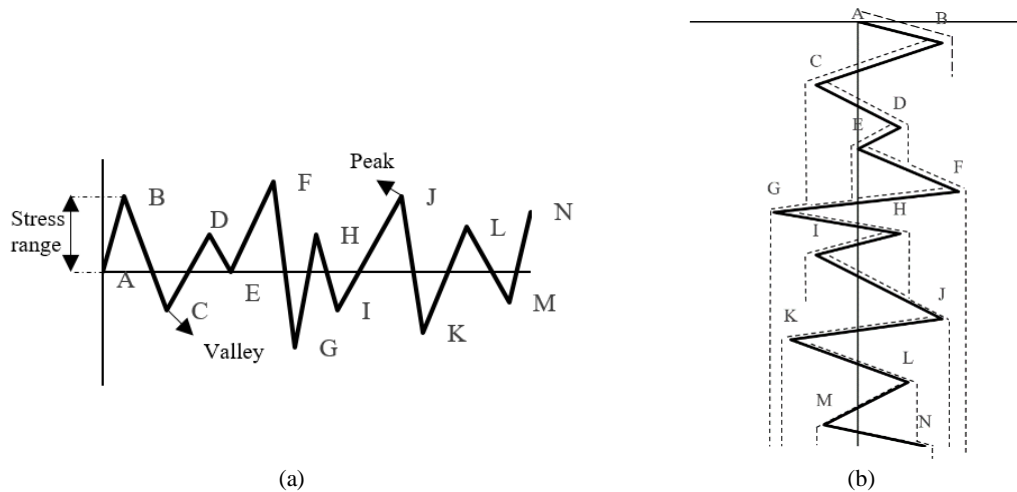
Figure 3-13. (a) Example of a random signal with labelled peaks and valleys, showing the stress range of a peak and (b) Example of the rainflow counting procedure for the signal.

The procedure of rainflow counting is described in ASTM (2011). In this research, a MATLAB rainflow counting toolbox created by Niesłony (2009) was used. This toolbox was initally

developed for fatigue life analysis of machine components according to ASTM (2011) rainflow counting procedure.

3.6.3   Fatigue damage calculation

The fatigue damage was considered at the location of maximum stress at a hypothetical welding point. Design guidelines provide a recommended practice for the fatigue life calculation of offshore wind turbines that is followed here.

- Calculation of fatigue strength:

S-N curves are defined in log-log scale as shown in Equation (3-17), where N refers to the number of cycles to failure, $log(\bar{a})$ corresponds to the intercept of $log(N)$ axis, $\Delta\sigma$ is the stress range in MPa and m is the negative inverse slope of the curve.

(3-17)

$$\log(N) = \log(\bar{a}) - m\log(\Delta\sigma).$$

Various other quantities are required in the fatigue damage calculation of a section. These include thickness effects, mean stress effects, and stress concentration factors for hotspots (e.g. joints). For a given stress range, a revised version of the S-N relationship, which considered thickness effects, is shown in Equation (3-18), where t is the thickness through which a crack is likely to grow (i.e. thickness of the monopile), t_{ref} is the reference thickness taken as 25mm, k is the thickness component and SCF is the stress concentration factor.

$$\log(N) = \log(\bar{a}) - m\log\left((\Delta\sigma(SCF))\left(\frac{t}{t_{ref}}\right)^k\right). \qquad \text{(3-18)}$$

Brennan and Tavares (2014) studied the application of stress concentrations factor and thickness effect correction ($\left(\frac{t}{t_{ref}}\right)^k$) in offshore wind turbine monopiles and concluded that applying these factors can lead to over-conservatism, but they were considered in the fatigue calculations in this research to be consistent with the guidelines.

Different S-N curves are defined depending on the structural detail type and its surrounding environment. According to Ziegler et al. (2016) circumferential butt welds are more applicable to offshore wind turbine monopiles compared to oil and gas structures. Therefore, in this research, structural detail class E was considered for the transition of weld to base material on the outside of girth welds in monopiles, as recommended by DNV (2014). The parameters for the corresponding S-N curve in seawater with cathodic protection are given in Table 3-8.

Table 3-8. S-N curve parameters for structural detail class E, according to DNV (2014).

N ≤ 10^6		N ≥ 10^6		Thickness component	Hotspot consideration
Log($\bar{a}_1$)	m_1	Log($\bar{a}_2$)	m_2	k	SCF
11.61	3.0	15.35	5.0	0.2	1.13

m_1 and m_2 are the respective negative inverse slopes and a_1 and a_2 are the corresponding intercepts of the bilinear curve. Figure 3-14 shows the "raw" S-N curve for structural detail class E (Equation (3-17)); the thickness effect, and stress concentration factor were applied in the process of fatigue damage calculations in MATLAB.
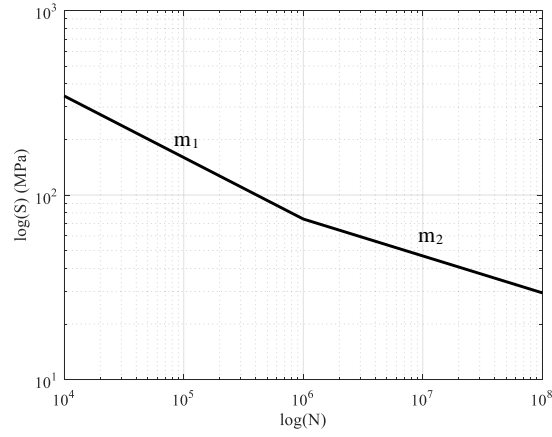
Figure 3-14. S-N curve for structural detail class E.

Mean stress effects do not need to be considered for fatigue analysis of the welded connections, however, for non-welded joints the Gerber parabola must be used, which according to Schijve (2009), includes the ultimate stress in metals (quadratic relationship) as a relatively accurate method of realisation of mean stress effects for fatigue analysis. For a certain fatigue life, this relationship is shown in Equation (3-19).

$$\frac{\Delta\sigma_N}{(\Delta\sigma_N)_{\bar{\sigma}=0}} = 1 - \left(\frac{\sigma_m}{\sigma_U}\right)^2,$$

(3-19)

where σ_m is the mean stress, σ_U is the ultimate stress of the material and $(\Delta\sigma_N)_{\bar{\sigma}=0}$ is the stress without the consideration of mean effects. In this research, fatigue endurance was considered at hypothetical welded connections, which did not require the application of mean stress effects.

For a variable amplitude loading, the fatigue damage is calculated according to Palmgren-Miner sum rule (P-M), which states that the fatigue damage for the environmental state k is the sum of damage caused by every stress range, which is determined by dividing the number of cycles

within this stress range by the number of cycles to failure for that stress range, as expressed in Equation (3-20).

$$D_k = \sum_{i=1}^{N_c} \frac{n_i}{N_i},$$

(3-20)

where N_c corresponds to the total number of stress bins counted over the stress time history, n_i is the number of cycles for stress range i and N_i is the number of cycles to failure for stress range i. A total damage of one corresponds to fatigue failure. Combining the fatigue damage with a rearranged Equation (3-17), the fatigue damage can be re-written as:

$$D_k = \frac{1}{\bar{a}_j} \sum_{i=1}^{N_c} \left[n_p \times \left(\Delta\sigma_{i(factored)} \right)^{m_j} \right],$$

(3-21)

where j refers to the corresponding section of the bi-linear S-N curve depending on the stress level and the factored subscript for the stress corresponds to the application of stress concentration factor and thickness effects to stress range i. The corresponding segment of the bi-linear S-N was found for every stress range, i, and the mean effect of the stress range was also considered.

The damage required in one hour of simulation that would lead to a total damage of 1 over 20 years (failure according to PM sum rule) is $D_{ref}^{1hr} = \frac{1hr}{20\,years} \times 1$. D_{ref}^{1hr} is used as a reference to normalise the damage calculated for each environmental state.

As each environmental state k has a different probability of occurrence p_k, the normalised contribution of the environmental state k to the total fatigue damage is $DC_k = \frac{D_k}{D_{ref}^{1hr}} p_k$ and the total normalised fatigue damage is obtained by summing each damage contribution according to Equation (3-22):

$$D = \sum_{k=1}^{N_k} DC_k.$$

(3-22)

The fatigue life of the monopile is then calculated according to Equation (3-23):

$$Fatigue\ life = \frac{20\ years}{D}.$$

(3-23)

Fatigue damage calculation was verified using a 300s harmonic loading simulation. The fatigue damage was calculated using the rainflow counting and fatigue life calculation MATLAB scripts and compared and verified with the hand-calculated damage/life. This verification is provided in Appendix-B. Using this methodology, the fatigue life of the reference turbine system was

predicted for various levels of aerodynamic damping, operational regimes, scour and backfilling scenarios.

4 Soil-structure Interaction

Calculation of fatigue life in the time-domain requires extensive simulations, and so large finite element models are not practical to be used, which is the reason for selecting beam element models with p-y curves. However, the soil-structure interaction can affect the dynamics and, hence, the fatigue of offshore structures. DNV (2013) recommends that caution must be taken for the fatigue limit state analysis of wind turbines with p-y curves, especially for their initial stiffness. In this chapter, the sensitivity of the static response and modal properties of the wind turbine support structure to the finite element modelling of the soil-structure interaction is examined.

The finite element modelling techniques and soil types used in this chapter are described in section 4.1. Verification of the models is presented in section 4.2. The comparison of the response of the system to static loading along with the modal variations are discussed in section 4.3. Finally, a summary of the results is presented in section 4.4.

4.1 Finite element modelling

The influence of finite element modelling of the NREL 5MW wind turbine was studied using beam and solid element models, as shown in Figures 4-1(a) and (b). In the beam element models, the effect of discretisation of the soil profile into layers, represented by springs, was studied. These are shown in Table 4-1. The effect of soil block/cylinder boundaries was examined in the 3D solid element model of the wind turbine. The block diameters considered are presented in

Table 4-2, expressed in terms of the pile diameter (D_{pile}=6m).

Table 4-1. Soil profile discretisation in the beam element model of the NREL 5MW wind turbine.

Model	Number of springs	Discretised layers' depths (m)
BE-1	3	15
BE-2	5	9
BE-3	9	5
BE-4	15	3
BE-5	30	1.5

Table 4-2. Soil block/cylinder boundaries in the solid element model of the NREL 5MW wind turbine.

Model	Soil block diameter	Soil block depth below monopile
SE-1	$3D_{pile}$	$2.5D_{pile}$
SE-2	$6D_{pile}$	$2.5D_{pile}$
SE-3	$12D_{pile}$	$2.5D_{pile}$
SE-4	$18D_{pile}$	$2.5D_{pile}$

As stated in Chapter 3, Timoshenko beam elements of 0.5m length were implemented for the modelling of the offshore wind turbine support structure in the beam element models. Eight-node linear solid elements were used for the modelling of the 3D models. In the 3D models, the pile and tower parts were meshed using two elements through thickness with a length of 0.5m. The size of elements in the soil cylinder (block) was variable based on the dimensions of the block. In the soil cylinder size of $3D_{pile}$, the outer boundaries were meshed using 0.8m elements. For the larger soil blocks, the size of elements at the outer boundaries scaled up more or less proportionally (e.g. the $6D_{pile}$ block was meshed using approximately 1.5m elements at the outer boundaries and so on). The interface between the soil and pile in all blocks was meshed with approximately 0.5m elements at the circumference. The sensitivity of offshore wind turbine's stiffness to smaller mesh size was examined and found to be negligible. The bottom boundary of the soil block was 15m below the pile and was supported on pins, while roller was used for the side boundaries.

In practice, a soil profile may consist of different soil types. A homogeneous soil profile was considered in this analysis for the sake of simplicity. A uniform assumption to study soil-pile interaction is commonly implemented in the literature (Achmus and Abdel-Rahman, 2005; Alexander and Bhattacharya, 2011; Kuo, Achmus and Abdel-rahman, 2012; Byrne *et al.*, 2015; Zdravković *et al.*, 2015). As shown in Table 3-1, the soil profile at the location of the NREL 5MW wind turbine mostly consists of cohesionless soil. Thus, in this study, the various cohesionless soil types that were present at this site (from loose to dense sand) were considered homogeneously to investigate the profile numerical modelling effects on the lateral and rotational stiffness of the wind turbine. Table 4-3 shows the types of soil considered for this analysis, where φ is the angle of friction, γ_{sat} is the saturated unit weight, E_{50} is the elastic modulus, and v is the Poisson ratio of the soil. The soil properties presented here are based on the data given by Nehal (2001). As this information is not complete in some cases, the best estimates for the soil parameters (e.g. elastic modulus) were used. In the following, the angle of friction of the soil will also be used as a representative for the soil type.

Table 4-3. Different soil profiles considered in this research based on the types of soil at the location of the NREL 5MW wind turbine.

Soil types	φ (°)	γ_{sat} (kN/m³)	E_{50}(MPa)	v
Loose sand to medium-dense sand-1	27.5	17	20	0.3
	30.0	18	45	0.3
Medium dense sand-2 to dense sand	32.5	19	60	0.3
	35	19	80	0.3

Figures 4-1(a) and (b) show the beam and solid element models of the wind turbine in ABAQUS, respectively. The lateral springs in the beam element model are highlighted in Figure 4-1(a). Two point loads of 1MN were applied: one at the mean sea level representing the waves, one at the

rotor height representing the wind, as shown in Figures 4-1(a) and (b). In the solid element models, the point loads were uniformly distributed at the surface of the support structure at the respective levels. The vertical load from turbine weight, which is positioned at the top of the tower, was also taken into consideration by the application of gravity. In this research, the longitudinal stress in the pile, the lateral displacement at the mudline and tower top along with tower top rotation were measured, as indicated in Figure 4-1(c).
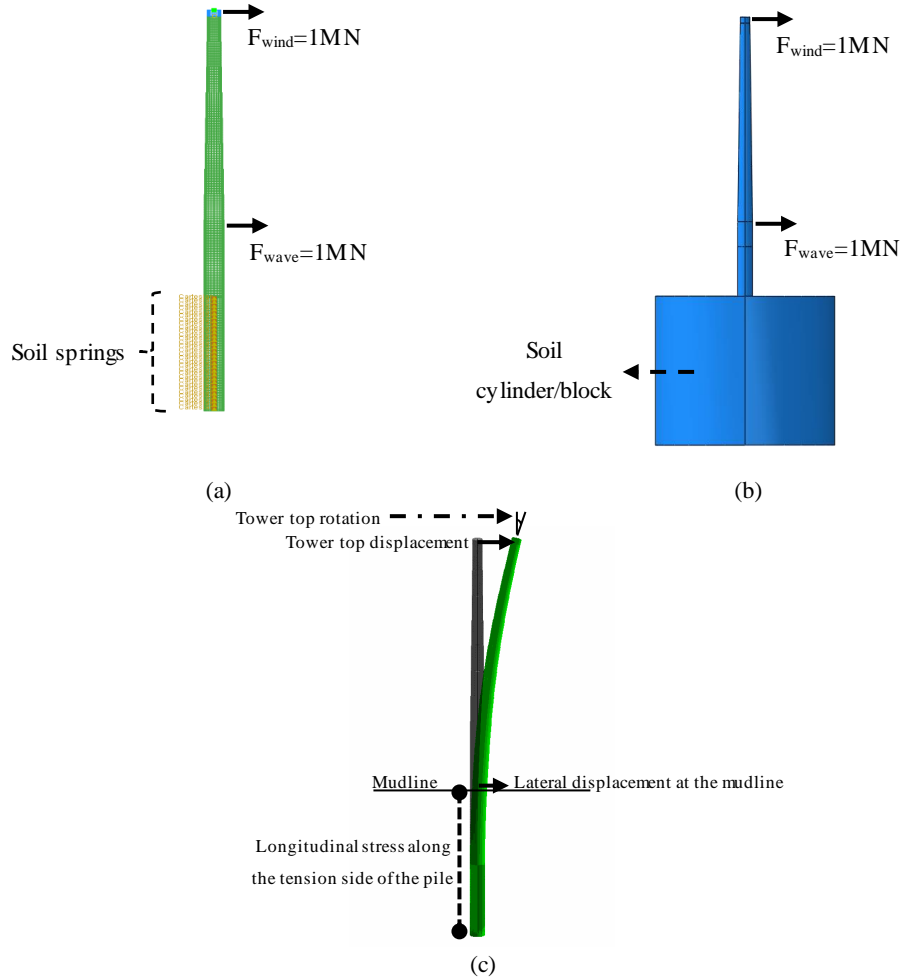
Figure 4-1. Sketch of (a) the beam element model of the wind turbine with lateral springs and the applied loads, (b) the solid element model of the wind turbine with the soil block/cylinder and the applied loads and (c) the deflected shape and measurements' locations.

General static step was used in the static studies, in which the load was ramped up in one second and the incrementation of the step was controlled by setting a maximum limit of 0.1s. The monopile and tower were modelled using elastic materials. This is mainly because yielding of the steel section under operational loads is very unlikely to occur (Kampitsis *et al.*, 2015). In the beam element models, the nonlinear p-y curves were defined according to DNV (2013) recommended practice (shown in Appendix-A). Elastic and Mohr-Coulomb material definitions were used in turn to investigate the effects of soil nonlinearities on the lateral and rotational stiffness of the wind turbine structure in the 3D models. A small amount of cohesion (*c*) of 0.1kPa was applied in the Mohr-Coulomb models to stabilise the 3D models initially, similar to Abdel-Rahman and

Achmus (2005). The interface between soil and pile was modelled using the Coulomb friction with μ=0.4, which is typically used for the soil-pile interaction (Achmus and Abdel-Rahman, 2005). The inside of the pile was filled with soil of the same type as the soil used in the soil block. For the contact region at the bottom of the monopile with the soil, normal (i.e. perpendicular surface) contact was assumed to be sufficient. In all surface interactions the selection of the master and slave surface determines which surface penetrates the other between the nodes, with the slave surface being the penetrable surface. The choice of master and slave surfaces was made based on the relative elastic moduli of the sections in contact following ABAQUS documentation (2012).

4.2 Verification of the finite element modelling

This section aims to verify the finite element modelling of the reference wind turbine by comparing the solid and beam element models. The solid element model of the wind turbine with a soil elastic modulus of E_s=80MPa is compared against the beam element model of the wind turbine with a constant spring stiffness applied through the penetrated depth, which results in the closest match between the beam and solid element models. Static analysis of the wind turbine was performed for two load application scenarios; only lateral loads, and lateral and gravity loads applied. Figures 4-2(a) and (b) show the comparison between the lateral deflections of the pile below the mudline in the beam and solid element models without and with the application of gravitational loads, respectively.

| (a) | (b) |
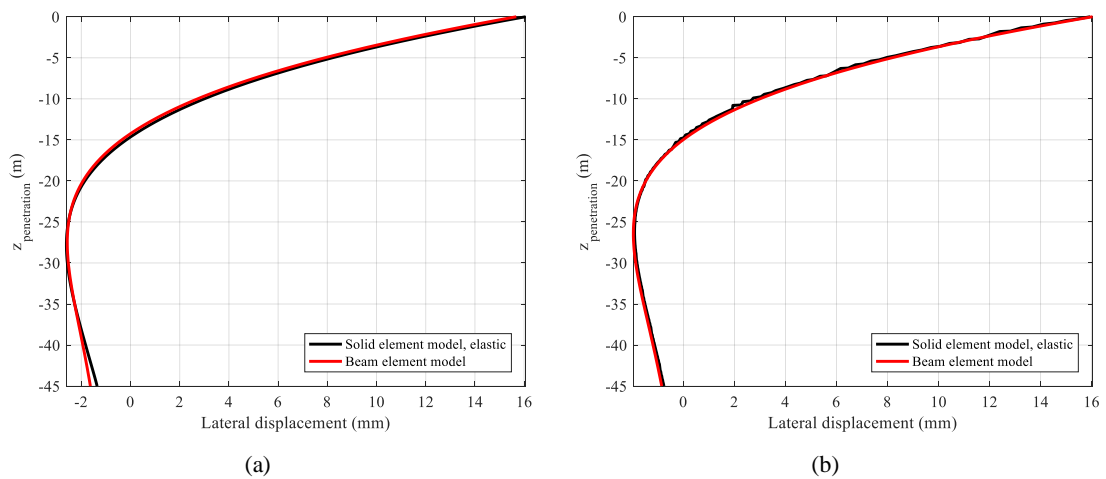
Figure 4-2. Pile deflections from the mudline to the bottom of the pile in the solid and beam element models (a) without the gravitational loads and (b) with the gravitational loads applied.

As can be seen, the mudline displacements show a good agreement between the solid and beam element models. The deflected shapes appear to be similar through the penetrated depth of the pile. It should be noted that in the solid element models application of gravity causes a slightly higher confinement with depth, as a result of compression in the soil, which is not accounted for in the beam element models. Accordingly, the stiffness of soil springs was increased by 20% for the bottom half of the penetration depth in the beam element models to get a match between the

two models. Figure 4-3 shows the longitudinal stresses along the penetrated depth of the pile in the considered scenarios.

(a)   (b)
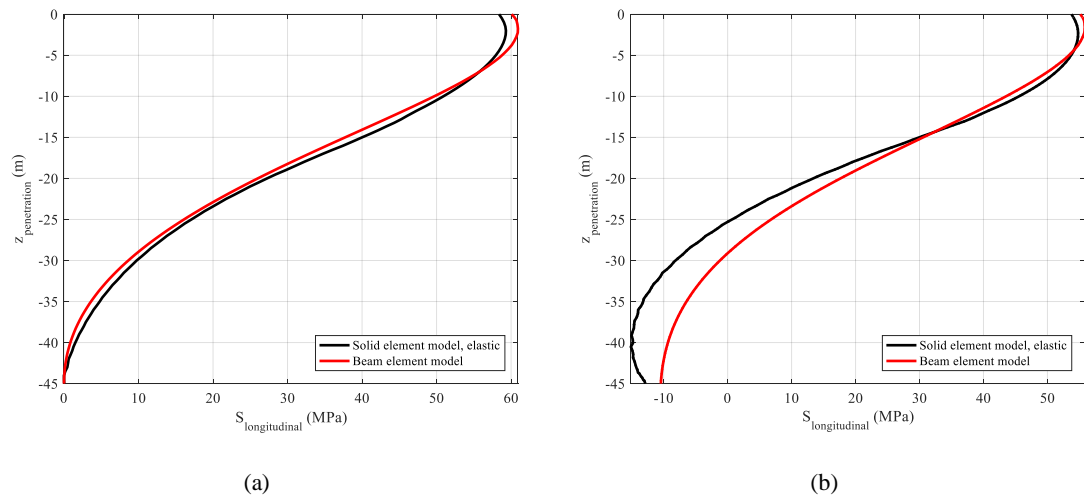
Figure 4-3. Longitudinal stress in the pile from the mudline to the bottom of the pile in the solid and beam element models (a) without the gravitational loads and (b) with the gravitational loads applied.

Figure 4-3(a) shows that when the gravitational loads are not applied, the beam and solid element models show a close distribution of the longitudinal stresses with a difference of 2.5% at the maximum stress. However, when gravity is applied, the results show a fairly different rate of change in the longitudinal stresses in the solid element model, which is thought to be due to the additional compressive loads caused by the friction shear stress at the interface with the soil. In order to show this, the longitudinal stress in the pile due to only the gravitational loads were studied. Figure 4-4 shows the longitudinal stress in the pile due to gravity only for different coefficients of friction (μ) (between 0.6 and 0.03).
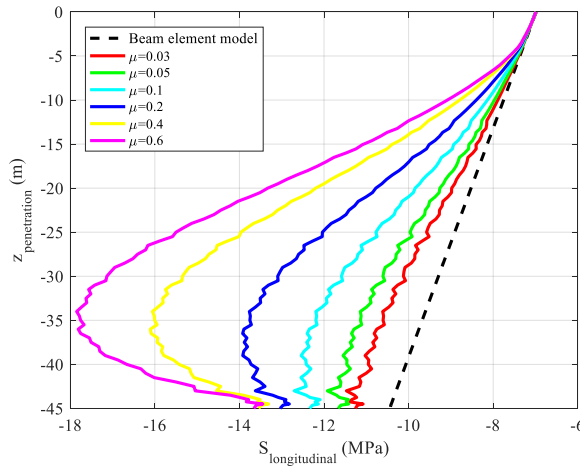
Figure 4-4. Comparison of the longitudinal stress below the mudline in the pile in the beam element model with the stresses in the solid element models due to the gravitational loads for various coefficients of friction.

As can be seen, the presence of friction in the model causes an additional compressive stress in the pile due to the interaction of the neighbouring soil with the pile. According to Figure 4-4, the reference coefficient of friction in the pile (i.e. μ =0.4) causes a maximum deviation of 53% compared to the beam element model. However, when μ=0.03 was applied, the stress in the solid element model was only higher by 6%. Also, as the coefficient of friction increases, the variation of stress in the pile becomes less linear, peaking at around z=-35m. This is due to the increased influence of the frictional stresses, which has a quadratic relationship with depth. The skin friction between the soil and pile is typically modelled using t-z curves, which were not considered in this research. Nevertheless, the difference in the maximum longitudinal stresses seems to be minor (i.e. by 1.5%) in Figure 4-3(b).

The identical deflected shapes and minor differences in the maximum longitudinal stresses in the beam and solid element models of the wind turbine verifies their finite element modelling. In the following sections, the influence of soil type (i.e. soil stiffness), number of springs in the beam element and soil cylinder size in the solid element models on the lateral response and modal properties of the wind turbine are discussed.

4.3   Static analysis

4.3.1   Beam element model (p-y curves)

Figure 4-5 shows the lateral deflection of the pile at the mudline for different numbers of lateral springs in the beam element model. A good match is found between the deflections predicted by fifteen and thirty springs. Comparison of the lateral deflections at mudline for other spring quantities shows that three springs model underestimates the lateral displacement of the monopile by an average of 12% compared to the fifteen and thirty springs. A good match is found between

the deflections of five and nine springs, which predict 8% lower lateral displacements at the mudline than thirty springs.
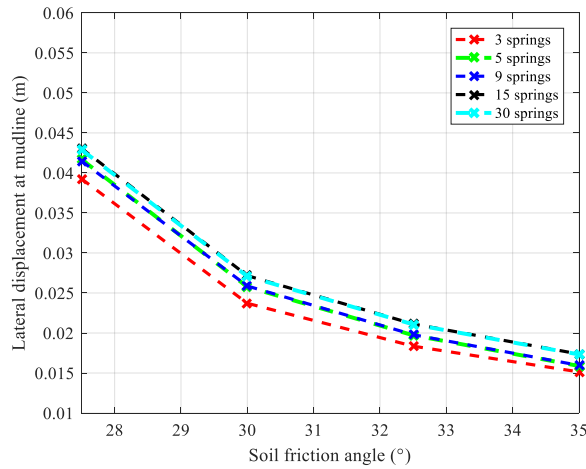
Figure 4-5. Lateral displacement of the pile measured at the mudline for different numbers of lateral springs in the beam element model.

Comparing the sensitivity of deflections to the soil type shows that in loose sand ($\varphi=27.5°$), the lateral displacement of the pile at the mudline is more than 1.5 times the medium dense sand-1 ($\varphi=30°$). Also, the lateral deflection for the dense sand ($\varphi=35°$) is less than half of the loose sand ($\varphi=27.5°$). According to Figure 4-5, the mudline lateral displacement shows a smaller decrease with increasing soil friction angles above $\varphi=30°$.

In a non-homogeneous profile, more springs may be necessary to capture the distribution of soil layers along the pile. In this research, the soil profile for fatigue analysis was discretised with thirty springs. This enabled a more accurate definition of different soil layers and allowed modelling the scour in more details.

4.3.2   Solid element model (elastic and Mohr-Coulomb)

Figures 4-6(a) and (b) show the lateral mudline displacements for various soil types predicted by the solid element models with elastic and Mohr-Coulomb materials, respectively. Soil block diameters $12D_{pile}$ and $18D_{pile}$ predict almost identical lateral displacements (particularly in the elastic soil). The smallest soil block ($3D_{pile}$) leads to an underestimation of the lateral displacements by up to 28%. However, $6D_{pile}$ soil block predicts closer lateral displacements to the larger blocks (up to 8% different). Comparison of Figures 4-6(a) and (b) indicates that there is a sign of soil plasticity, as the lateral displacements are higher by approximately 40% in the Mohr-Coulomb models compared to elastic soil. In the elastic material definition, the dense sand ($\varphi=35°$) displacement is 56% lower than that of loose sand ($\varphi=27.5°$). A similar difference between displacements in loose ($\varphi=27.5°$) and dense sand ($\varphi=35°$) was measured in the Mohr-Coulomb solid element models.
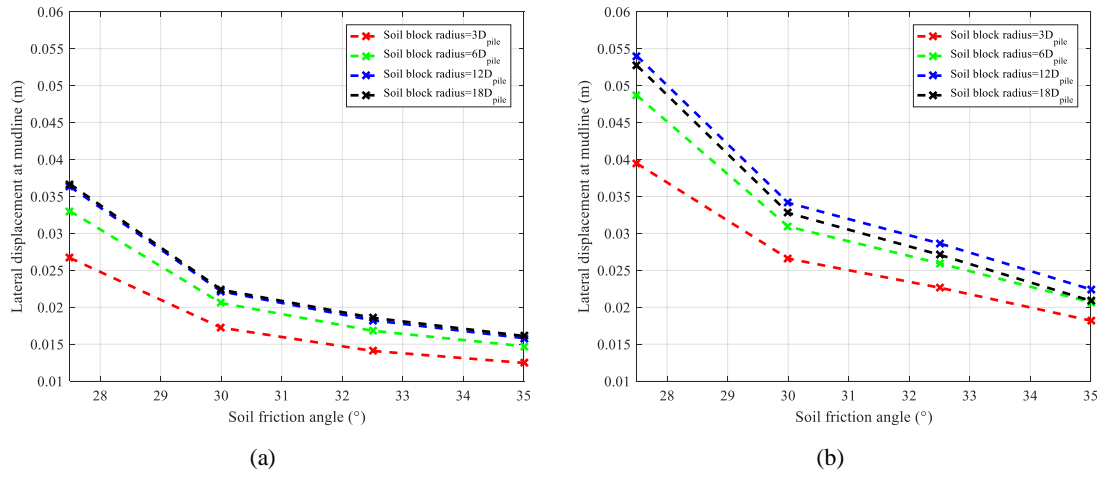
Figure 4-6. Lateral mudline displacements in the solid element models for various soil types and block diameters with (a) elastic soil material and (b) Mohr-Coulomb soil material.

4.3.2.1 *Boundary effects in the solid element models*

It has been demonstrated that soil cylinder size in the solid element models can have a significant influence on the lateral mudline displacements (especially for $3D_{pile}$). The effect of boundaries on the stress state in the soil is also a major factor, especially in dynamic analysis. Figure 4-7 shows the Von Mises stress in the soil for different block dimensions. Von Mises stress is typically used as an indication to assess the yielding of a material. As an example, in this figure, all soil blocks are assigned homogeneous medium dense sand-2 ($\varphi=32.5°$). It should be noted that the influence of boundaries could be slightly more significant in the softer soils due to their higher straining.
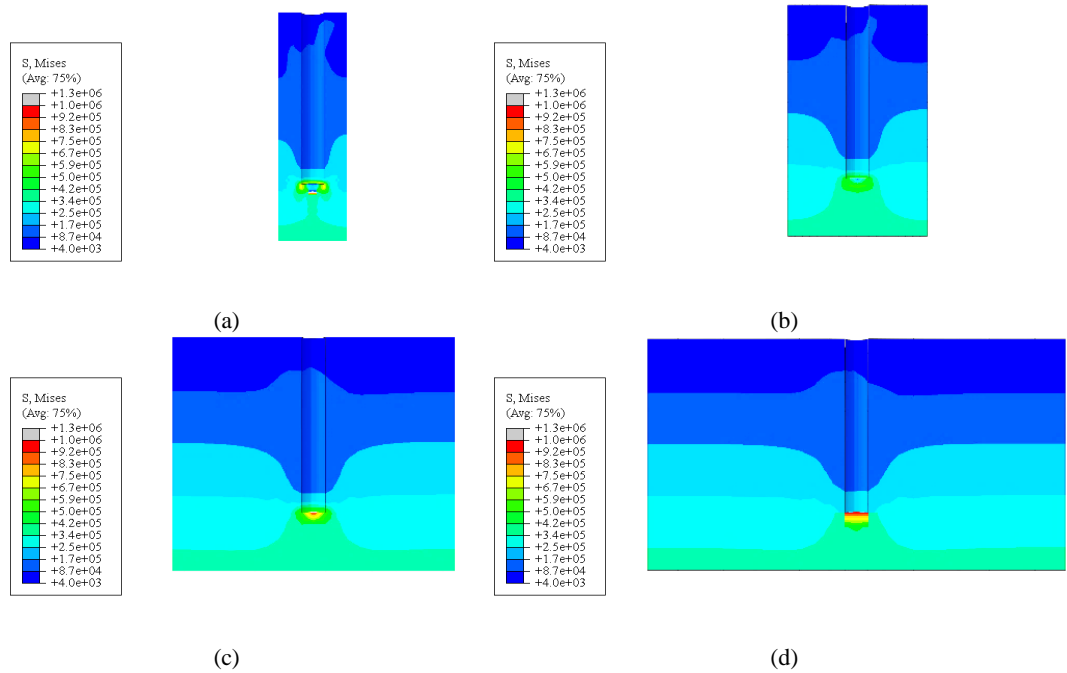
Figure 4-7. Von Mises stress in the soil blocks with medium dense sand-2 ($\varphi=32.5°$) and a diameter of (a) $3D_{pile}$, (b) $6D_{pile}$, (c) $12D_{pile}$, and (d) $18D_{pile}$.

The stress in the soil block can be classified into gravitational stresses and stresses that stem from the lateral loading of the wind turbine. The gravitational stresses show an increase with depth in the soil and are symmetrical about the medial axis of the soil block. Also, the weight of the wind turbine causes a stress concentration underneath the monopile, which propagates to deeper depths. The lateral loading leads to the disturbance of the symmetry in the stresses. In all figures, close to the top surface, the soil on the right side of the monopile is under compressive stress, while the soil on the left side of the monopile experiences tensile stresses. A similar scenario occurs at the bottom of the pile, but in a reversed order. Both of these areas can experience plastification in the Mohr-Coulomb material definition. The effect of soil boundaries on the stress layers in the soil, due to their proximity to the pile, can be seen in Figures 4-7(a) and (b). However, Figures 4-7(c) and (d) show that once the dimensions of the soil block increase beyond a certain level, the stress state of the soil is less affected by the side boundaries. Also, in these figures, the stresses from the weight of the wind turbine are precisely concentrated under the monopile and are less affected by the side and bottom boundaries. The influence of bottom boundary was not studied here, as its influence on the lateral behaviour of the monopile was significantly less pronounced. Instead, a recommended value of 15m clearance by Achmus and Abdel-Rahman (2005) was used as a minimum. Based on the observations made here, soil block diameter of $12D_{pile}$ and higher is considered to be a suitable choice for the analysis of wind turbines, which is in line with Achmus and Abdel-Rahman's (2005) recommendation.

4.3.3   Comparison of the beam and solid element models

Comparing Figure 4-5 and Figure 4-6 suggests that the mudline lateral displacements predicted by p-y curves are in better agreement (up to 15% difference) with the elastic material model than Mohr-Coulomb models. However, the deviation between the beam and solid element models with elastic soil reduces to approximately 8% for stiffer soil types. Also, the relative change of displacement for different soil types follows a closer trend in the elastic and p-y curve models compared to Mohr-Coulomb soil models. This indicates that p-y curves are relatively linear for the fatigue loads and the plastification of the soil, which occurs at the top and bottom (i.e. at the toe kick) of the soil-pile interface, is not properly captured in the p-y curves. This observation is in good agreement with the findings in the literature (Achmus and Abdel-Rahman, 2005; Achmus, Kuo and Abdel-Rahman, 2009; Byrne *et al.*, 2015). Figure 4-8 shows the lateral displacement and rotation of the wind turbine measured at the tower top in the beam and solid element models. The tower top displacements match in the elastic solid element and beam element models. However, the deviation of the tower top displacements and rotations in Mohr-Coulomb from the elastic soil models (and p-y curves) are smaller than the ones seen at the mudline. The tower top rotations and displacements vary by less than 5% in the dense sand ($\varphi=35°$).

(a)   (b)
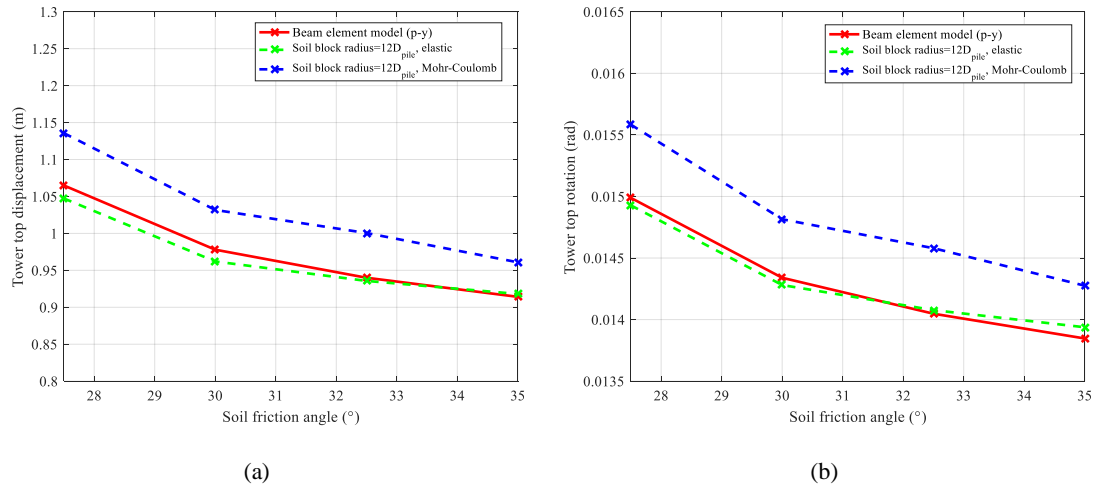
Figure 4-8. (a) Lateral displacement and (b) rotation of the wind turbine measured at the top of the tower.

The variation of the first natural frequency for different soils is important due to the narrow range of allowable frequencies in the design of offshore wind turbines (between 1P and 3P frequencies in the soft-stiff design). Figure 4-9 presents the first natural frequency of the wind turbine predicted by the beam and solid element models.
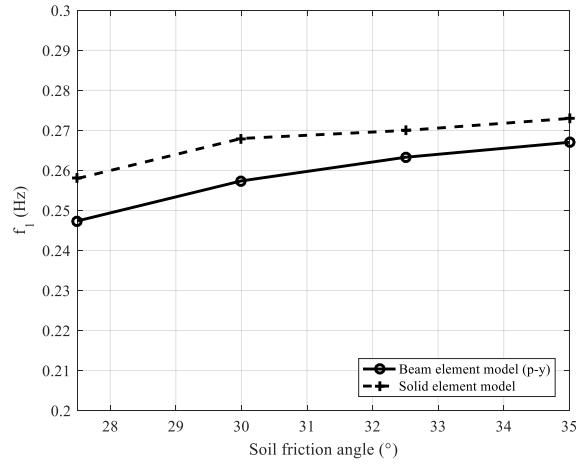
Figure 4-9. First natural frequency predictions by the beam element and solid element models of the wind turbine in various soil types.

The changes in the natural frequency of the wind turbine are dependent on the variations in the stiffness of the support structure. Figure 4-9 shows that the first natural frequency changes by approximately 8% from the loose to dense sand ($\varphi=27.5°$ to $\varphi=35°$) in the beam element models. It was shown in Figure 4-8 that the lateral and rotational stiffness of the wind turbine varies by less than 3% between the beam and elastic solid element models. Similarly, the predicted first natural frequencies in Figure 4-9 show an over-estimation of the first natural frequency by the less than 3% in the solid element model. For denser soils, the gap between the natural frequencies is smaller (approximately 2%).

Figure 4-10(a) shows the deflection of the pile, while Figure 4-10(b) shows the longitudinal stress in the pile along the penetration depth for dense sand ($\varphi=35°$), as an example. The longitudinal stress in the monopile was used for the fatigue analysis of the NREL 5MW offshore wind turbine in Chapter 6. The longitudinal stress in monopile is defined in Equation (4-1):

$$\sigma_{longitudinal} = \sigma_{bending} + \sigma_{gravitational},$$

(4-1)

where $\sigma_{bending}$ is tensile, or compressive stress resulted from the bending moment by the lateral loads and $\sigma_{gravitational}$ is the compressive stress caused by the gravitational effects. It was shown in section 4.2 that the frictional stresses cause an additional compressive load on the pile in the solid element models.

Figure 4-10(a) shows that in spite of the closer lateral displacements in the elastic and p-y curves models, a slight difference in the deflected shapes is seen. A higher toe kick is present in the solid element models as a result of plastification in the Mohr-Coulomb models and differences in the distribution of lateral soil resistance in the beam and solid element models. Figure 4-10(b) shows the differences in the distribution of stresses along the pile in the solid (elastic and Mohr-Coulomb) and beam element models. The maximum stresses in the pile are lower in the solid element models with elastic and Mohr-Coulomb material by 4.5% and 2%, respectively, compared to the beam element model.
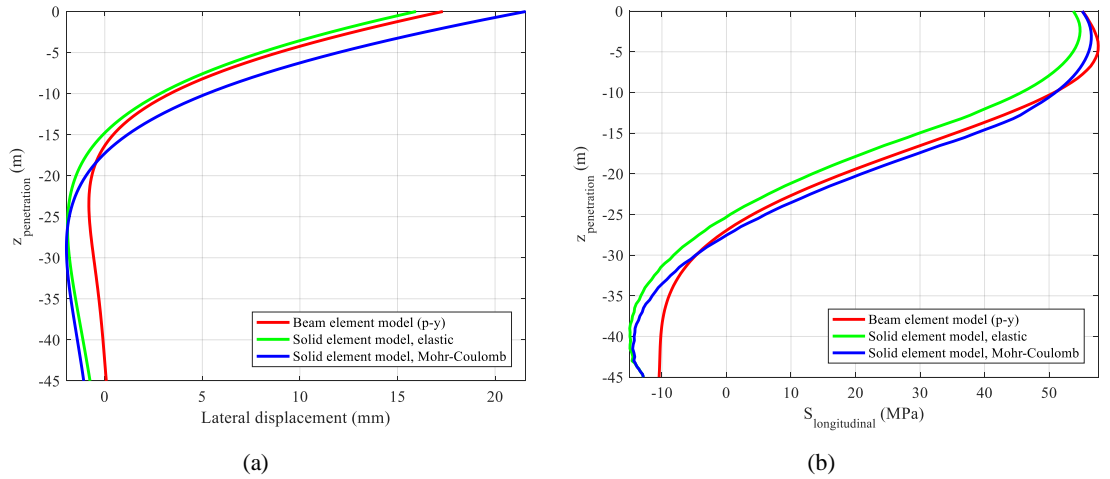
Figure 4-10. (a) Lateral displacement and (b) longitudinal stress along the penetration depth of the pile in the beam and solid element models.

In the beam element model, the stress is maximum at approximately 5m below mudline, while in the solid element models, the stress shows slightly different locations for the maximum longitudinal stress (i.e. around 3m and 4.5m in the elastic and Mohr-Coulomb models respectively). The influence of frictional stresses, which was caused in the finite element modelling process, can be the reason for this difference in the locations. Considering these

limitations, a fairly close match is found between the models and it can be concluded that in the current models, p-y curves could lead to slight overestimation of fatigue damages.

Up to this point, due to incomplete soil data, a uniform elastic modulus was applied throughout the soil cylinder. However, in reality soil elastic modulus is dependent on the stress level in the soil and is typically lower closer to the surface. P-y curves assume an increasing spring stiffness with depth. Using an alternative approach, the elastic modulus variation with depth was considered using Equation (4-2). According to EAU (1996), the elastic modulus variations in the soil is defined by the variations of the principal stress (σ) in the soil, and σ_{at} is the reference (atmospheric) stress, κ is the stiffness factor, and λ is the stiffness parameter, which vary depending on the soil type.

$$E_s = \kappa \sigma_{at} \left(\frac{\sigma}{\sigma_{at}}\right)^{\lambda} \tag{4-2}$$

The elastic modulus of the soil was calculated from the mudline to the bottom of the soil cylinder based on the stresses due to gravitational loads in the soil cylinder only. Application of lateral loads may increase the stress in some regions of the soil and can result in a slightly different elastic modulus. This effect was not considered here, however it could be implemented using UMAT (user-defined material) in ABAQUS. Figure 4-11 shows the elastic modulus variation through depth for dense sand ($\varphi=35°$), as an example.
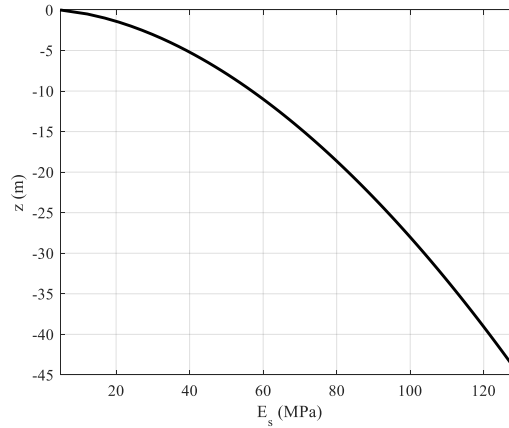
Figure 4-11. Variation of elastic modulus through depth for dense sand based on the stresses in the soil due to the gravitational loads.

The soil around the pile was discretised using six layers of equivalent elastic moduli, using the values given in Figure 4-11. Thus, the top two layers of the soil were assigned with smaller elastic moduli than specified in Table 4-3, while the deeper layers had a higher elastic modulus than $E_s=80$MPa, which was specified in the previous solid element models for the dense sand.

Figure 4-12(a) shows the comparison of the deflected shapes of the pile in the beam and solid element models with elastic and Mohr-Coulomb material models and variable elastic modulus. As can be seen, the higher stiffness of the bottom soil layers results in a closer pile deflections than the ones seen in Figure 4-10. In Figure 4-12(a), the higher mudline displacements from the ones shown in Figure 4-10 are resulted by the lower stiffness of the top soil layers than the previously applied E_s=80MPa in the solid element models.

Figure 4-12(b) shows the longitudinal stress in the pile along the penetrated depth. The maximum longitudinal stress in the beam element models with p-y curves shows a slightly closer match with the variable elastic modulus assignment in the solid element models (varies by 4%). The solid element model with Mohr-Coulomb material shows a lower deviation of the maximum stress by 1.5% compared to the beam element model (p-y curves). However, as it was also seen in Figure 4-3(b) and Figure 4-10(b), the compressive stresses at the bottom of the pile seem to be different in the solid element model from the beam element (p-y curves) model for the reasons previously mentioned. Overall, the variability of the soil stiffness through depth seems to result in slight changes in the maximum longitudinal stress in the pile.

(a)   (b)
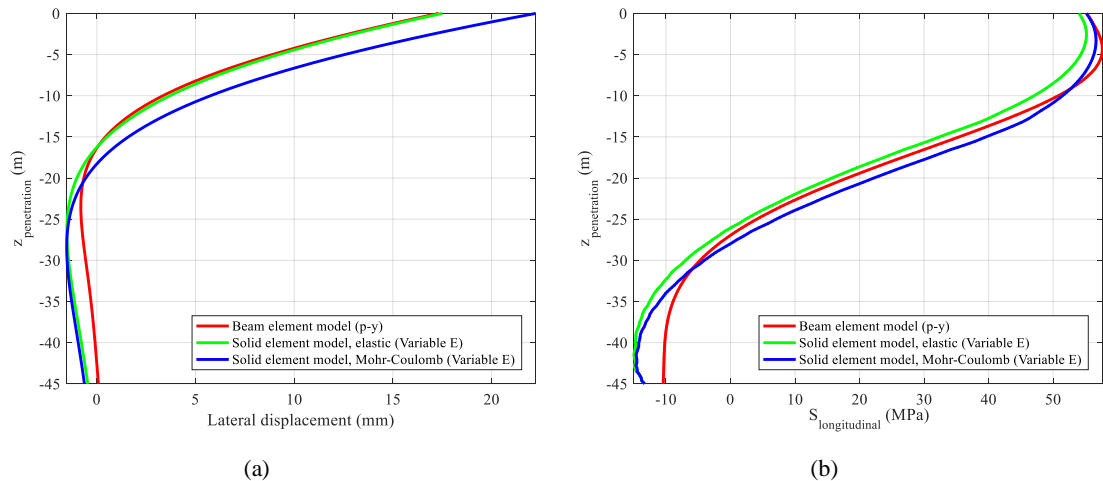
Figure 4-12. (a) Pile deflection and (b) longitudinal stress along the penetrated depth in the solid element models with variable elastic modulus and the beam element models.

Application of variable elastic modulus in the solid element models creates a more accurate model for the soil, but it does not show a significant advantage in obtaining a better match between the beam and solid element models. This is thought to trace back to the stresses induced by the contact in the solid element models, which are not included in the beam element models. Finite element modelling of the soil-structure interaction is a complex task and models that are more accurate are required for a detailed investigation of their interaction. However, as the main objective of this study was to verify the application of p-y curves in the beam element model using the more detailed solid element models, further consideration of soil-structure interaction was considered to be out of the scope of this research.

4.4   Summary

This chapter aimed to verify the finite element model used and study the soil-structure interaction influence on the stiffness of the wind turbine structure. In addition, the influence of finite element modelling techniques on the results was assessed. Two conventional methods of beam elements with p-y curves and elastic and Mohr-Coulomb plasticity solid elements with friction were considered.

In the beam element models, a good agreement was found between the fifteen and thirty springs models. However, in this research, thirty springs model was selected to model the non-homogenous soil profile and scour in the fatigue analysis. The solid element models showed a good agreement between $12D_{pile}$ and $18D_{pile}$ boundaries for the soil block.

In general, the beam element models tend to underestimate the mudline deflections of the wind turbine significantly compared to the Mohr-Coulomb solid element models, which is in line with the findings in the literature. In addition, a slight overestimation of soil stiffness at deeper soil was observed in the p-y curves compared to the solid element models. However, a close match was found in the lateral and rotational displacements of the beam and elastic solid element models of the wind turbine.

The natural frequency of the monopile showed an 8% change for different soil types. For an offshore wind turbine, this is a substantial increase, as it can affect the dynamic response of the system.

The beam element models showed a slightly higher maximum longitudinal stress in the pile, which can lead to conservative fatigue life estimates. The marginal differences are thought to arise from the modelling of the soil-pile interface and the uncertainties associated with soil in both models (e.g. selection of modulus of subgrade reaction, k, in beam element models, friction and the exact elastic moduli in 3D models). The extensive simulations required in the fatigue analysis does not allow the use of solid element models, due to their computational costs. Various research has been done to improve p-y curves for the offshore wind turbine applications. However, none has been applied extensively in practice. Thus, in this research, beam element models with the recommended p-y curves by DNV (2013) were used for the fatigue analysis of the NREL 5MW wind turbine.

5 Transition Piece

In this chapter, the effect of the transition piece on the stiffness of offshore wind turbine support structure is studied. The transition piece connects the tower and pile, and therefore is an important feature in the transfer of forces between the two. The interface between various steel parts of the transition piece have conventionally been grouted. In long-term, the cyclic loads on the transition piece can cause degradation of material strength and wearing of the grout surfaces in contact with the steel sections, which can affect the stiffness of the transition piece and that of the system as a whole. In this chapter, the static analysis of a 3D finite element model of the transition piece is used to study the influence of material strength variations and contact resistance changes, which can occur in long-term, on the stiffness of the transition piece. The influence of nonlinear material behaviour and tied contact applications in the finite element model of the transition piece was also investigated. The reference transition piece is illustrated in Figure 5-1. In addition, the sensitivity of the stress in the pile, the wind turbine stiffness and modal properties to variations in the transition piece flexibility was examined by studying an integrated model of the Opti-OWECS 3MW wind turbine including the soil block.

In section 5.1, a description of the finite element models used is given. This is followed by the discussion of the observed mechanism of the force transfer in the transition piece in section 5.2. Section 5.3 compares the static response of the transition piece using elastic and Concrete Damaged Plasticity (CDP) material models for the grout. Section 5.4 shows the results of the sensitivity analysis of the lateral and rotational stiffness of the transition piece to changes in the elastic modulus of the linear grout material. In both sections, the influence of contact variations is also discussed. Section 5.5 investigates the transition piece stiffness effects in the integrated model of the Opti-OWECS 3MW wind turbine. Concluding remarks are presented in section 5.6.
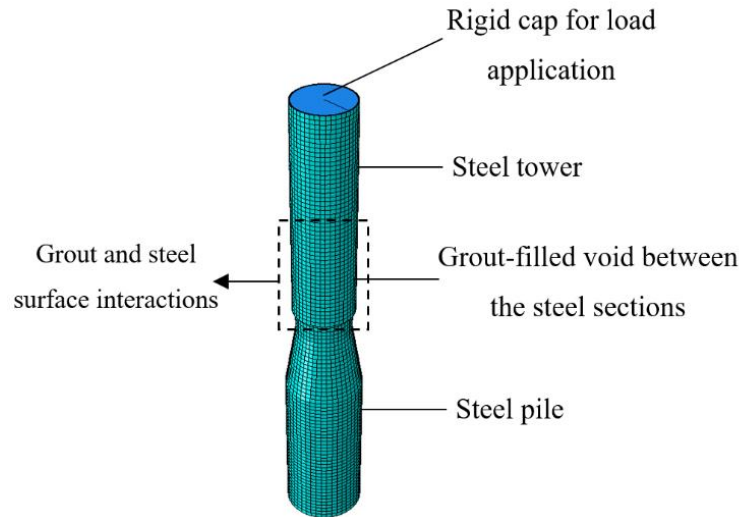
Figure 5-1. Overview of the transition piece model of Opti-OWECS 3MW wind turbine, showing different sections of the ABAQUS model and highlighting the area of the grout and steel interaction.

5.1 Modelling of the transition piece

The grouted connection model consists of steel tower and pile sections, and the grout that fills the void between the two surfaces. The transition piece considered in this study was not reinforced with shear keys. The pile and tower sections were extended beyond the grout in the models to avoid unwanted numerical stress singularities from boundaries close to the grout and steel interface. The dimensions of the transition piece parts are shown in Figure 5-2. All parts in the transition piece were modelled using three linear 8-node solid elements through their thickness with the circumferential length of 0.2m. Reduced integration element interpolation was used for the solid elements to speed up the calculations, the accuracy of which was primarily checked against full integration interpolation. A set of vertical, lateral and bending loads were applied at the top of the tower section, as shown in Figure 5-2. The vertical load corresponds to the sum of gravitational loads from the tower and nacelle masses. The lateral and bending loads were selected based on the level of aerodynamic loads in an operational wind turbine. In the static analysis, the results were taken for a lateral loading of 1MN with the corresponding bending moment for the lever arm of approximately 57m, extending from the tower head to the top of the transition piece. This type of loading is of a similar magnitude to the fatigue limit state maximum wind load, which is exerted on the rotor and is transferred to the transition piece from the tower.

The complete model of an Opti-OWECS 3MW wind turbine, consisting of a soil cylinder, tower section that extends from the nacelle to the transition piece, a pile that extends from 20m into the soil cylinder to the transition piece, and the grout that fills the void between these sections, was created to study the influence of transition piece flexibility on the stiffness of the offshore wind turbine. Detailed section dimensions were shown in Figure 3-2(a). The soil properties were defined by the parameters given in Table 3-4. In this model, the pile and tower sections were

modelled using a linear elastic steel material model with identical parameter values. The size of the elements in the steel and grout sections were similar to that used in the transition piece model (stated in the previous paragraph). The soil block has a radius of 30m and a depth of 45m and its elements vary in size from 2.5m to 0.5m. A lateral load of 1MN, similar to the transition piece model, was applied at the top of the tower (at the location of the nacelle).

Surface interactions and material behaviour are the important features to be implemented in this model. Here, all finite element models were modelled using either a tied contact or friction. Tying the surfaces effectively couples the degrees of freedom of the nodes at the interface of the grout and steel sections. Friction between the parallel surfaces was modelled using Coulomb friction model, and normal (i.e. perpendicular surfaces) contact was used for the interaction of the bottom surface of the pile with the soil block in the complete model of the wind turbine. The interface between the pile, tower and grout was modelled using contact elements with a coefficient of friction (μ) of 0.4, according to Pedersen and Jørgensen (2012). A rigid cap was tied to the top of tower section in the transition piece and the wind turbine models to distribute the loads evenly at the top surface. The bottom of the pile in the transition piece used fixed boundary conditions. The rigid cap is shown at the top of the transition piece model in Figure 5-1.
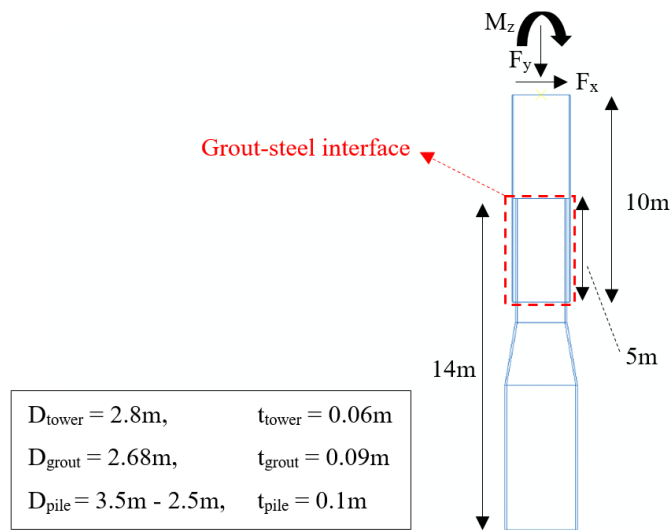
Figure 5-2. Transition piece dimensions of the reference Opti-OWECS 3MW wind turbine with the exerted loads at the top.

The grout (C150) material properties were defined according to the data given by Pedersen and Jørgensen (2012) along with steel material properties, as shown in Table 5-1, where ρ is material density, E is the elastic modulus, and υ is the Poisson ratio.

Table 5-1. Elastic material parameters for the grout (C150), based on the values suggested by Pedersen and Jørgensen (2012), and steel in ABAQUS.

Material	ρ (kg/m³)	E (GPa)	υ
Grout	2450	55	0.19
Steel	7850	210	0.3

5.2 Transition piece mechanism

The presence of friction between the grout and steel sections' interface is crucial to describe the bending resistance mechanism. In this section, a review of the mechanism of the transition piece is given from the static analysis of the model with elastic grout material and friction or tied contact between the interacting surfaces. The interface of the grout with the steel sections, as highlighted (red box) in Figure 5-2, is presented. A comparison is made between the Von Mises stress at the grout in the friction and tied interface models in Figure 5-3. Note that in these figures, the applied bending moment is in the clockwise direction, the lateral load is from left to right, and the gravitational load is downward (all applied at the top), as was also shown in Figure 5-2. Figure 5-3 shows that when friction is present in the model, the grout creates a force couple to resist the bending moment (i.e. the top left and bottom right corners in Figure 5-3(a)). However, in the tied case, the resistance appears to be distributed evenly from top to bottom on each side of the grout (i.e. left and right side of the grout in Figure 5-3(b)). Two points of stress concentrations are observed in the tied model (i.e. top left and right), which is the result of stress singularity at these contact points of the grout and steel sections. It was shown in Chapter 2 that this is not the actual case for the transition piece mechanism. The force couples in the friction contact model are resulted from the localised separation of the grout and monopile, which results in slippage and contact pressure points in the grout.

(a)   (b)
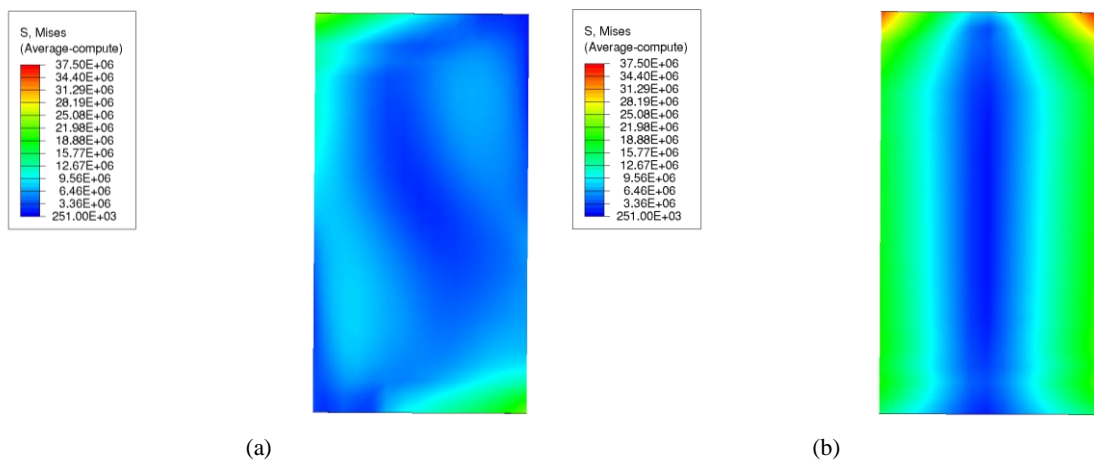
Figure 5-3. Von Mises stress (in Pa) shown on the outside grout surface (grout-tower interface) in the transition piece model with (a) friction contact and (b) tied contact.

Figure 5-4 shows the state of contact on the grout's interacting surfaces after the exertion of the loads on the transition piece. The presence of friction between the surfaces leads to the limited utilisation of the contact surfaces. The proportion of the surface of grout that is sticking to the monopile (i.e. has not separated from the monopile) is approximately 70% of the overall surface in contact. The internal and external surfaces of the grout, which are in contact with the pile and tower, respectively (i.e. Figure 5-4(a) and Figure 5-4(b)), show similar contact status patterns. Less than 10% of the surfaces demonstrate the occurrence of slippage.

(a)   (b)
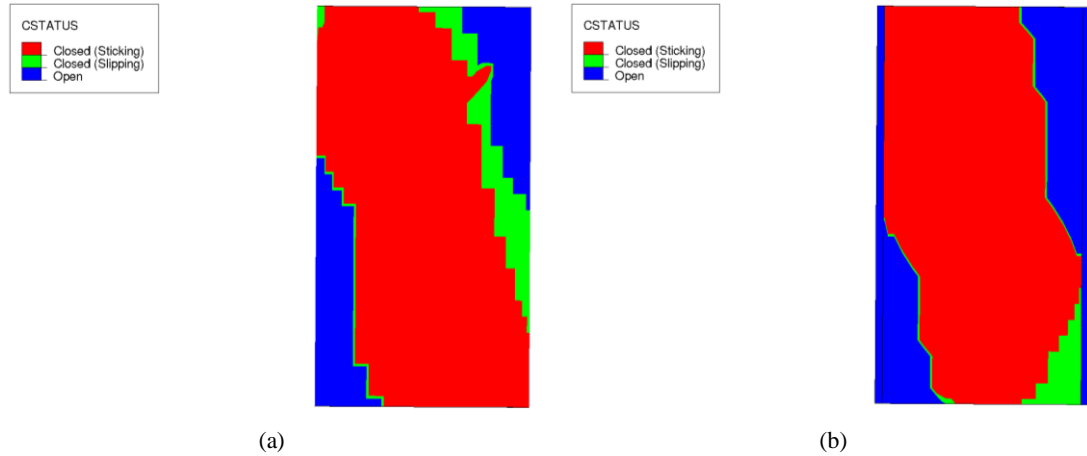
Figure 5-4. Contact status of the grout's surface on (a) the outside interface with the tower and (b) the inside interface with the monopile.

The influence of the element size on the contact status was investigated in a preliminary study and the element size was reduced (initially from 0.5m to 0.2m) until this influence was found to be negligible. Figure 5-5 shows the contact openings in the grout interface with the tower and pile sections. As expected, comparison of Figure 5-4 with Figure 5-5 indicates that slippage and sticking states occur at the locations where no contact opening happens. Also, Figure 5-5 shows that the maximum detachment occurs at opposite corners and on the opposite faces of the grout. The size of gaps appears to be equal and slightly higher than 2.6mm. The occurrence of separation between the surfaces of grout and monopile sections is a result of the ovalisation of the grout due to bending. The ovalisation was observed in the form of outward radial displacement of the grout within the regions highlighted in Figure 5-5. Prakhya, Zhang and Harding (2012) reported a smaller gap formation in an example grouted connection and loading. The gaps formed in this study are about two times higher than those in the transition piece considered by Prakhya, Zhang and Harding (2012). However, this could be due to the differences in the assumption of geometrical properties and loads.

(a)   (b)
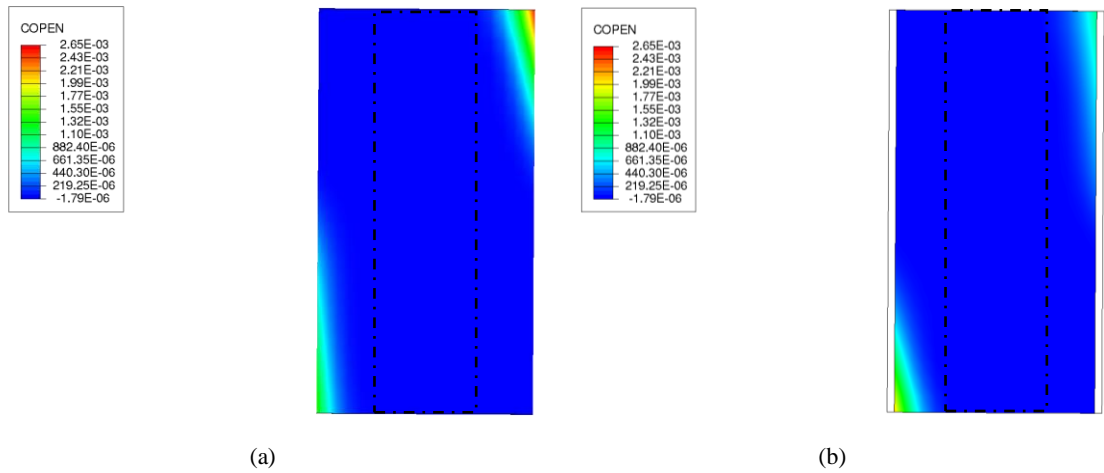
Figure 5-5. Contact opening shown on the grout's surface at (a) the outside interface with the tower and (b) the inside interface with the monopile. The highlighted regions correspond to the regions in grout with the radial displacements, which is an indication of ovalisation.

The presence of gaps on the opposite sides of the grout means that contact pressure areas are present on the opposite sides and corners of the grout. The resultant contact pressure areas on the grout are demonstrated in Figure 5-6. The pressure from the contact coincides with the closed contact areas shown in Figure 5-4. A limited fraction of the grout surface is mobilised through high-pressure zones, whose resultant force and moment provide the majority of resistance to bending and lateral loading.

(a)   (b)
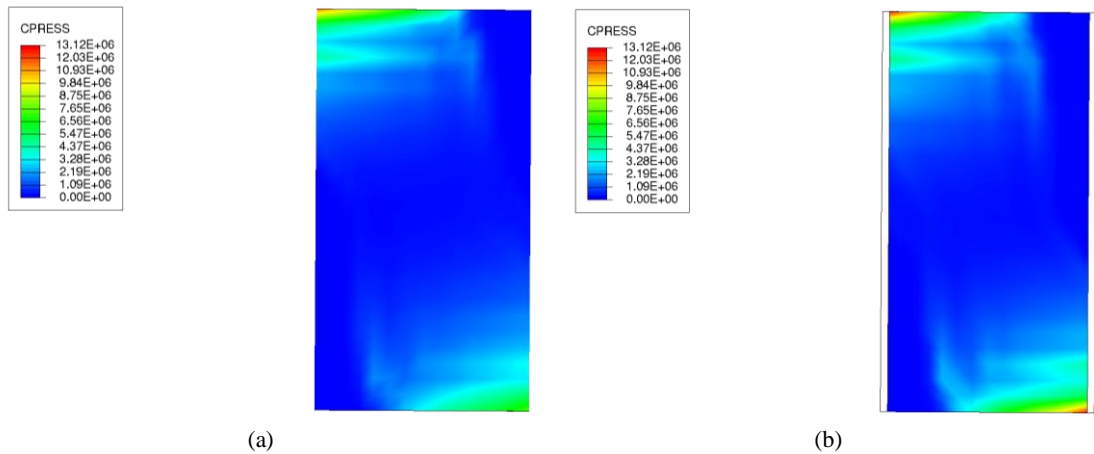
Figure 5-6. Contact pressure shown on the grout's surface at (a) the outside interface with the tower and (b) the inside interface with the monopile.

In the current unreinforced transition piece, the two main points of pressure are prone to crushing due to significant compressive stress, and the opposite corners are sensitive to cracking due to the tensile stresses and debonding from the lateral and bending loads. It was established in the literature (Chapter 2) that the presence of shear keys in the transition piece and the conical grouted connections limit the relative slip and opening between the grout and steel sections (Schaumann, Wilke and Lochte-Holtgreven, 2008; Lotsberg et al., 2012). However, these connections may experience higher stress concentrations, which makes them more susceptible to crushing.

5.3 Concrete Damaged Plasticity (CDP) material model

In this section, the Concrete Damaged Plasticity (CDP) model of the grout is used to investigate the effects of grout nonlinearities on the lateral and rotational stiffness of the transition piece. CDP material model for the grout have been widely used in the recent years. CDP uses a non-associative plastic flow rule which is similar to the Drucker-Prager approach (Dassault Systèmes Simulia Corp., 2012).

CDP model can capture the stiffness degradation in compression and tension under cyclic loads. This is done by assigning stiffness damage criteria for various inelastic strain levels. In addition, in a reversed cyclic loading scenario, the cracks, which were formed due to tension, are closed when the load is reversed (i.e. when this part of the section goes to compression). In this scenario, any damage in the model can be set to recover. Figure 5-7 shows the behaviour under stiffness degradation and recovery in a uniaxial loading case. For the definition of damage, d_t and d_c are the respective damage parameters under tensile and compressive stresses. w_t and w_c are the respective parameters for the damage recovery under tensile and compressive stresses.
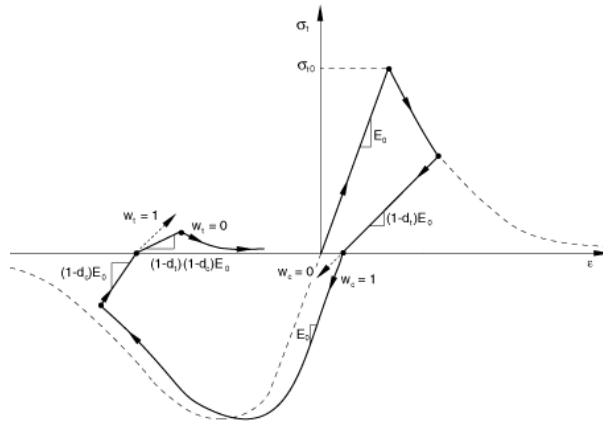
Figure 5-7. Example of CDP material definition with elastic modulus degradation and recovery in a uniaxial tension and compression case (Dassault Systèmes Simulia, 2012).

Table 5-2 shows the key parameters of the Concrete Damaged Plasticity model used to model the grout (C150) in this research, following values suggested by Pedersen and Jørgensen (2012) and Jankowiak and Łodygowski (2005). ψ' is the dilation angle, f_{b0}/f_{c0} is the ratio of initial equibiaxial compressive yield stress to initial uniaxial compressive yield stress, K is the ratio of the second stress invariant on the tensile meridian to that on the compressive meridian at initial yield and $\mathcal{C}$ is the eccentricity parameter, which are used to calculate the yield function (F) and potential flow (G) in the grout.

Table 5-2. Parameters used to define the nonlinear grout (C150) material from data presented by Pedersen and Jørgensen (2012).

ρ (kg/m3)	E_g (GPa)	υ	Ψ'	$\mathcal{C}$	K	f_{b0}/f_{c0}
2450	55	0.19	38	1.0	0.67	1.12

As shown in section 5.2, the stress distribution in the grout with tied contact does not agree with the expected pattern in practice. However, these models were also considered in the following studies, as they represent a similar configuration to what is going to be used in the fatigue analysis simulations (Chapters 6 and 7). Thus, the nonlinear grout material influence on the static response was examined using four scenarios with linear and nonlinear material definitions and tied and friction contacts in the transition piece model. Figure 5-8 shows the force-displacement relationship for these material and contact assumptions, in which the maximum displacements are magnified on the right. The behaviour of the transition piece is fairly linear in the tied and friction contacts. However, the inclusion of friction shows a more significant contribution to the stiffness of the transition piece compared to the elastic or plastic material properties of the grout. The tied model of the transition piece appears to have a higher lateral stiffness by 16%.
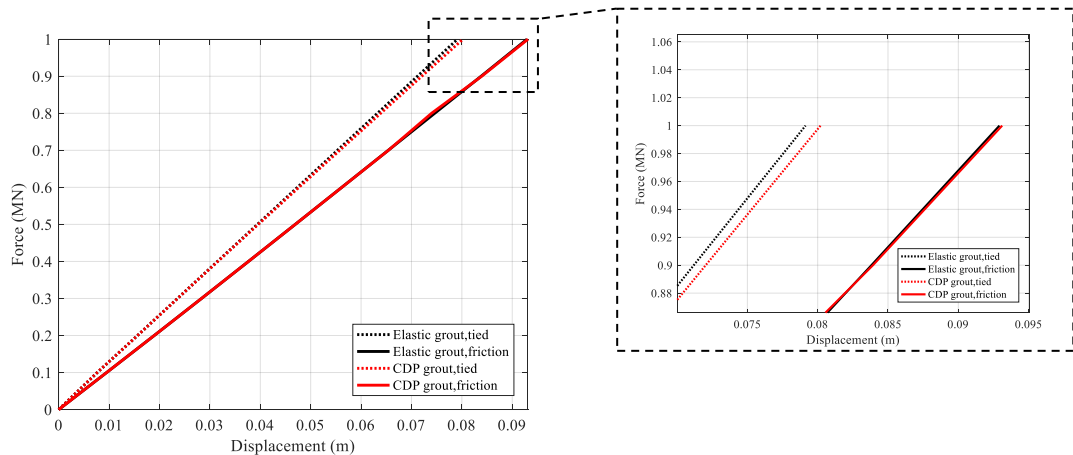
Figure 5-8. Force-displacement comparison between the elastic and Concrete Damaged Plasticity models of the grout with tied and friction contacts. The highlighted area is zoomed to the right.

According to Figure 5-8, in the tied models, displacements in the elastic grout models are approximately 2% smaller than those in the CDP grout models. This difference is almost zero in the models with friction contact. A further check showed that the difference in the displacements does not grow much for higher loads (up to 3MN), as a result of similar level of grout plasticity. These results further emphasise that the modelling of the contact between the grout and steel is a key in describing the transition piece's resistance to lateral and bending loads. However, the elastic material definition seems to be an appropriate choice for the finite element modelling of the grout, as the influence of material nonlinearity was found to be negligible on the stiffness of the transition piece under operational loads.

5.4 Transition piece stiffness study - Elastic grout

In this section, the change in the stiffness of the transition piece is investigated for a range of grout elastic moduli and coefficients of friction. Variation in the grout elastic modulus and friction are employed as proxies to examine the variations in the material strength and surface resistance, which, for instance, could arise from long-term damage. The lateral and rotational stiffness of the transition piece are calculated from the lateral displacements and rotations at the top of the transition piece. The grout is modelled as a linear elastic material. As before, the interfaces between grout, tower and pile are modelled using tie and friction contacts. The grout elastic modulus was taken as E_g=55GPa in the previous studies. In addition to this, two grout elastic moduli of E_g=5.5GPa and E_g=27.5GPa, which are $\frac{1}{10}$ and $\frac{1}{2}$ of the original value, and a higher value of E_g=110GPa were considered to investigate the influence of grout elastic modulus on the lateral and rotational stiffness of the transition piece. Figures 5-9(a) and (b) show the lateral and rotational stiffness changes in the transition piece, respectively, for the same magnitudes of lateral and bending loads as before.

As before, for all elastic moduli, the lateral and rotational stiffness is higher by 16% in the tied models. The rate of change of the lateral and rotational stiffness in both (i.e. tied and friction) models tends to be smaller for grout elastic moduli higher than 27.5GPa. When friction is applied, the lateral stiffness of the transition piece is 1% lower in the model with E_g=5.5GPa than E_g=110GPa. The rotational stiffness, however, shows a slightly higher decrease of approximately 2% for the comparison of the same elastic moduli. These variations tend to be significantly lower than those observed in the tied models, where the lateral and rotational stiffness were reduced by 4% and 5%, respectively, when comparing the E_g=5.5GPa and E_g=110GPa models. Slippage in the friction models of the transition piece effectively reduces the dependence of the transition piece's lateral and rotational stiffness on the elastic modulus of the grout.
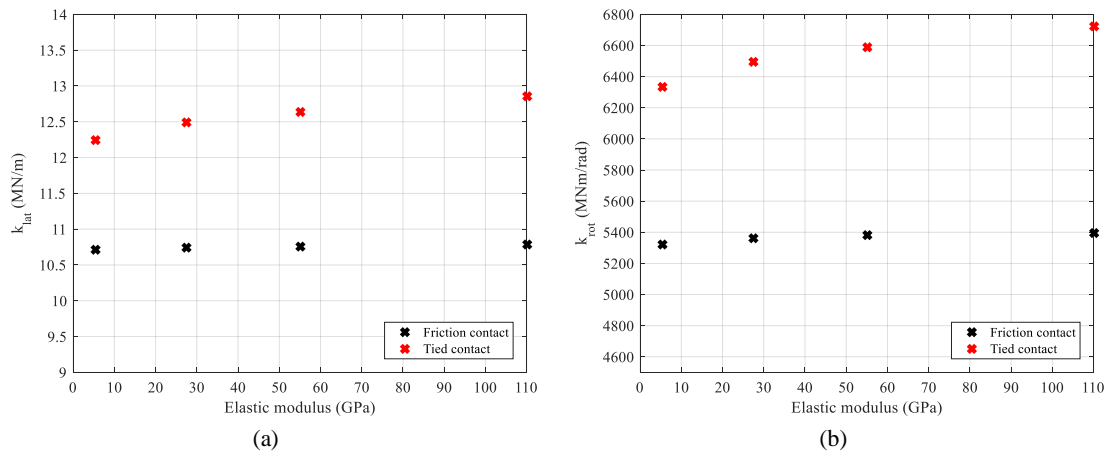
Figure 5-9. Variations of (a) the lateral stiffness and (b) the rotational stiffness of the transition piece with elastic grout material, and the tied and friction contact conditions for various grout elastic moduli.

The variations in the stiffness of the transition piece due to the changes in the coefficient of friction at the interface of the grout and steel have been investigated. Figure 5-10 compares the lateral and rotational stiffness of the transition piece for various values of friction coefficient (μ).
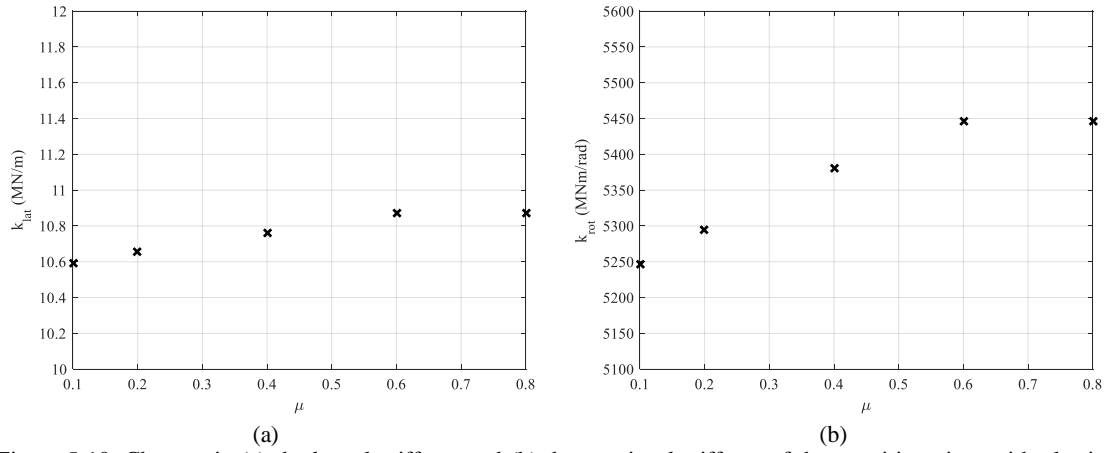
Figure 5-10. Changes in (a) the lateral stiffness and (b) the rotational stiffness of the transition piece with elastic grout material and friction contact conditions due to the variations in the coefficient of friction (μ).

The coefficient of friction (μ) was varied from 0.1 to 0.8 (the original value in the analysis was μ =0.4), while the grout elastic modulus was set to 55GPa. Similar to the results shown in Figure 5-9, the changes in the lateral and rotational stiffness of the transition piece due to the friction coefficient variations appear to be minimal. The lateral and rotational stiffness of the transition piece show a decrease of approximately 3% and 4% for an 88% reduction in coefficient of friction, respectively. In the literature, the coefficient of friction between the steel and grout is commonly suggested to be between 0.4 to 0.6. According to Figure 5-10, this range of friction coefficients causes less than 1% change in the stiffness of the transition piece.

5.5 Transition piece influence on the offshore wind turbine

To study the effects of the grout elastic modulus and transition piece contact on the stresses in the monopile, the wind turbine's static response and modal properties were calculated with the same variation in the grout elastic modulus as before. Figure 5-11 illustrates the assembly of the 3D solid element model of the wind turbine support structure, including the transition piece, and soil block/cylinder.
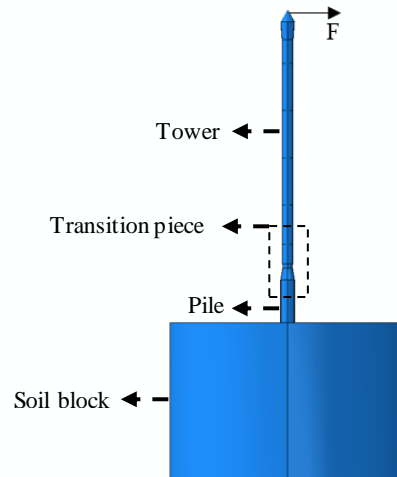
Figure 5-11. Assembly of the tower, monopile, transition piece and soil block/cylinder of Opti-OWECS 3MW wind turbine using solid elements with the application of the load at the tower-top.

Tower top displacements were approximately 11% lower in the tied contact models compared to friction models. The lateral and rotational stiffness of the wind turbine were calculated from the tower top displacements and rotations. The changes in the lateral and rotational stiffness of the wind turbine for each contact condition were smaller than the transition piece stiffness variations, shown in Figure 5-9. The lateral stiffness of the wind turbine decreased by approximately 1.3% in the tied model and 0.3% in the friction model, when the grout elastic modulus reduced by a factor of 10 (i.e. from 55GPa to 5.5GPa). The rotational stiffness of the wind turbine in both contact conditions experienced a 1% drop as a result of a similar decrease in the grout elastic modulus.

Figure 5-12 shows the variation of longitudinal stress in the monopile at the mudline level for different grout elastic moduli and contact properties. This location was selected as a representative point in the monopile and does not necessarily represent a hotspot or an extreme case. In both models, the grout elastic modulus seems to have a negligible influence on the stresses in monopile. It is shown that the longitudinal stress in the monopile with tied contact is approximatly 2% lower than the stresses for friction contact in the transition piece.
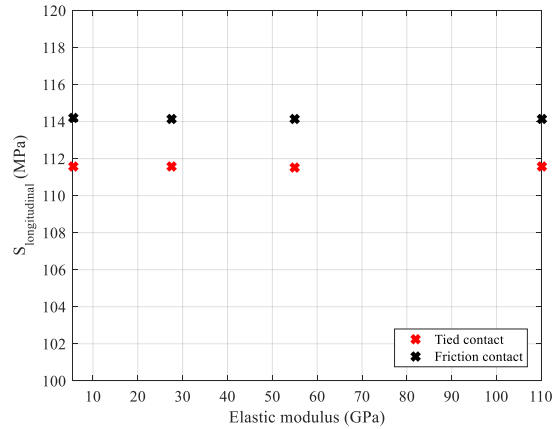
Figure 5-12. Longitudinal stress in monopile at the mudline for different transition piece contact conditions and grout elastic moduli.

Figure 5-13 shows the variation of the first natural frequency of the wind turbine to the changes in the elastic modulus of grout. The target first natural frequency for this wind turbine is 0.3Hz. The first natural frequency shows a change of less than 1% for the reduction of grout elastic modulus by a factor of 10 (from 55GPa to 5.5GPa). The drop of the grout elastic modulus from 110GPa to 5.5GPa (i.e. by a factor of 20) reduces the first natural frequency by approximately 1.5%.
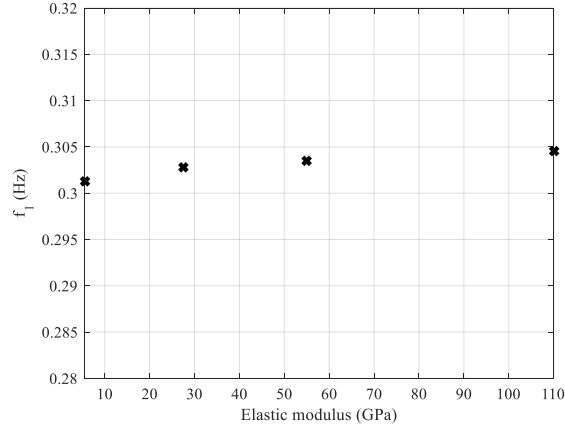
Figure 5-13. Variation of the first natural frequency of the Opti-OWECS 3MW wind turbine due to the changes in the grout elastic modulus.

The observations made here are in good agreement with the findings of Schaumann, Wilke and Lochte-Holtgreven (2008). However, the modal analysis simulations in this section were linear and Schaumann, Wilke and Lochte-Holtgreven (2008) suggested an analytical method to adjust the first natural frequency to account for the presence of friction damping in the model. Using their approach to consider the influence of friction, the first natural frequency of the offshore wind turbine was found to reduce by less than 1% from the values shown in Figure 5-13.

5.6   Summary

In this chapter, the influence of the transition piece material and contact properties on the stiffness of the wind turbine was studied. Solid element models of the transition piece, and tower, monopile, grout and soil assemblies were used. In this study, the transition piece was loaded by a 1MN lateral load at the top of the tower, the resulting bending moment, and the gravitational load from the mass of the tower and turbine on the top.

Including friction was found to be essential in describing accurately the mechanism by which the transition piece and stress-flow in the grout resist these loads. The transition piece demonstrated the formation of gaps at opposite corners, which separated the steel and grout sections by up to 2.6mm for the exerted loads. The ovalisation of the grout was also presented in the form of radial displacement of the grout. The concentration of contact pressures at opposition corners between the grout and pile and grout and tower was shown. The resultant bending moment due the pressure couples formed between the steel sections and grout contributes to the majority of resistance in the grout. Some shear resistance is also present due to the friction between the surfaces.

It was shown that the inclusion of material nonlinearities in the form of Concrete Damaged Plasticity does not have a significant influence on the static response of the connection. However, the presence of friction in the model makes the difference in the stiffness of the finite element model. A close match between the elastic and nonlinear material models of grout was obtained. Friction coefficient and elastic modulus variations also resulted in a minimal change in the lateral and rotational stiffness of the transition piece.

Finally, the assembly of the tower, monopile, transition piece and soil block was considered to study the contribution of grouted connections to the overall stiffness of the wind turbine. A negligible change was seen in the lateral and rotational stiffness of the wind turbine support structure, as a result of large variations in the elastic modulus of the grout. The maximum deviation in the lateral and rotational stiffness of the wind turbine was found to be up to 1.3%. The first natural frequency of the wind turbine also showed a similar shift, as a result of grout elastic modulus variations.

As mentioned, in a reinforced transition piece with shear keys, the relative sliding and gap opening between the grout and pile is reduced significantly. Generally, this type of transition piece can show a much closer offshore wind turbine stiffness and stresses in the pile between the tied and friction contact models. Despite the larger differences in the lateral displacements of the tower between the tied and friction models, the longitudinal stress in the monopile experienced minor changes. Based on this observation, the influence of using tied contact on the stresses in the pile is considered to be sufficiently small to be permissible in the fatigue analysis simulations. In addition, under cyclic action, the transition piece can induce some damping as a result of friction.

This was included as structural damping (in the form of Rayleigh damping) in the fatigue analysis simulations in the beam element models.

This decision does not indicate that the transition piece is not a crucial part of the wind turbine. It should be noted that when considering the serviceability limit state of the wind turbine (i.e. top deflections and rotations) or fatigue in the transition piece itself, consideration of contact properties would have a significant influence on the results. This research aims to focus on the vibration and fatigue analysis of offshore wind turbine structure in a global sense and the detailed study of the transition piece in the short and long terms is thought to be out of the scope of this research.

6 Damping Influence on Fatigue Life

As damping strongly influences the dynamic response of the system, which in turn drives its fatigue life, it is important to investigate systematically what range of fatigue life corresponds to the range of damping values commonly proposed (shown in Chapter 2). In this chapter, the influence of damping level, which could be from different sources (i.e. aerodynamic, soil, structural, or tuned-mass), on the fatigue life of the NREL 5MW wind turbine is studied using time-domain dynamic simulations of the beam element model with p-y curves. In addition, the effects of turbine operational state (shutdowns) on the fatigue of the structure is examined.

Section 6.1 gives an overview of the finite element model and the considered simulation scenarios. Statistical properties of the aerodynamic and hydrodynamic loads are presented in section 6.2. The influence of damping on the stress time history is presented in section 6.3. Section 6.4 presents the fatigue analysis results. The effects of the wind turbine operation, aerodynamic damping variability and different levels of damping in the operational wind turbine on the fatigue life of the offshore wind turbine are investigated. In section 6.5, an approximate approach to estimate the fatigue life for various damping levels are proposed, which does not require the computationally expensive time-domain simulations to assess the fatigue life for each level of damping. Finally, a summary of the results is given in section 6.6.

The results presented in sections 6.2, 6.3 and 6.4 have been submitted as a scientific paper to Ocean Engineering journal (Rezaei, Fromme and Duffour, 2017).

6.1 Finite element analysis details

The beam element model of the NREL 5MW wind turbine, as shown in Chapter 4, with the soil profile shown in Table 3-3 was used. Figure 6-1 illustrates the application of damping and loads in this finite element model.
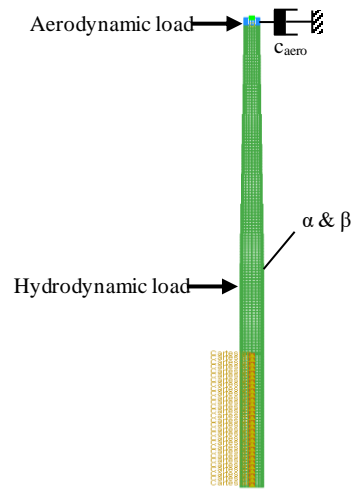
Figure 6-1. Sketch of the beam element model of the NREL 5MW wind turbine, showing the environmental loads and damping applications.

The operational regime of the wind turbine was studied for the configurations shown in Table 6-1. The rotor and blade pitch status in the operational regime were determined according to Table 3-5. In the operational wind turbine, a constant blade pitch angle was considered at each wind speed. The turbine was assumed to be parked in the non-operational regimes with either stalled or feathered blades. An extensive set of load cases for the fatigue design of offshore wind turbines has been recommended by DNV (2013). The applicability of non-operational scenarios to the fatigue of offshore wind turbines is limited and only attributed to specific design checks for the occurrence of faults. In this research, the non-operational (parked) scenarios are considered for the occurrence of faults representing scenarios where the turbine control system is faulty and the blades are stuck at certain positions (stalled or feathered). For simplicity and coherence with the fatigue analysis of the operational wind turbine, the non-operational scenarios were considered for the same environmental states as for the operational turbine, exemplifying hypothetical instances in which repair of the wind turbine are not possible for a prolonged period.

Table 6-1. Configuration of the wind turbine for various operational regimes.

Turbine regime	Rotor status	Blade pitch	$\zeta_{aerodynamic}$	ζ_{other}
Operational	Variable speed	Variable pitch	✓	✓
Non-operational	Stationary	Stalled	x	✓
	Stationary	Feathered	x	✓

No aerodynamic damping was assigned in the non-operational wind turbine models. The dashpot constant representing the aerodynamic damping was varied, while the Rayleigh parameters for damping from other sources (combined structural, hydrodynamic and soil damping) was kept constant, to give a different total damping in each operational turbine scenario. The levels of damping used are presented in the respective sections.

The dashpot constant for aerodynamic damping application was calculated according to Equation (6-1).

$$c_{aero,i} = 2M_{\omega_i}\omega_i\zeta_i,$$

(6-1)

where M_{ω_i} is the modal mass, ω_i is the natural frequency in rad/s, and ζ_i is the modal damping of the ith mode. In each model, the Rayleigh damping parameters (i.e. α and β) for the damping from the other sources (combined structural, hydrodynamic and soil damping) were determined by Equation (6-2). Both Rayleigh damping parameters were applied to the finite element model. The modal damping at the second mode was considered to be equal to 2% for the calculation of α and β.

$$\zeta_i = \frac{\alpha}{2\omega_i} + \frac{\beta\omega_i}{2}.$$

(6-2)

Application of damping in both forms were verified using a free vibration analysis of the wind turbine, in which the applied damping in the model was checked from the vibration decay of the wind turbine.

6.2 Influence of operational regime on loads and bending moment

The operational regime of the wind turbine determines the aerodynamic forces and damping on the structure. Figure 6-2(a) shows the mean resultant wave loads and their standard deviation for the sea states considered (Table 3-7). The mean and standard deviation of the aerodynamic and hydrodynamic loads were used to quantify their static and dynamic (varying) components. With increasing wave height and period, the static component of the wave load increases only slightly, whereas the dynamic component increases significantly. Figures 6-2(b) and (c) show the mean and standard deviation of the operational and non-operational wind loads for each environmental state. As one would expect, the aerodynamic load is significantly higher when the blades are pitched out (stalled) than when they are feathered. As the 'intensity' of the environmental states increases, so do the mean and standard deviation of the rotor thrusts. When the wind turbine is in operation, the mean wind load peaks at the rated wind speed and then decreases (as blades are increasingly feathered), whereas the standard deviation of the load shows a continuous increase with the wind speed due to turbulence. The mean rotor thrust for the operational wind turbine is higher than for the non-operational feathered wind turbine, but in the case of pitched out blades, the mean wind thrust for very high wind speeds (environmental states 22 and 24) is greater than during operation, where blades are increasingly pitched. The interaction of the wind with feathered or pitched out (stalled) blades and a stationary rotor decreases the standard deviation of the wind load, meaning that a significantly lower load turbulence is present for the non-

operational wind turbine compared to that experienced by the pitch-controlled operational wind turbine as the rotor is stationary.
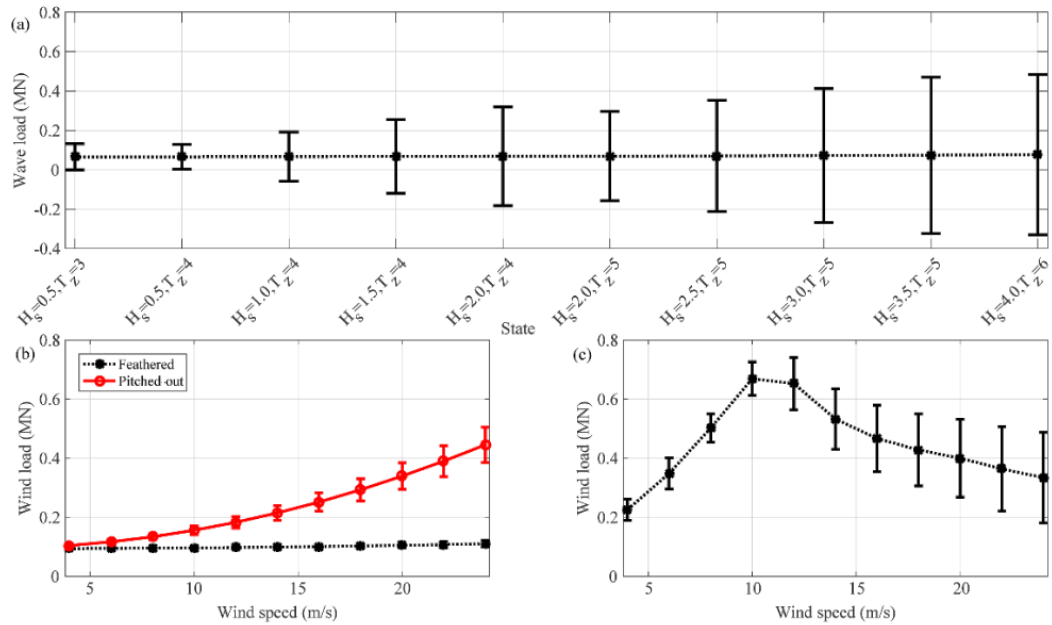
Figure 6-2. Mean (static component) and standard deviation (variable component) of the environmental loads: (a) wave load, (b) non-operational wind load (feathered and pitched out) and (c) operational wind load.

As a wind turbine is a type of cantilevered structure, the highest bending moment and stresses occur close to the bottom, with a significantly higher lever arm and thus bending moment contribution of the wind load. Figure 6-3(a) shows the mean and standard deviation of the mudline bending moment for the non-operational wind turbine, calculated from the combined wind and wave forces. When the blades are feathered, the wind load is approximately constant and the mean and standard deviation of the mudline bending moment is mainly driven by the increase in the variable component of the hydrodynamic loads. However, when the blades are pitched out, the higher lever arm of the wind thrust leads to an increasing mean mudline bending moment. The standard deviation of the bending moment at the mudline increases as both wind and wave loads have increasing dynamic components. Figure 6-3(b) shows the mean and standard deviation of the mudline bending moment for the operational wind turbine. The mean value peaks at the environmental states corresponding to the rated wind speed and then slowly decreases, roughly following the wind speed pattern shown in Figure 6-2(c). It is important to note that the relative contributions of the wind and wave loads are subject to the environmental conditions and water depth. The magnitude and lever arm of the hydrodynamic loads increases with the water depth, leading to a more pronounced influence of wave loading on the stresses below mudline.
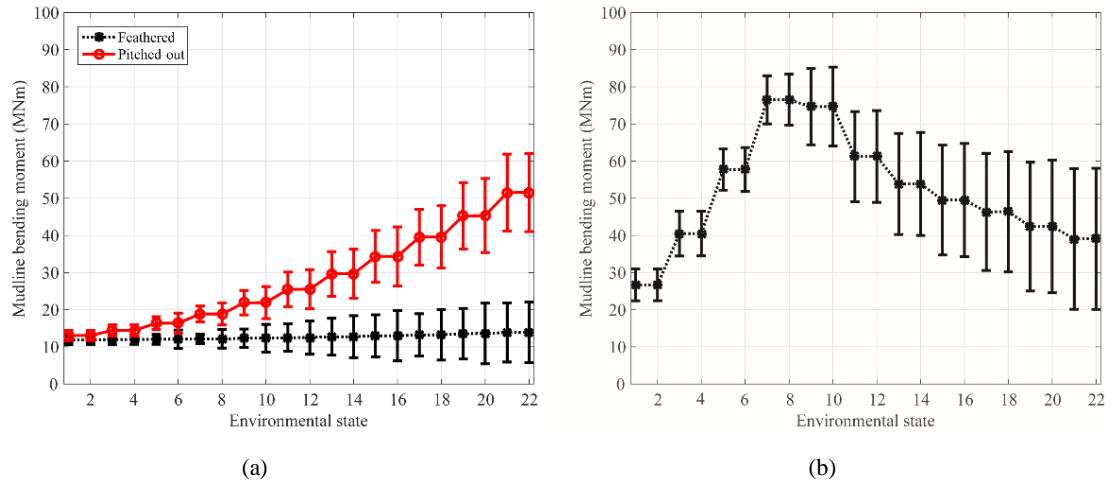
Figure 6-3. Mean (static component) and standard deviation (dynamic component) of the resultant loads, mudline bending moment for (a) non-operational wind turbine and (b) operational wind turbine at mudline.

As described in Chapter 3, wind and waves were considered to be unidirectional and in the fore-aft direction of the wind turbine. Therefore, the location of maximum tensile stress around the circumference of the pile is approximately at 180˚ on the upwind side of the monopile, as demonstrated by Fontana et al. (2015). As was shown in Chapter 4, the location of the maximum longitudinal stress in the monopile is not necessarily at the mudline and its precise location was investigated to accurately capture the highest stress for the fatigue analysis of the wind turbine. Figure 6-4 shows the variation of the bending moment along the depth of the monopile as a result of respectively 1MN wind and wave loads. For the soil conditions considered, the maximum bending moment in the reference monopile occurs approximately 8m below the mudline. Assuming the maximum stress occurs at the mudline instead of its actual location could result in an error of approximately 15% in the stress amplitudes in the monopile, significantly underestimating fatigue damage. It should be noted that the location of this maximum stress is specific to the geometry considered here and could shift depending on the soil properties and scour depth.
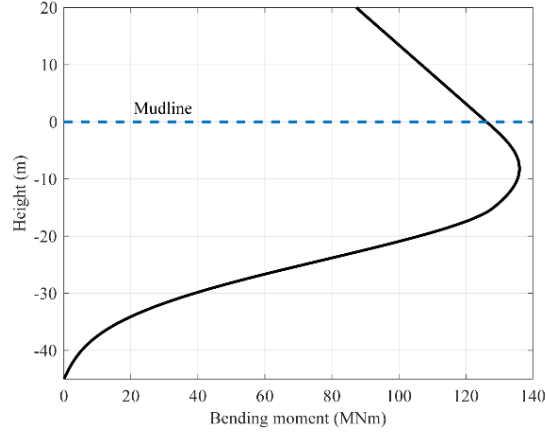
Figure 6-4. Bending moment in the reference monopile for 1MN wind and wave loads.

6.3   Damping effects on the stress

The stress reduction as a result of various levels of damping at the first mode on the standard deviation of the longitudinal stress at 8m below the seabed is shown in Figure 6-5(a). The standard deviation of the stress shows a higher reduction in the above rated wind speed environmental states (environmental states 11 and higher) than in the lower states. As the environmental conditions become more severe, the standard deviation of stress grows. As an example, a segment of the stress time history for environmental state 11, in which the wind speed is just above the rated wind speed of the turbine, is shown in Figure 6-5(b) to illustrate these reductions.

(a)   (b)
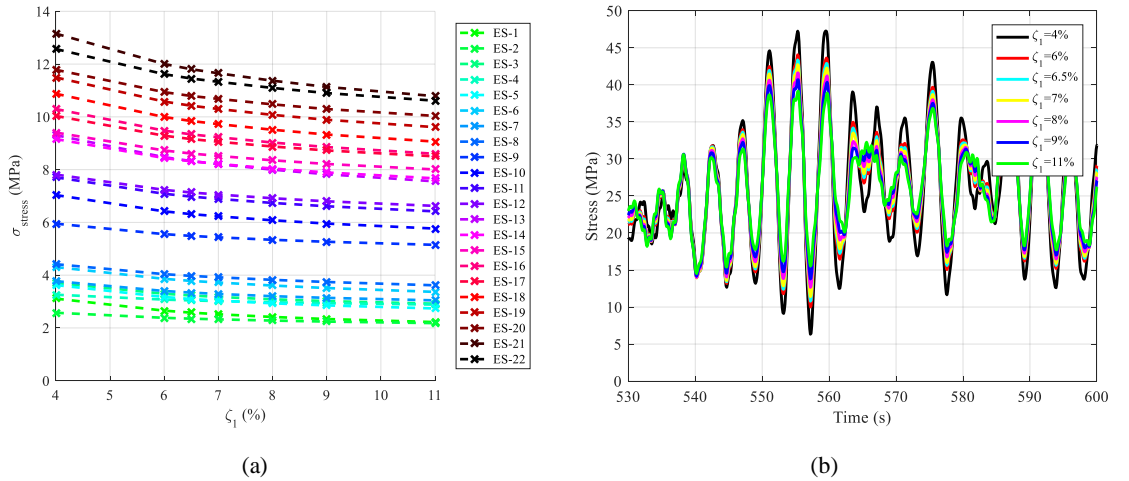
Figure 6-5. Changes in (a) the standard deviation of stress as a result of different damping levels for different environmental states and (b) the longitudinal stress in the monopile for environmental state 11 for different damping levels.

The stress response in the monopile consists of low and high amplitude cycles, which are present in the time-history of the stress response for all environmental states due to wind and wave loads. Comparison of the stress amplitudes shows a reduction of approximately 18% for an increase of 7% in the overall damping of the system (from 4% overall damping to 11% damping). The

reduction of stress in the monopile as a result of damping ranges between 7% to 13% for an increase of 2% and 5% in the overall damping, respectively. These reductions are similar to the reductions in the standard deviations of stresses shown in Figure 6-5(a). However, they are higher than those reported by Fontana et al. (2015) in the operational range of the wind turbine (the monopile was fixed in their model and value of the aerodynamic damping were not stated).

6.4 Fatigue analysis results

6.4.1 Effects of variable damping application

In this section, the effect of the variation of damping with wind speed is investigated by comparing the fatigue life of the offshore wind turbine when damping is assumed variable or constant. Variable aerodynamic damping values were taken from Valamanesh and Myers (2014) and used for illustrative purposes only, as they are based on a smaller wind turbine. According to Valamanesh and Myers (2014), aerodynamic damping of the wind turbine varies between 3.7% to 5.4% depending on the wind speed (Table 6-2), with the maximum value close to the rated operational wind speeds of their turbine. The average value of damping of approximately 4.5% was used as a reference for comparison.

Table 6-2. Aerodynamic damping ratio contributions at different wind speeds, based on data from Valamanesh and Myers (2014).

Wind speed (m/s)	4	6	8	10	12	14	16	18	20	22	24
Aerodynamic damping (%)	4	4	3.7	4.4	4.6	5.4	5.3	4.9	4.7	4.5	4.3

Figure 6-6 shows the environmental state normalised damage contributions for the constant and variable damping application models. The normalised damage contributions are obtained by factoring in the probability of occurrence of each environmental state to its damage. In this section, a general comparison is made between the respective damage contribution of each environmental state and a more detailed discussion of the environmental states' damages and their contributions is given in the following sections. Figure 6-6 shows that environmental states 11 to 18 (with the exception of environmental state 17) have the highest contributions to the fatigue of the wind turbine structure.

For environmental states 9 to 18, higher variable aerodynamic damping values were applied, according to Table 6-2. For some environmental states (e.g. 11-14), a reduction of up to 16% in the normalised fatigue damage contribution occurs due the higher damping values. However, for other environmental states (e.g. 15-18), the only slight increase in damping combined with a low probability of occurrence (Table 3-7) leads to only a small drop in their damage contribution.
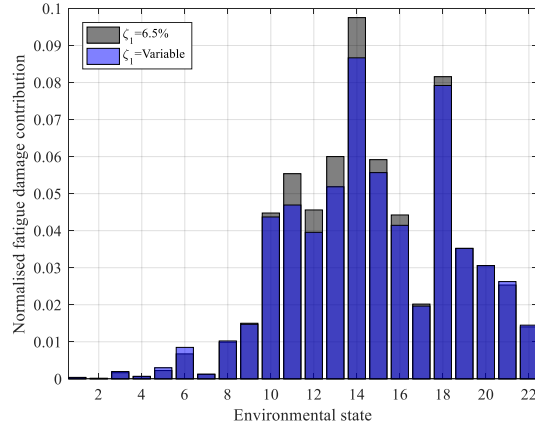
Figure 6-6. Normalised fatigue damage contribution changes as a result of the variable damping application. Bars are overlaid (i.e. all start from zero).

Overall, due to the variability of the aerodynamic damping and the probability of occurrence of the environmental states, the change in the damage contributions is variable, but the damage is only significantly reduced for the environmental states above the rated wind speed of the turbine. The fatigue life is calculated as 31 years for the constant damping case and 33 years for the variable damping case - a 7% increase in the predicted fatigue life of the system. Given that the values of varying aerodynamic damping are difficult to obtain and come with significant uncertainty, this rather small difference in fatigue life suggests that in practice assuming a constant aerodynamic damping for all wind speeds leads to acceptable fatigue life estimates. Therefore, a constant aerodynamic damping is assumed in the remainder of this chapter.

6.4.2 Operational vs. non-operational wind turbine

Although the environmental loads considered are in the operational range of the wind turbine, this section investigates the long-term effects on the fatigue life of wind turbine shutdowns. As they cause both a decrease in load and in damping, their overall effect is difficult to assess without a complete fatigue life calculation. Salzmann and Tempel (2005) suggested approximately 5% of aerodynamic damping for the operational wind turbine of a similar size, and as detailed in the literature review, damping from other sources is reported to be 1-2%. Therefore, reference damping of 2% for the non-operational and 7% for the operational wind turbine was assumed in this section, which is slightly higher than the constant damping considered in the previous section.
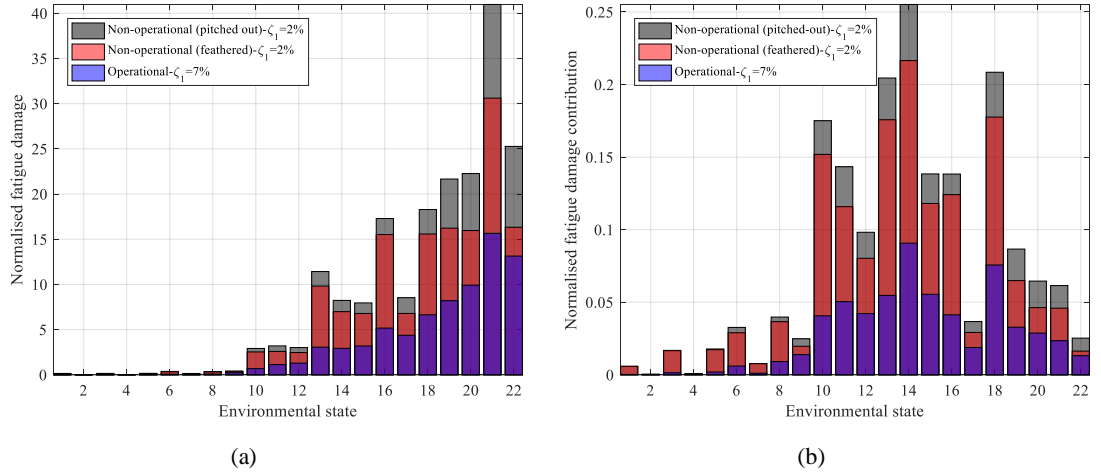
Figure 6-7. (a) Normalised damage and (b) normalised fatigue damage contribution of the environmental states for operational and non-operational (feathered and pitched out) wind turbines. Bars are overlaid (i.e. all start from zero).

Figure 6-7(a) shows the normalised damage for each environmental state of the wind turbine, comparing the operational turbine with non-operational (feathered and pitched out) loads and damping. The environmental loads and resulting bending moments for the operational and non-operational wind turbine can be seen in Figure 6-2 and Figure 6-3. Figure 6-7(b) shows the contribution of the environmental states to the fatigue damage of the wind turbine, taking the probability of occurrence of each state (Table 3-7) into account. Figure 6-7(a) shows that the fatigue damage increases in general with increasing wind speed and wave height, with slight variations due to the dynamic amplification from the forcing frequencies. The lower environmental states (up to #8) do not lead to significant fatigue damage. The environmental states that are above the rated wind speed of the operational wind turbine lead to a significantly higher fatigue damage. This confirms that the wind load has a high contribution to the fatigue damage of operational systems. In non-operational mode, the dynamic wave load dominates the fatigue damage. Feathered blades lead to lower damage than pitched out blades due to the lower aerodynamic load component. Figure 6-7(a) shows that in spite of the lower aerodynamic loads in the non-operational cases, the fatigue damage is significantly higher due to the absence of aerodynamic damping.

Figure 6-7(b) shows that fatigue life is dominated by the contribution of the environmental states around the rated wind speed. The predicted fatigue life of the operational wind turbine is approximately 33 years, as opposed to 11 years for the pitched out and 14 years for the feathered non-operational cases. The importance of the aerodynamic damping is clearly demonstrated by the fact that the higher operational damping compensates for the higher rotor loads and results in a fatigue life that is more than twice the fatigue life of the non-operational case. Environmental states are paired up such that odd-numbered states have the same wind speed as the following even-numbered state, so damage variation within each pair can be attributed only to different

wave loading. For instance, in Figure 6-7(a), environmental states 21 and 22 have the same wind speed of 24m/s but different wave loads (Table 3-7). The difference in the fatigue damages of these environmental states are approximately 40% for the non-operational wind turbine, but considerably lower for the operational case. These large variations, due to the differences in wave loading, are a feature for above-rated wind speed environmental states (see also environmental states 15-16 and 17-18) and can be explained by a combination of the higher magnitude of wave loads and the proximity of the wave peak frequency to the first natural frequency of the wind turbine. In the following section, the importance of damping for the fatigue life of the wind turbine in operation is investigated further.

6.4.3 Damping influence in operation

6.4.3.1 Fatigue damage comparison

In this section, a set of damping levels is considered to examine their effect on the fatigue damage in the wind turbine. The levels of damping applied to the operational wind turbine model range from 4% to 11%, 2% of which is applied in the form of Rayleigh damping to account for structural, hydrodynamic and soil damping. As shown in Figure 6-5(a), the standard deviation of the longitudinal stress (at approximately 8m below the seabed) shows a reduction of approximately 7%, 13%, and 18% for an increase of 2%, 5%, and 7% in the overall damping of the system.
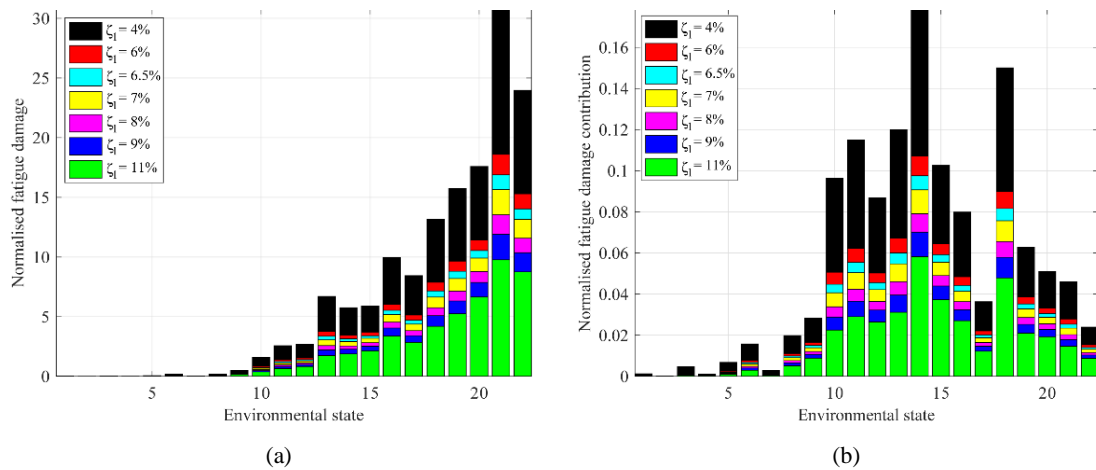
Figure 6-8. (a) Fatigue damage and (b) fatigue damage contribution for every enviromental state at different levels of total damping. Bars are overlaid (i.e. all start from zero).

Figure 6-8(a) shows the normalised fatigue damage and Figure 6-8(b) shows the contribution of the normalised damage for every environmental state at various damping levels while the turbine is in operation. As expected, the fatigue damage observed with 4% overall damping is the highest. Higher damping levels lead to a reduction in fatigue damage, but the reduction varies to some degree depending on the wind and wave loading for each environmental state. The lower environmental states show a larger reduction, while the damage reductions for environmental

states above the rated wind speed converge to similar levels. Compared to the values for 4% overall damping, the fatigue damage for 6% total damping reduces by an average of approximately 45%. This decrease is even more pronounced and reaches 75% when 11% total damping is considered. As shown before, the contribution of an environmental state to the overall fatigue of the structure depends on the combination of its probability of occurrence and absolute damage. In general, the higher environmental states have lower probabilities of occurrence but cause more damage. Environmental states 1 to 9 have a low contribution to the fatigue of the system due to their low normalised fatigue damage (Figure 6-8(a)). The most damaging environmental states are at and above the rated wind speed, with environmental states 14 and 18 contributing the most damage due to the combination of normalised fatigue damage and probability of occurrence (Table 3-7). The combined contribution of fatigue damage from environmental states 10 to 18 is more than 70% of the overall damage.

6.4.3.2 *Fatigue life comparison*

Figure 6-9 shows the fatigue life of the wind turbine (100% operational) based on the damage contributions obtained for the different damping values shown in Figure 6-8(b). The design fatigue life of 20 years is marked as a reference. An almost linear increase in fatigue life is observed when damping increases, from 16 years at 4% overall damping to 53 years at 11% damping. The changes in the overall fatigue life are consistent with the average reductions in the environmental states' damages as shown in Figure 6-8(a) and demonstrate the potential fatigue life extension of a wind turbine structure with additional damping, e.g. in the form of a tuned-mass damper or other structural modifications. Wind turbines are regularly shut down for short maintenance and inspection intervals, but breakdowns can lead to longer non-operational periods during operational environmental states until repairs can be scheduled. In a hypothetical scenario where the turbine is left parked for an extended period, the fatigue damage is increased, as was shown in section 6.4.2 from the comparison of operational and non-operational wind turbines. Assuming respectively 5% and 10% downtime (95% and 90% operational) and summing the proportional damage, a reduction in the fatigue life of the wind turbine of approximately 2% and 4% is predicted, indicating a potential danger of prolonged downtime.

Ignoring the diffraction effects on the wave loading, which was shown to over-estimate the hydrodynamic loads (by assuming constant inertia coefficient C_m=2.0, section 3.5.2) for environmental states with lower wavelengths (i.e. environmental states 1-8), was checked by conducting an additional full fatigue analysis with and without diffraction effects applied in the calculation of the wave loads for a representative total damping of 6%. It was found that the reduced wave loading due to the diffraction effects increases the fatigue life of the structure by approximately 10% (i.e. from 28 years to 31 years). The proportional damage of the lower environmental states (i.e. environmental states 1 to 8) was significantly reduced as the over-

conservatism associated with the wave period of 3s was considerable (see Table 3-6). However, the contribution of the damage of these environmental states to the overall damage of the wind turbine was limited and the most significant differences in the damage contributions were observed for the intermediate environmental states due to their higher contribution to the total damage (i.e. environmental states 9 to 14 with a high probability of occurrence). A more detailed breakdown and discussion of the changes in the damage contribution of the environmental states due to the hydrodynamic loads is given in Appendix-C.

It should be noted that for a non-operational wind turbine (i.e. parked turbine), where the fatigue damage is mainly driven by the wave loading, a higher level of over-conservatism in the fatigue life prediction would be expected. In the following investigation, a constant coefficient of inertia of C_m=2.0 was considered for simplicity due to its limited influence on the overall damage of the wind turbine in the operational scenarios, which are the focus of this research project.
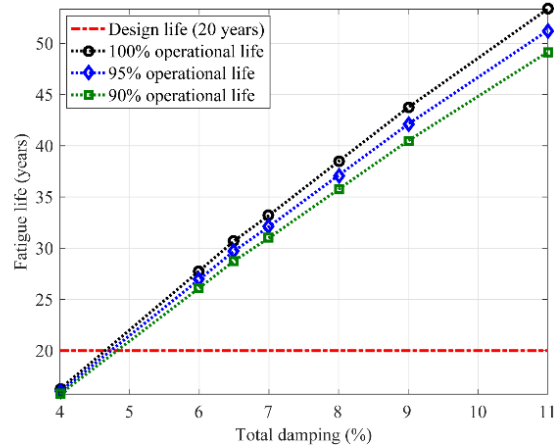
Figure 6-9. Fatigue life comparison for various levels of damping and operational life.

6.5 Approximate method for the prediction of fatigue life

In this section, an approximate method for the prediction of the fatigue life is proposed that avoids the need for the time-consuming time-domain analyses for each level of damping. Various hybrid frequency/time-domain fatigue analysis methods have been proposed in the literature (Low, 2011; Du et al., 2015; Michalopoulos, 2015; Michalopoulos and Zaaijer, 2015; Mohammadi et al., 2016; Yeter, Garbatov and Guedes Soares, 2016). Using a transfer function to obtain the response in the frequency-domain has become a common practice and various studies have made use of it as a replacement for time-domain simulations for the fatigue analysis of offshore structures (Etube, 1998; Halfpenny, 1999; Etube, Brennan and Dover, 2001; Tempel, 2006; Low, 2011; Du et al., 2015).

In this section, a hybrid time-domain approach is proposed, which requires the time-domain analysis for only one level of damping and uses it to predict the fatigue life at other damping levels with little extra effort. The outline of the simplified fatigue analysis is shown in Figure 6-10. In this method, the output stresses from the time-domain simulations of a reference damping level are transformed into the frequency-domain. The dynamic amplification of an equivalent single degree of freedom system (SDoF), which can be easily obtained from the dynamic properties of the wind turbine, is used as a substitute for the transfer function of the finite element model. The reference stresses are scaled by the ratio of amplification of the response between each damping level and the reference. Subsequently, the scaled stresses are transformed back into the time-domain. The fatigue damage in the wind turbine is calculated using the same procedure as the previous sections. Michalopoulos and Zaaijer (2015) first examined the use of dynamic amplification factor in the frequency-domain fatigue analysis for a quick assessment of the location variation influence within a wind farm. However, they found large differences in the respective environmental states' damages compared to the time-domain results, which was argued to be caused by the cycle counting method used. Here, the dynamic amplification factors were employed to assess damping variation influences, and the time-domain fatigue analysis was used to obtain more accurate results.
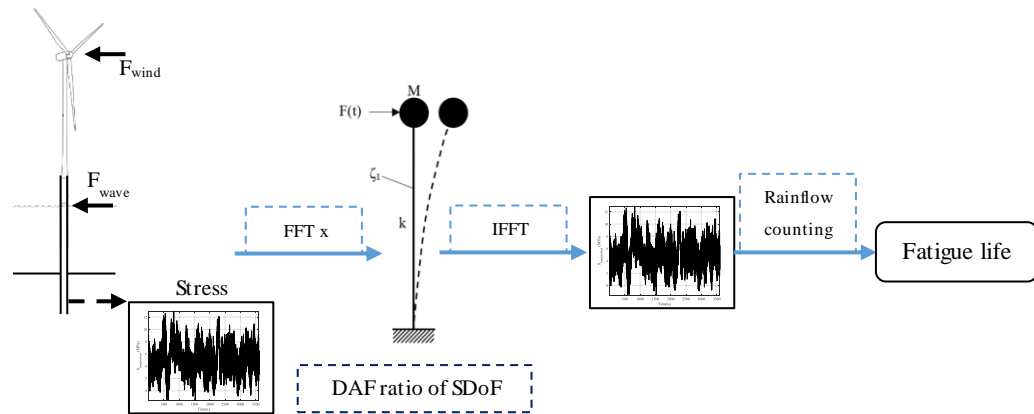
Figure 6-10. Schematic flow chart of the simplified fatigue analysis method. Offshore wind turbine sketch was retrieved from International Zinc Association (2011).

This method has the advantage of using the coupled time-domain simulations of a reference damping level as a benchmark and the rainflow counting technique, which is considered as an accurate method for the calculation of fatigue damages.

As a first step, to verify the application of the single degree of freedom dynamic amplification factors, they were compared with the amplification of the response in the finite element model. The amplification of the response in the finite element model was obtained from the magnitude of the transfer function of the moment to stress at 8m below the mudline. The mass of the equivalent single degree of freedom system is the first modal mass (M_1) and the stiffness (k)

chosen so that the first natural frequency is identical to that of the offshore wind turbine. The dynamic amplification factor (*DAF*) of a single degree of freedom system under harmonic loading is independent of the loading amplitude and is given by Equation (6-3):

$$DAF(\Omega) = \frac{1}{\sqrt{\left[1 - \left(\frac{\Omega}{\omega_1}\right)^2\right]^2 + \left[2\zeta_1\left(\frac{\Omega}{\omega_1}\right)\right]^2}},$$

(6-3)

where Ω is the force frequency, ω_1 is the first natural frequency of the system and ζ_1 is the total damping for the first mode. Figure 6-11 shows the dynamic amplification of the maximum stress (at 8m below the mudline) in the finite element model and the equivalent single degree of freedom system for a total damping of ζ_1=4%, as an example. The peak amplifications show a difference of approximately 3% while a consistent, but small, difference between the amplifications at higher frequencies is observed, which is caused by the consideration of higher modes in the finite element model. However, the ratio of amplifications at any two damping level matched well in both models.
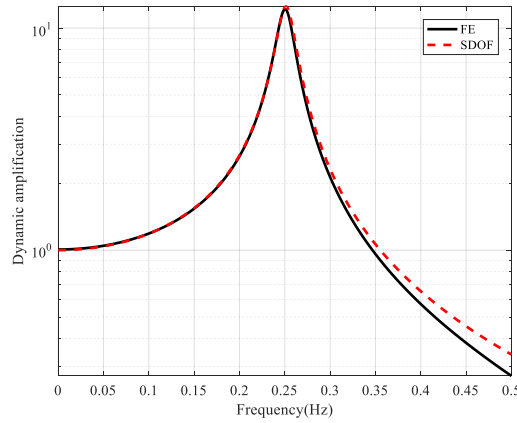
Figure 6-11. Comparison of the dynamic amplification of the maximum stress in the finite element model with the dynamic amplification in the single degree of freedom system for a total damping of ζ_1=4%.

6.5.1 Application to the harmonic excitation

Figure 6-12 shows this dynamic amplification factor on a log-linear scale for different levels of damping. The dynamic amplification factor primarily depends on the proximity of the force frequency (Ω) to the first mode of the structure (ω_1) (i.e. amplification of the response is the highest at the first natural frequency of the system) and the damping.
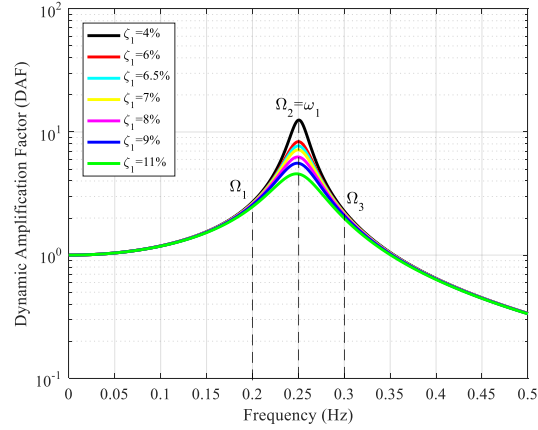
Figure 6-12. Dynamic amplification factors of the equivalent single degree of freedom system under harmonic loading.

According to Equation (6-3), at $\Omega = \omega_1$, the dynamic amplification term becomes $\frac{1}{2\zeta}$. To test the variation in the dynamic amplification at different force frequencies, a set of idealised harmonic wind and wave loads with identical amplitudes of 0.5MN and frequencies $\Omega_1 = 0.2Hz$, $\Omega_2 = 0.25Hz$ and $\Omega_3 = 0.3Hz$ were applied in the time-domain. These frequencies were indicated in Figure 6-12. Subsequently, the steady-state portion of the longitudinal stresses at the monopile (at 8m below the mudline) were compared for each force frequency.

As expected, the wind turbine monopile experiences the highest stresses when it is excited at the first natural frequency. As an example, at ζ_1=6%, the longitudinal stresses for the force frequencies $\Omega_1 = 0.2Hz$ and $\Omega_3 = 0.3Hz$ are smaller than those for $\Omega_2 = 0.25Hz$ by 65% and 77%, respectively. These reductions in the response were in agreement with those obtained from Equation (6-3). At the first natural frequency, larger differences between the longitudinal stresses at different damping levels was seen, due to the higher differences in the dynamic amplifications.

The influence of damping was further studied by considering a mid-level damping of ζ_1=7% (comprising 5% aerodynamic and 2% structural, soil and hydrodynamic damping) as a reference. The ratio of stresses in the 7% damping case and the stress at other damping levels showed that the time-domain harmonic loading ratios of the response match well with the theoretically calculated ratios of the dynamic amplifications of the response. A difference of up to 1% between the simulation and analytical stress ratios was seen.

To test the influence of the reference damping level, damping level of ζ_1=11% was selected as an alternative reference and the comparison of the stress ratios showed approximately 2% deviations. Thus, the selection of reference damping level is considered to have a minor influence on the outcome of this analysis.

Recall that the fatigue life (F.L) of the wind turbine is defined by:

$$F.L. = \frac{T_{simulation}}{\sum n_s / N_s},$$
(6-4)

where $T_{simulation}$ is the simulation time, n_s is the number of stress cycles in the simulation and N_s is the number of cycles to failure for the given stress range. In a harmonic loading scenario, for any two levels of damping from the simulations above, the number of cycles in the simulation, n_s, and simulation lengths, $T_{simulation}$, are the same for both stress ranges. Thus, the ratio of fatigue lives was simplified using the definition of S-N curve (shown in Equation (3-17)) and the resultant expression is given as:

$$\log\left(\frac{F.L._2}{F.L._1}\right) = -m(\log S_2 - \log S_1) = -m\left(\log \frac{S_2}{S_1}\right),$$
(6-5)

where S_i ($i=1$ or 2) is the stress range for the harmonic loading scenario i. Thus, for the harmonic loading response of the wind turbine, the fatigue life ratio $\frac{F.L._2}{F.L._1}$ shows a linear relationship with stress range ratio $\frac{S_2}{S_1}$ in log-log scale. The slope of the line is defined by "m", which is the negative inverse slope of the S-N curve. In fact, the S-N curve is bilinear and "m" can be equal to three or five, depending on the stress range. Equation (6-5) is only valid if both of the stresses correspond to the same segment of the S-N curve (i.e. the same "m"). Figure 6-13 shows the comparison of fatigue damage ratios from the simulations and Equation (6-5), for an example case of loading frequency of 0.25Hz. Figures for other load frequencies were not plotted to avoid repetition, but showed a similar trend. In this figure, the superscripts and subscripts of the axis labels refer to the reference and considered damping levels, respectively. As can be observed, the theoretical fatigue damage ratios show a close match (i.e. approximately 2% difference) with the fatigue damage ratios found from the time-domain simulations. At other force frequencies, similar deviations at the different damping levels were obtained.
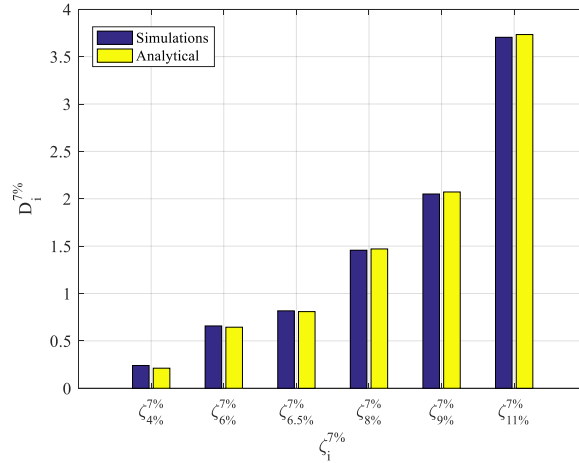
Figure 6-13. Comparison of the fatigue damage ratios from the simulations with the analytical predictions using the dynamic amplification factor of the equivalent single degree of freedom system, using ζ_1=7% as the reference.

6.5.2 Application to the environmental loads

In the frequency-domain, harmonic loads have one peak at their frequency and are zero at all other frequencies. However, aerodynamic and hydrodynamic loads are stochastic and have a broadband frequency content. As mentioned, the longitudinal stresses were extracted from the simulations for each environmental state (in the time-domain), and converted to the frequency-domain using Fast Fourier Transform (FFT). For each environmental state, the dynamic amplification ratios, with respect to the dynamic amplification of the reference case (ζ_1=7%), were multiplied by the Fourier transform of the longitudinal stress. Figure 6-14 shows the amplitude spectra of the reference and scaled (for total damping of ζ_1=4%) longitudinal stresses for environmental state 14 in the range of 0-0.5Hz frequencies, as an example. Two clear peaks are visible in Figure 6-14. The peak at around 0.15Hz corresponds to the peak frequency of the wave load while the peak at 0.25Hz corresponds to the first natural frequency of the wind turbine. 1P frequency is buried between the frequencies 0.15Hz and 0.25Hz, while the 3P frequency is further away at around 0.6Hz (not shown in Figure 6-14). As can be seen, frequencies below 0.2Hz and above 0.3Hz experience small change, while the amplitude of stress close to the natural frequency of the wind turbine shows the most significant amplification, similar to what was seen in the harmonic excitation scenarios.
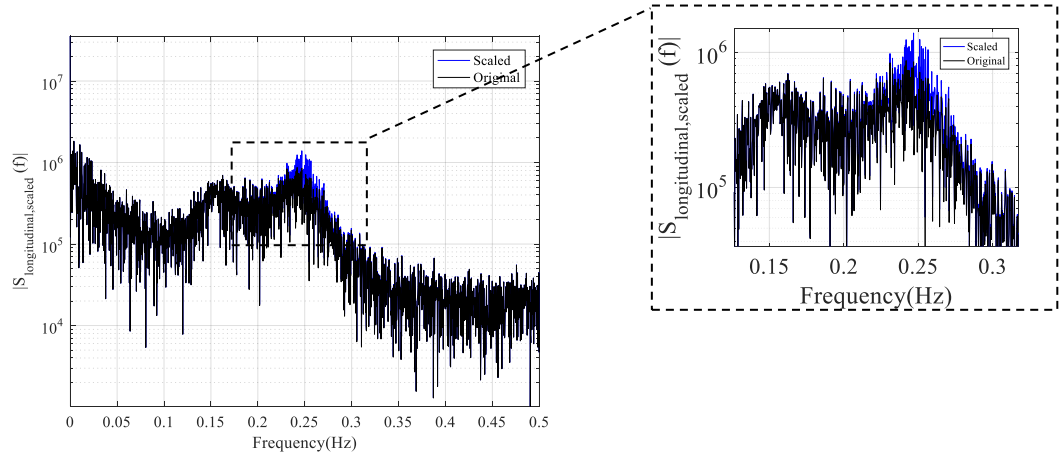
Figure 6-14. Comparison of the scaled FFT of the longitudinal stress for the model with ζ_1=4% in environmental state 14 with the original (unscaled) spectrum for ζ_1=7%, as an example. The highlighted region is zoomed to the right.

The inverse Fourier transformation of the stress spectrum resulted in the time series of the stress, which was rainflow counted to find the fatigue damage in each environmental state. Figure 6-15 compares the inverse Fourier transform of the scaled stress shown in Figure 6-14 with the retrieved stress output from the time-domain simulation of 4% damping for environmental state 14. As can be observed, a good match is found between the two time histories.
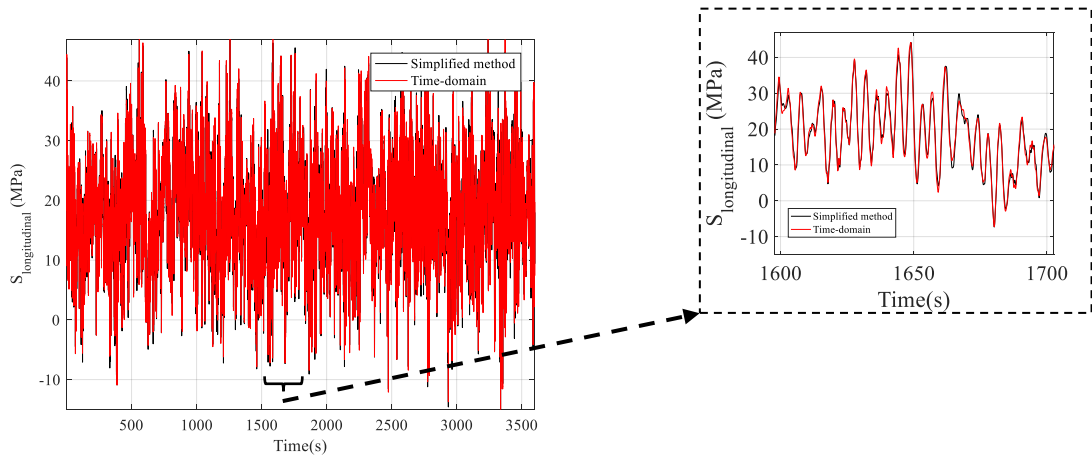
Figure 6-15. Comparison of the inverse Fourier transform of the scaled spectrum shown in Figure 6-14 with the stress outputs from the time-domain simulation of environmental state 14 for a total damping of 4%. The highlighted segment of the time history is zoomed to the right.

Figure 6-16 compares the normalised damage contributions calculated using the simplified fatigue analysis with those from the time-domain analysis for the highest damping level of ζ_1=11%. Figure 6-16 shows that the normalised damage contribution is slightly underestimated in the simplified method. Nevertheless, a good match is found between the two approaches. The simplified method underestimates the fatigue damage by up to 2%.
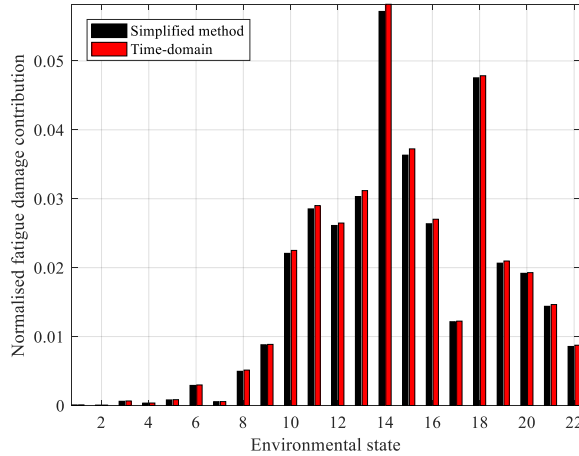
Figure 6-16. Comparison of the normalised damage contributions in the simplified fatigue analysis method with the time-domain results.

Figure 6-17 shows the predicted fatigue lives using the simplified method along with those predicted from the time-domain simulations. As can be seen, the fatigue life predictions show a close match. The fatigue life of the wind turbine at 11% damping shows the highest difference of 2% from the time-domain simulations, following the differences shown in Figure 6-16. The fatigue life prediction at other damping levels shows a very good match.
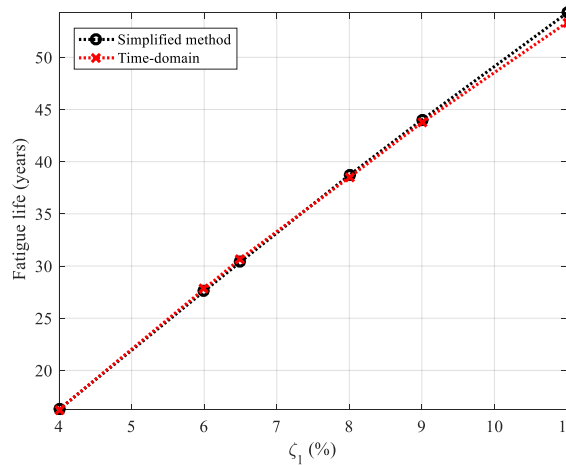
Figure 6-17. Fatigue life predictions from the simplified and the time-domain fatigue analyses of the wind turbine.

Although the simplified method does not consider the influence of higher natural frequencies, the small differences found in the fatigue life predictions show the applicability of the dynamic amplification factor to assess the influence of damping on the fatigue life of the wind turbine with a good accuracy and little extra effort. It should be noted that the accuracy of this method reduces for wind turbines located at deeper waters. In shallow to intermediate water depths, where monopile-supported offshore wind turbines are typically constructed, the method is reasonably accurate due to the dominance of the aerodynamic forces in the dynamic response of the wind

turbine, leading to a close approximation of the response using the dynamic amplification of an equivalent single degree of freedom system. However, for monopile-supported offshore wind turbines in deeper waters, the contribution of the hydrodynamic loads on the dynamic response of the system becomes more significant. The study of the limitations of this method, presented in detail in Appendix-D, showed that the deviation between the simplified method and actual response becomes significant when the amplitude of the wind load is less than half that of the wave load. Therefore, this limitation is particularly important for the consideration of parked wind turbines. For these structures, the proposed method can show slightly higher deviations from the time-domain simulation results for stress locations below the mean sea level. However, in all scenarios, the proposed method is reasonably accurate for all stress locations above the mean sea level.

It should also be noted that the deviation between the simplified method and the actual response of the system only occurs at frequencies above the first natural frequency of the wind turbine. Offshore wind turbines are typically designed using a soft-stiff approach and the peak frequency of the hydrodynamic loads is below the first natural frequency of the structure. For a representative JONSWAP spectrum peak at 0.1 Hz with the bulk of the spectral density below 0.2 Hz, the wave loads will have a very small spectral density at frequencies around and above the first natural frequency of the wind turbine. Therefore, it can be argued that the deviation between the simplified method and the real response remains small for most offshore wind turbines. A similar simplified analysis to Appendix-D can be implemented in practice to examine the validity of the approximate method for other wind turbines. The main advantage of this method is in its simplicity and the amount of time and effort that can be saved by avoiding the computationally expensive time-domain simulations to assess damping variations in offshore wind turbines at the preliminary stages of their design.

6.6   Summary

This chapter aimed to investigate the influence of damping on the fatigue of the wind turbines using the time-domain simulation of the environmental loads and structural response. In addition, the sensitivity to the operational regime of the turbine, and application of variable damping was studied. Fatigue damage in the monopile is mainly driven by the bending moment due to turbine and wave loads on the wind turbine. These were calculated for a range of environmental states for operational and non-operational regimes. It was anticipated that the majority of the states out of the operational range are below the cut-in wind speed, which has a marginal contribution to the fatigue damage of the offshore wind turbine. States with high wind speeds and wave heights caused significant normalised fatigue damage per time, but the actual overall contribution to the fatigue life was less severe due to their lower probability of occurrence. Consideration of variable

damping in the fatigue analysis increased the predicted fatigue life by up to 7%. Increased aerodynamic damping above the rated wind speed of the turbine reduced the fatigue damage of environmental states with higher damage contribution. However, the estimation of varying damping levels has significant uncertainties, and the rather small difference in predicted fatigue life suggested that in practice assuming a constant aerodynamic damping throughout leads to acceptable fatigue life estimates.

Unexpected shutdowns of the wind turbine during operational environmental states change the level of loading on the structure and result in the absence of aerodynamic damping. It was shown that the absence of aerodynamic damping has a larger influence on the fatigue damage than the reduced loading from the wind, resulting in a reduced fatigue life by up to 60%. In the case of significantly prolonged maintenance or shutdown, this could reduce the fatigue life to an unsafe level, depending on the targeted design life.

The influence of damping in limiting fatigue damage in offshore wind turbines was shown to be important. The variable component of the longitudinal stress in the monopile showed a reduction of approximately 18% for an increase of 7% in the overall damping of the system, leading to an average reduction of the fatigue damage by up to 60% for different environmental states. The predicted fatigue life of offshore wind turbines showed an almost linear increase with the level of damping, from 16 years at 4% overall damping to 53 years at 11% damping.

A hybrid time-domain approximate method, which requires a single set of time-domain simulations as a benchmark to calculate the fatigue life at other damping levels was proposed and tested. For each environmental state, the longitudinal stress from the simulations at a reference damping level was scaled according to the dynamic amplification of the response of an equivalent single degree of freedom system to obtain the stress at other levels of damping in the monopile. A close match was found between the simulation results and those from the simplified method. This method could reduce the computation time required for the assessment of fatigue influences of damping, is fairly simple to implement and results in accurate predictions.

7 Scour Influence on Fatigue Life

In this chapter, the influence of local scour and backfilling on the dynamics of offshore wind turbines is investigated. Short-term effects of scour and backfilling are studied using static and modal analyses. Time-domain fatigue analyses are performed to investigate the changes in fatigue life (i.e. long-term effects) due to scour and backfilling phenomena. Results from the short and long-term analyses were used to propose an approximate method to predict the fatigue life for various levels of scour, only requiring one fatigue life calculation. Considering the scour and backfilling effects, this would be a valuable tool to ensure a cost-effective fatigue design of offshore wind turbines without the need for the computationally intensive full fatigue analysis.

Section 7.1 shows the details of the implementation of scour in the finite element model. Section 7.2 discusses the static and dynamic influences of scour. The long-term influence of scour and backfilling, along with the study of the modal parameters recovery due to backfilling, are considered in section 7.3. Scour effects are discussed in section 7.4 to establish an approximate method for a faster fatigue life prediction in the preliminary stages of design. Finally, the summary of the results is given in section 7.5.

7.1 Finite element analysis details

In this chapter, the beam element model of the NREL 5MW wind turbine with the soil profile shown in Table 3-3 was used. Figure 7-1 illustrates the application of scour, damping and loads in this finite element model. Scour was implemented in the models by removing the p-y springs for the considered level. In the case of backfilling, the springs where replaced with a modified stiffness based on the backfilled material density.
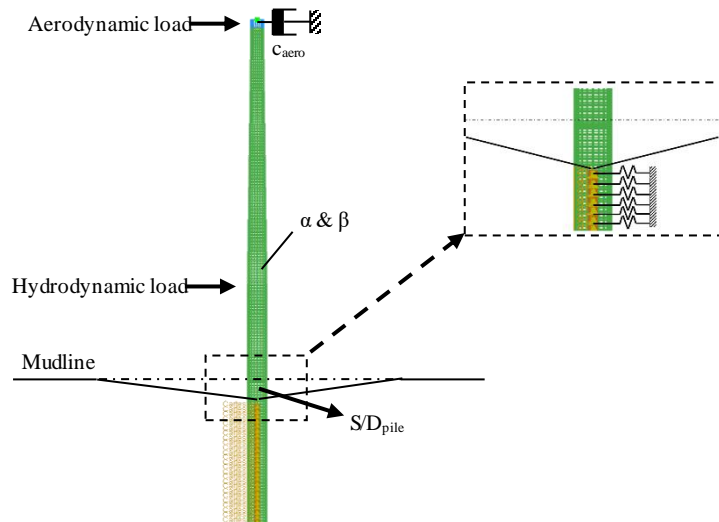
Figure 7-1. Layout of the beam element model, showing the environmental loads, damping, and scour applications.

A constant value of damping was applied throughout all analyses. The aerodynamic damping, which is implemented in the form of a dashpot at the top, provides $\zeta_{aerodynamic}$=4% in the first mode. This value is lower than that used in Chapter 6 for a similar wind turbine, which leads to slightly lower fatigue life. Structural, hydrodynamic and soil damping was applied as Rayleigh damping, providing a first mode modal damping of ζ_{other}=2%, which results in a total first mode damping of ζ_{total}=6%. Rayleigh damping parameters (α and β) and the dashpot constant ($c_{aerodynamic}$) were determined according to Equations (6-1) and (6-2). The turbine was considered to be operational with variable rotor speed and pitch angle depending on the mean wind speed. The rotor and blade pitch status were determined according to Table 3-5.

Table 7-1 shows the range of scour depths modelled. The no scour case (scenario 1) was considered as a reference for the future comparisons. The maximum scour depth considered was $1.5D_{pile}$ (i.e. 9m) that is slightly higher than the recommended local scour depth ($1.3D_{pile}$) in the DNV guidelines (2013).

Table 7-1. Different considered scenarios for the scour depth in the operational wind turbine.

Scenario	Scour depth (S/D_{pile})
Scenario 1	0
Scenario 2	0.25
Scenario 3	0.50
Scenario 4	0.75
Scenario 5	1.00
Scenario 6	1.25
Scenario 7	1.50

Table 7-2 shows the backfilling scenarios considered. In all scenarios, the scour depth was assumed to be backfilled (naturally or artificially) from a maximum depth of $1.5D_{pile}$. The

backfilling depth was varied from $0.5D_{pile}$ to $1.0D_{pile}$. The backfilling material was considered to be of the same type as the original soil, but with different densities due the lower compaction of the soil in backfilling (Sørensen and Ibsen, 2013). Sørensen et al. (2010; 2013) suggested and considered backfilled material densities of up to 85% of the original soil. In this research, three variations of the backfilled material density, which affects the stiffness of the soil, were considered with respect to the original soil density (of the top soil layer):

- $I_{backfilled}=20\%$

- $I_{backfilled}=40\%$

- $I_{backfilled}=80\%$

Table 7-2. Different backfilling scenarios in the operational wind turbine.

Scenario	Backfilling depth (S/D_{pile})	Backfilled material density, $I_{backfilled} = \rho_{backfilled}/\rho_{original}$ (%)
Scenario 8		20
Scenario 9	From 1.5 to 0.50	40
Scenario 10		80
Scenario 11		20
Scenario 12	From 1.5 to 0.75	40
Scenario 13		80
Scenario 14		20
Scenario 15	From 1.5 to 1.00	40
Scenario 16		80

These scour and backfilling depths were considered to be in equilibrium in each scenario, and the fatigue life was predicted assuming that the scour depths considered have been present and unchanged throughout the life of the structure. However, the influence of backfilling period was accounted later in the calculations.

7.2 Short-term effects of scour

7.2.1 Scour effects on natural frequency

This section investigates the variation of the natural frequency of the wind turbine structure due to scour. Figure 7-2 shows the changes in first and second natural frequencies as a result of scour. The variations in natural frequencies are compared to the original frequencies of the wind turbine (i.e. no scour scenario).

Results show that the first natural frequency decreases by approximately 2.2% while the second natural frequency shows a maximum reduction of 3.6%, as a result of $1.5D_{pile}$ local scour hole. The resultant decrease in the natural frequencies increases nonlinearly with increasing scour depth for low depths and tends to become fairly linear for scour depths of $0.75D_{pile}$ and higher. It should be noted that as the recommended design scour depth is $1.3D_{pile}$, the reductions of natural

frequencies at this scour level are smaller than 2%. The changes shown are smaller than the previous results (Zaaijer, 2005; Tempel, 2006). However, it should be noted that some variability in the results is expected in different offshore wind turbines with different soil conditions.
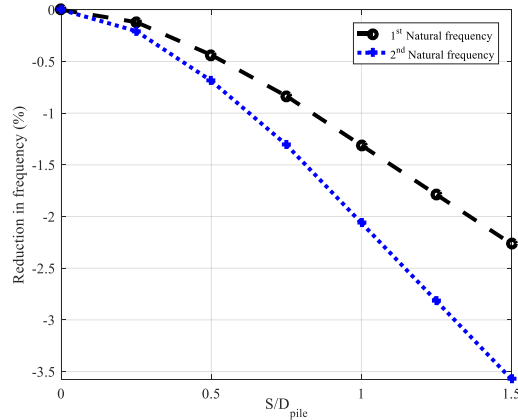
Figure 7-2. Changes in the natural frequencies due to scour with respect to the natural frequency of the no scour scenario.

Changes in the natural frequency of 2.2% and 3.6% can be caused by different sources. Accordingly, it is difficult to attribute such variations only to scour and detect the occurrence of scour from such measurements in practice. Consequently, it is much safer to assess the scour effects on the natural frequencies at the design stage.

7.2.2   Scour effects on the bending moment

Scour increases the exposed length of the wind turbine support structure. In monopile-supported offshore wind turbines, this leads to an increase in the bending moment in the structure below the seabed. Figure 7-3(a) shows the change in bending moment in the monopile for a notional static wind and wave loads of 1MN. As expected, scour does not result in any change in bending moment above the mudline. The increase in bending moment occurs at around the location of its peak, which is variable for different structures but tends to be between the original mudline and z=-15m depending on the soil profile. Also, scour shifts the location of maximum bending moment slightly down. The maximum scour depth of $1.5D_{pile}$ increases the bending moment by approximately 9% compared to the no scour scenario.

(a)   (b)
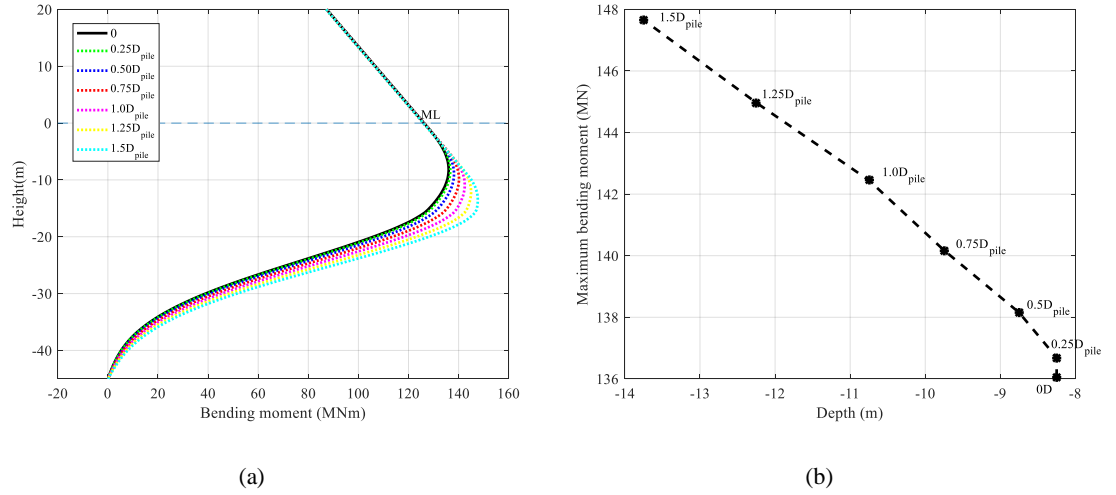
Figure 7-3. (a) Bending moment in the monopile (mudline is marked at zero depth) and (b) variation of maximum bending moment with its location below mudline due to various scour depths.

Figure 7-3(b) shows the variation of the maximum bending moment in the monopile against its location for different scour depths. The location of maximum bending moment shifts by almost 6m down as the scour depth increases, as shown in Figure 7-3(b). Misalignment between the wind and wave loads could result in a slightly different shift in the location of the maximum bending moment. Locating the maximum bending moment is important in the fatigue design of offshore wind turbine structures against scour, as it is directly linked to the stresses in the structure.

In the preliminary stage of design, a certain level of uncertainty exists around the exact location of welds in the monopile. As the location of maximum stress was shown to be variable due to scour, the fatigue life influences of scour were studied at a range of depths (from -8m to -15m according to Figure 7-3(b)), consisting of three nearby locations at the monopile where the weld is likely to be positioned. The following locations are all measured from the mudline of the no scour case:

1. $z_1 \approx$ -8m
2. $z_2 \approx$ -10.5m
3. $z_3 \approx$ -12m

The selected locations are carefully chosen to include the bending moment variations for all scour depths in the considered range adequately, as shown in Figure 7-3(b).

In brief, the natural frequencies of the wind turbine show small changes as a result of scour. The maximum bending moment in monopile increases significantly, which can have a more significant effect on the fatigue life of the wind turbine. The location of maximum stress also appears to shift down, which have to be considered in their fatigue analysis.

7.3 Fatigue analysis – long-term effects of scour

7.3.1 No scour

First, the fatigue damage at the selected locations in the monopile is studied for the wind turbine with no scour (i.e. scenario 1). Figure 7-4(a) shows the normalised damage caused in each environmental state at $z_1 \approx$ -8m, $z_2 \approx$ -10.5m, and $z_3 \approx$ -12m. The fatigue damages are normalised against the damage corresponding to a fatigue life of 20 years. In general, a small variation is observed among the normalised fatigue damages of the environmental states at the considered depths. These variations depend on the bending moment seen in Figure 7-3. The lower environmental states (up to #8) produce minor fatigue damage compared to the damage caused by the higher environmental states. As shown in Chapter 6, although the damage resulted in each environmental state increases overall as a result of higher amplitudes of wave and wind forces, slight variations are present due to some variations in the frequency matching, causing the differences in dynamic amplifications. In addition, the normalised fatigue damages at z_2 are slightly higher (by up to 1%) than at z_1 in the environmental states with V_w=18m/s and higher (i.e. environmental states 16 and above). Figure 7-4(b) shows the normalised damage contribution of every environmental state. The combined contribution of fatigue damage caused in the environmental states 10 to 18 adds up to more than 70% of the overall fatigue in the monopile.

(a)   (b)
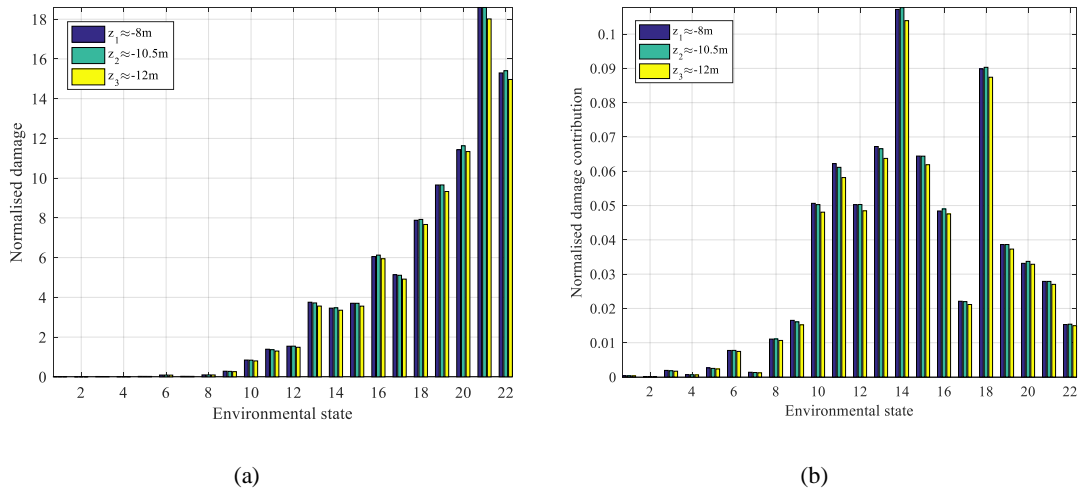
Figure 7-4. (a) Normalised fatigue damage and (b) normalised fatigue damage contributions of the environmental states at $z_1 \approx$ -8m (used in Chapter 6), $z_2 \approx$ -10.5m, and $z_3 \approx$ -12m.

The variation in the normalised fatigue damage contributions, depending on the selected locations, is around 1%, which is similar to the normalised damages observed in Figure 7-4(a). Summing the fatigue damages from all environmental states' contributions gives a fatigue life of approximately 28 years at $z_1 \approx$ -8m. The fatigue life at $z_2 \approx$ -10.5m is only a slightly short of 28 years, and at $z_3 \approx$ -12m is closer to 29 years. The variation in the fatigue life at the different locations in scenario 1 (i.e. no scour) is probably well within the margin of calculations of the

method. However, based on the observations made in Figure 7-3, these variations are expected to grow with the scour depth.

7.3.2 Scour with no backfilling

Figure 7-5 shows the change in the normalised fatigue damage contribution for every environmental state due to scour depths of up to $1.5D_{pile}$ at the depth of $z_3 \approx -12m$, as the worst case of the three. Similar graphs for other depths are not shown to avoid repetition, but are discussed in the text. The increase in fatigue damage appears to be slightly higher in the environmental states with higher damage contributions, but fairly similar in other environmental conditions in Figure 7-5.
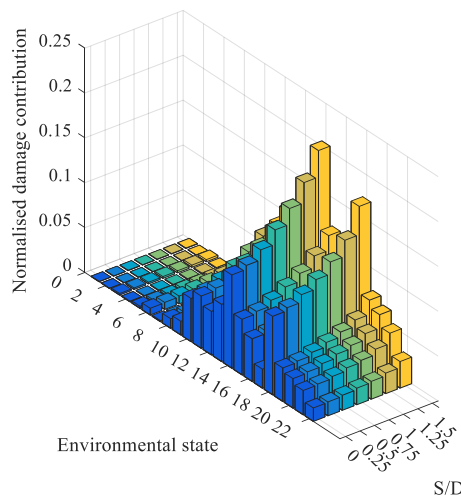
Figure 7-5. Comparison of the scour effects on the fatigue damage contributions of the environmental states at $z_3 \approx -12m$.

Scenario 1 (i.e. no scour) was taken as the reference for the comparisons. Figure 7-5 shows that the fatigue damage contribution of $0.25D_{pile}$ is higher than the no scour case by a small amount. However, the fatigue damage contributions show a slightly higher increase for the scour depths of $0.25D_{pile}$ to $1.0D_{pile}$. A higher increase in the fatigue damage contributions is observed at $1.25D_{pile}$ and $1.5D_{pile}$. According to Figure 7-5, at $z_3 \approx -12m$, a maximum increase of 102% in the normalised damage contributions is observed for the scour depth of $1.5D_{pile}$, compared to the reference scenario.

At $z_1 \approx -8m$ and $z_2 \approx -10.5m$, the relative variations in the fatigue damage contributions showed a similar growth for small to moderate scour depths (up to $1.0D_{pile}$). However, for higher scour levels (>$1.0D_{pile}$), a less drastic increase was observed. The highest difference in the normalised fatigue damage contributions for different scour depths appeared to be by a maximum of approximately 40% and 75% at $z_1 \approx -8m$ and $z_2 \approx -10.5m$, respectively. The combined effect of the

increase in bending moment and the shift in the location of maximum bending moment resulted in the highest increase at $z_3 \approx$ -12.5m and the lowest variation at $z_1 \approx$ -8m.

Figure 7-6 shows the predicted fatigue life of the wind turbine at the considered depths for different scour levels. The design life of 20 years is also marked as a reference. The predicted lives in this figure are obtained based on 100% operation of the wind turbine. When no scour has occurred around the pile, the fatigue life is the lowest at $z_1 \approx$ -8m, which would be a critical location for a weld. The predicted fatigue life at $z_1 \approx$ -8m reduces by 29% for a scour depth of $1.5D_{pile}$, which does not fall below the design life of 20 years. However, the downward shift in the location of maximum bending moment, as a result of scour, leads to a higher rate of fatigue life reduction at the lower locations (i.e. $z_2 \approx$ -10.5m, and $z_3 \approx$ -12m). The decrease in fatigue life is approximately 40% at the intermediate location, $z_2 \approx$ -10.5m. However, the variation in the fatigue life grows to more than 45% at $z_3 \approx$ -12m for the highest scour depth. At these two locations, the fatigue life appears to fall below the design life for the scour depth of $1.0D_{pile}$. At $z_2 \approx$ -10.5m and $z_3 \approx$ -12m, the fatigue life is approximately 2 years shorter than the design life for a scour depth of $1.25D_{pile}$, which is close to the maximum recommended scour depth ($1.3D_{pile}$) in DNV (2013). This proves how important the consideration of bending moment shift is in the fatigue limit state design of the monopile-supported offshore wind turbines.
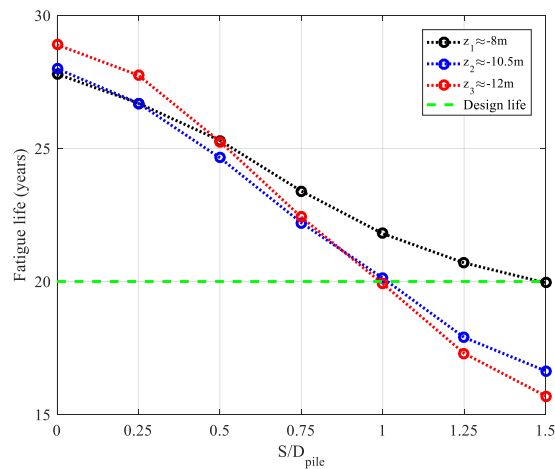
Figure 7-6. Fatigue life predictions for the variations of scour depth around the wind turbine at $z_1 \approx$ -8m, $z_2 \approx$ -10.5m, and $z_3 \approx$ -12m.

These results are based on the presence of aerodynamic damping and operation of the wind turbine. In the case of a stationary wind turbine, the fatigue life predictions could be reduced considerably, as shown in Chapter 6. However, the variations in the fatigue life predictions due to scour should be fairly similar to the operational wind turbine, as the relative change in the location of bending moments could be fairly similar.

7.3.3 Scour with backfilled material

Backfilling of the scour hole has been shown to benefit the offshore wind turbine support structures by limiting the fatigue damages (Sørensen and Ibsen, 2013). In this study, the modal properties and fatigue life of the wind turbine are re-evaluated considering natural backfilling of the scour hole. The original depth of the scour before backfilling was assumed to be $1.5D_{pile}$ and the backfilled material density was considered to be lower than that of the original soil. In the backfilled models, for simplicity, it was assumed that the scour hole is filled up instantly from the original depth to the backfilled depth, as shown in Figure 7-7 (e.g. when backfilling to $1.0D_{pile}$ is considered, the scour hole does not vary gradually from $1.5D_{pile}$ to $1.0D_{pile}$).
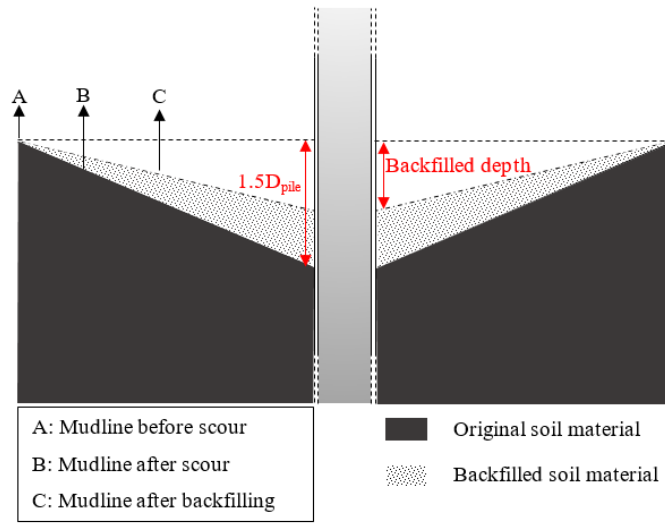
Figure 7-7. Diagram of the backfilling of the scour hole ($1.5D_{pile}$) with respect to the original (zero scour) and scoured mudline levels.

To study the recovery of the short and long-term effects of backfilling, the modal and fatigue life predictions of the scenarios with the same scour hole, but original soil density, were considered as references in the backfilling scenarios. For instance, the modal and fatigue life predictions of backfilling scenarios 8, 9, and 10, which were backfilled from $1.5D_{pile}$ to $0.5D_{pile}$ and have different backfilled material densities, were compared with the results of scenario 3, where the scour depth is $0.5D_{pile}$ with the original soil density.

As the density of the backfilled material gets closer to the original soil density, the foundation stiffness is expected to get closer to that of the original soil. Therefore, modal and fatigue life predictions are expected to become close to the reference scenarios for higher backfilled material densities. Table 7-3 compares the first natural frequency in each backfilling scenario. Although the backfilled models do not have the same stiffness properties as the original soil, the natural frequencies for the backfilled scenarios are only different by a maximum of 1%. The largest differences between the natural frequencies are mainly observed for the scour hole of $0.5D_{pile}$.

Table 7-3. Comparison of natural frequencies for backfilled scour hole and normal scour.

Backfilled depth	$I_{backfilled}$ (%)	$f_{1,scour}$ (Hz)	$f_{1,backfilled}$ (Hz)
0.5D$_{pile}$	20		0.249
	40	0.251	0.250
	80		0.250
0.75D$_{pile}$	20		0.250
	40	0.250	0.250
	80		0.250
1.0D$_{pile}$	20		0.248
	40	0.248	0.248
	80		0.248

The density of backfilled material seems to have a very small effect on the natural frequency. Therefore, it is shown that backfilling of the scour hole could recover the natural frequency of the wind turbine structure to a value close to the natural frequency of the same scour depth with the original soil. A similar observation was made by Damgaard et al. (2013).

Figure 7-8 shows the predicted fatigue lives for backfilling of the scour hole to 0.5D$_{pile}$, 0.75D$_{pile}$ and 1.0D$_{pile}$ depths and with different backfilled material densities, measured at $z_3 \approx -12$m, as the worst case of the other two measurement locations. The relative backfilled material density of $I_{backfilled}=100\%$, refers to the scenarios with the same scour depth and with the original soil in place (i.e. the reference scenarios in this section). As expected, the fatigue life increases with the density of the backfilled material.
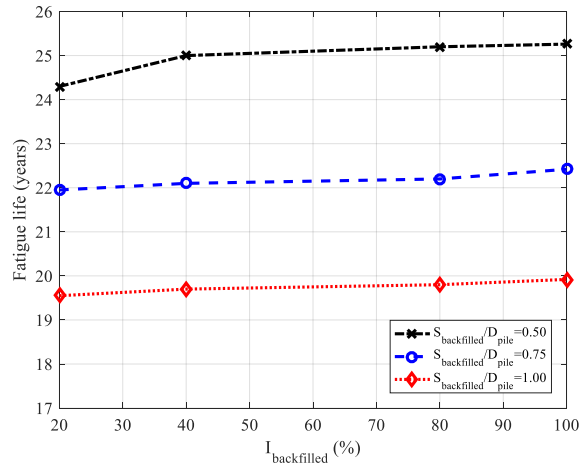
Figure 7-8. Fatigue life prediction for various backfilled material densities, measured at $z_3 \approx -12$m.

In general, the influence of backfilled material density is slightly more pronounced when the scour hole is backfilled to 0.5D$_{pile}$. In this case, a maximum decrease of a year is observed for a material density of $I_{backfilled}=20\%$, compared to the fatigue life of $I_{backfilled}=100\%$. For higher backfilled material densities, an even lower deviation is observed. This level of change in the fatigue life is within the margins of calculations. Accordingly, the influence of backfilled material density can

be regarded as negligible even when the scour hole is backfilled with a material density of $I_{backfilled}$=20%. It should be noted that this level of influence of the material density could be a result of the soft soil at the top of the profile, which reduces the contribution of the top soil layers to the overall foundation stiffness in the wind turbine. Research has shown that the backfilled material has a relative density close to 80% of the original soil, which results in a marginally lower fatigue life than with the original soil. Therefore, consideration of the fatigue life with the original soil at the same depth as the backfilled depth, instead of the lower material density, can be used in practice to model backfilling, as it yields a sufficiently close fatigue life prediction. In the following, a backfilled material density of $I_{backfilled}$=40% is used as an intermediate but marginally conservative estimate for the fatigue life.

The scour and backfilling may become a recurring matter depending on the offshore conditions, as discussed in Chapter 2. Consequently, the time scale of the backfilling process can be factored in the results by considering the portion of the life of the wind turbine during which the scour hole was backfilled to a certain level. To take this into account, linear interpolation of the fatigue damages from the simulations for the scour and backfilled depths based on the periods that each were present around the monopile can be used to find a more realistic prediction for the fatigue life. An application of this method is to monitor the fatigue life of the wind turbine based on onsite measurements of the scour depth over the operational life of the wind turbine. Another practical interpretation of this method can be applied to the artificial backfilling of the scour hole, where the current scour depth around the pile is known and the possible long-term benefits of the artificial backfilling of the scour hole is to be assessed. Figure 7-9 shows an example application of this assessment, where the changes in the fatigue life of the structure for a range of backfilled periods between 30% and 90% of the wind turbine's life are investigated.
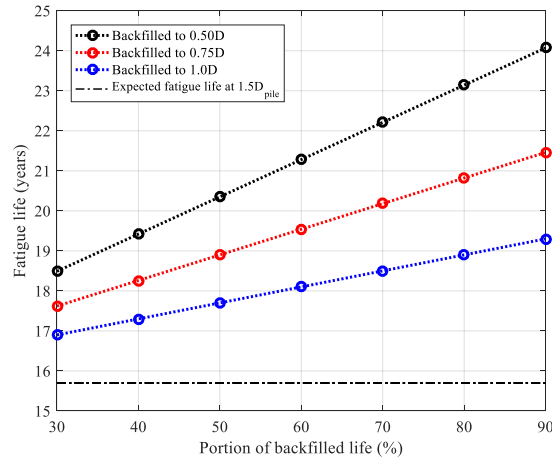
Figure 7-9. Long-term benefits of backfilling the $1.5D_{pile}$ scour hole (with $I_{backfilled}$=40%) in terms of the portion of offshore wind turbine's life and backfilled depth.

As before, the original scour depth is considered to be $1.5D_{pile}$, which is backfilled to $0.5D_{pile}$, $0.75D_{pile}$ or $1.0D_{pile}$. Note that the fatigue life of the wind turbine is less than the design life of 20 years with the current scour depth (i.e. $1.5D_{pile}$). Figure 7-9 shows that in spite of the increase in the fatigue life, backfilling to any scour depth does not necessarily ensure a safe fatigue life. For instance, extending the fatigue life beyond 20 years (i.e. design life) depends on the period of backfilling for $0.75D_{pile}$ and $0.5D_{pile}$, while backfilling the scour hole to $1.0D_{pile}$ does not extend the fatigue life beyond the design life. Moreover, a more pronounced increase in the fatigue life is observed when the scour hole is backfilled to lower depths. In general, it can be stated that fatigue life extension is dependent mostly on a combination of the backfilled scour depth and the backfilling period. Nevertheless, consideration of backfilling shows a significant recovery in the long-term predictions and illustrates how valuable and cost saving these considerations could be in practice.

7.4 Approximate fatigue life prediction method

In this section, the nature of scour effects on the long-term dynamic response of offshore wind turbines is studied to develop an approximate method for the prediction of fatigue life in offshore wind turbines due to scour. Initially, the scour effects in the wind turbine structure were examined in an equivalent single degree of freedom (SDoF) system to simplify the study of the dynamic response of the structure. It was assumed that the first natural frequency of the wind turbine is equal to the first natural frequency of the single degree of freedom system (ω_1). The modal mass (M), damping (ζ_1) and stiffness (k) are also equivalent to that of the reference wind turbine.

Assuming that a harmonic force with a mean and amplitude of F_m and F_a, and frequency Ω is applied to this single degree of freedom system, the total response of the system is given by Equation (7-1). The static and dynamic parts of the response are also labelled in this equation.

$$u(t) = \underbrace{F_m/k}_{static\,response} + \overbrace{F_a/k}^{Quasi-static}\underbrace{\overbrace{\frac{1}{\sqrt{\left[1-\left(\frac{\Omega}{\omega_1}\right)^2\right]^2 + [2\zeta_1\left(\frac{\Omega}{\omega_1}\right)]^2}}}^{Dynamic\,amplification}}_{Dynamic\,response}.$$

<div align="right">(7-1)</div>

It was previously shown that the natural frequency of the wind turbine (especially the first natural frequency) experiences minor changes as a result of scour (i.e. maximum of 2.2% for a scour depth of $1.5D_{pile}$). However, the bending moment in the monopile showed a significant difference in magnitude and location as a result of the higher free length of the structure and changes in the stiffness of the soil support. Comparison of these findings with the static and dynamic components of the single degree of freedom system's response in Equation (7-1) indicates that the dynamic amplification term in the response experiences minor change because of the small variations in the natural frequency due to scour. This minor change was tested and is shown in Figure 7-10 in the form of the steady-state response of the wind turbine structure at $z_1 \approx$ -8m for the considered scour scenarios. Similar results for the other locations was obtained but not presented to avoid repetition. The damping (ζ_1) in the model was kept constant in all scenarios. As can be seen, the shift in the natural frequency is relatively small. The variations in the natural frequency of the wind turbine are the same as the ones seen in Figure 7-2. Figure 7-10 shows that the longitudinal stress increases by approximately 4% at $z_1 \approx$ -8m. A slightly higher increase of up to 8% in the peak response of the wind turbine, arising from the static response variations, was observed at $z_2 \approx$ -10.5m and $z_3 \approx$ -12m. These variations in the longitudinal stress are close to the results seen in Figure 7-3.
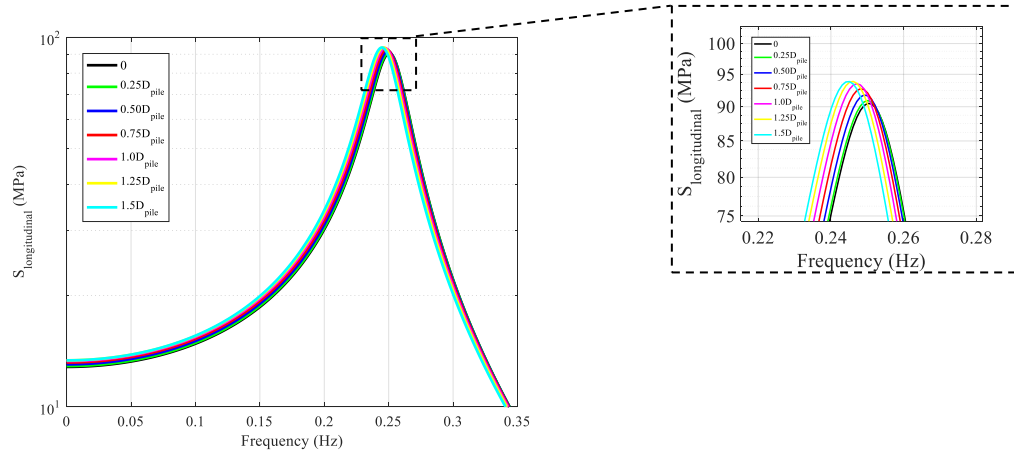
Figure 7-10. Comparison of the steady-state response of the wind turbine structure to an example loading for various scour depths at $z_1 \approx$ -8m. The peak response is zoomed to the right.

As the change in the dynamic amplification of the response is small, the variation caused by scour in the response of the system can be attributed to the static and quasi-static parts of the response.

The variations in static and quasi-static parts of the response are resulted by the changes in the in the free-length of the monopile and slight variations in the soil stiffness as a result of scour.

As the dynamic amplification of the response is more or less the same for all scour levels, studying the signals in the frequency domain does not provide a clear advantage in the analysis of scour effects. Accordingly, the mean and standard deviation of the stress responses in the time-domain were measured as a proxy to characterise the vibration of the wind turbine.

As shown in Chapter 6, for two sets of harmonic loads with the same force frequency but different magnitudes, the ratio of fatigue lives ($F.L_i$) is given as:

$$\log(\frac{F.L_{.2}}{F.L_{.1}}) = -m(\log S_2 - \log S_1) = -m\left(\log\frac{S_2}{S_1}\right).$$
(7-2)

In this section, application of this relationship to the standard deviation of the stresses is examined. A rough comparison of the stresses in the monopile showed that the majority of stress cycles in the monopile are in the range of stresses that corresponds to the part of S-N curve with $m=5$. These stress cycles also contribute to the majority of the fatigue damage in the monopile. Accordingly, here, the slope of fatigue life and stress ratios relationship in log-log scale was considered as a constant $m=5$ to simplify the fatigue life comparisons.

The variations in the static and quasi-static components of the dynamic response of the wind turbine were determined by a set of ratios for the mean and standard deviation of the stress time histories. Variation in the mean stress are thought to represent the static response changes while the changes in the standard deviations represent the variation in the quasi-static response of the wind turbine. For every environmental state, the changes in the mean and standard deviation of the stresses were calculated with respect to the mean and standard deviation of the model with no scour (scenario 1). The calculations were done for all of the previously considered locations (i.e. $z_1 \approx$ -8m, $z_2 \approx$ -10.5m, and $z_3 \approx$ -12m). The variations for the standard deviations were defined by the ratio shown in Equation (7-3).

$$\Delta\sigma_i^{k_{ES}} = \frac{\sigma_i^{k_{ES}}}{\sigma_0^{k_{ES}}},$$
(7-3)

where k_{ES} refers to the number of each environmental state, i corresponds to the scour depth in the model, σ is the standard deviation of the stress time history. The mean stress ratios $\Delta\bar{S}$ were defined in a similar manner. The contribution of the difference in each environmental state was accounted for by taking the weighted average of the stress ratios based on the probability of occurrence of each environmental state. The resultant ratios were called $\Delta\bar{\sigma}_{weighted}$ and $\Delta\bar{S}_{weighted}$ for the standard deviations and means, respectively. Figure 7-11 shows the weighted

average changes in the mean and standard deviation ratios of the stresses at $z_1 \approx$ -8m, $z_2 \approx$ -10.5m, and $z_3 \approx$ -12m for various scour depths.
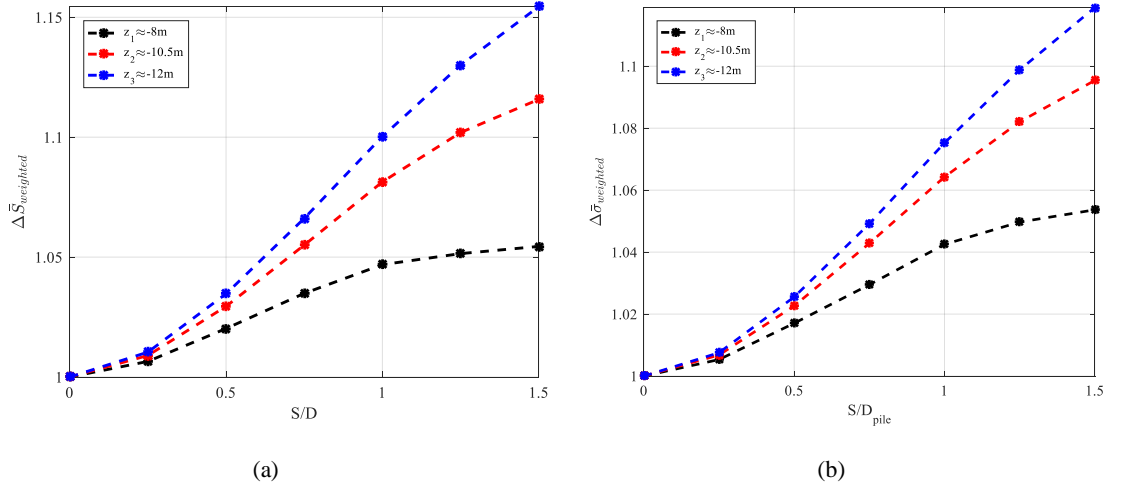
Figure 7-11. The weighted average of (a) the mean stress ratios and (b) the stress standard deviation ratios for various scour levels at $z_1 \approx$ -8m, $z_2 \approx$ -10.5m, and $z_3 \approx$ -12m.

A maximum increase of 15% is observed in the weighted mean stress ratios. The weighted stress standard deviation ratios show a maximum increase of up to 12% compared to the reference case at $z_3 \approx$ -12m. The weighted standard deviation ratios show maximum growths of 10% and 6% at the other depths. The influence of the changes in the mean stresses was studied using the Gerber parabola as a representation of the overall changes in the mean stresses per cycle. It was found that the differences shown in Figure 7-11(a) cause a marginal change in the fatigue lives and therefore their effect was not considered further. The relationship between the fatigue life and the weighted stress standard deviation ratios in the monopile at the three locations are plotted in Figure 7-12. The dashed curve represents the analytical curve for the relationship between the fatigue life and stress ratios shown in Equation (7-2).

Similar to the stress ratios, the fatigue life ratios were normalised with respect to the scenario with no scour as the reference case. A close match between the analytical curve and the results from the time-domain simulations was found. However, a slightly increased deviation is observed between the analytical curve and the points corresponding to the scour depths of 1.25D_{pile} and 1.5D_{pile} at all three locations. This can correspond to the limits for the assumptions made in this study regarding the corresponding negative inverse slope (m) of the section of S-N curve that the majority of damages occurs. Nevertheless, it is clear that the majority of damages in this case still occurs due the stresses corresponding to the section of S-N curve with m=5 and the assumptions are still valid but the slight deviations show the first signs of the limits of this assumption. In addition, the larger change in the first natural frequency at these scour depths can be another source for these deviations.
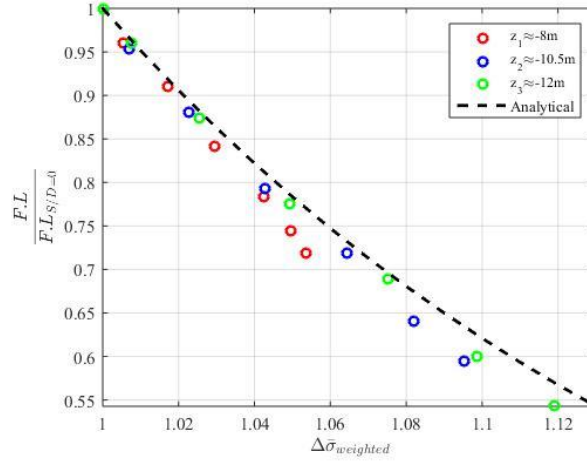
Figure 7-12. Changes in the fatigue life ratio with respect to the standard deviation ratio.

Considering that the variations in the dynamic response appeared to be mainly due to static and quasi-static changes in the response, a set of static analyses was done to verify this assumption and develop an approximate method to calculate fatigue life without the need for the time-domain dynamic simulations at every scour depth. This approximate method aimed to use the time-domain fatigue analysis of the no scour case as a benchmark to predict the fatigue life at different scour depths, using the stress ratios obtained from the static analysis. Figure 7-13 shows a flow diagram of the proposed simplified method for the assessment of scour variation effects on the fatigue life.
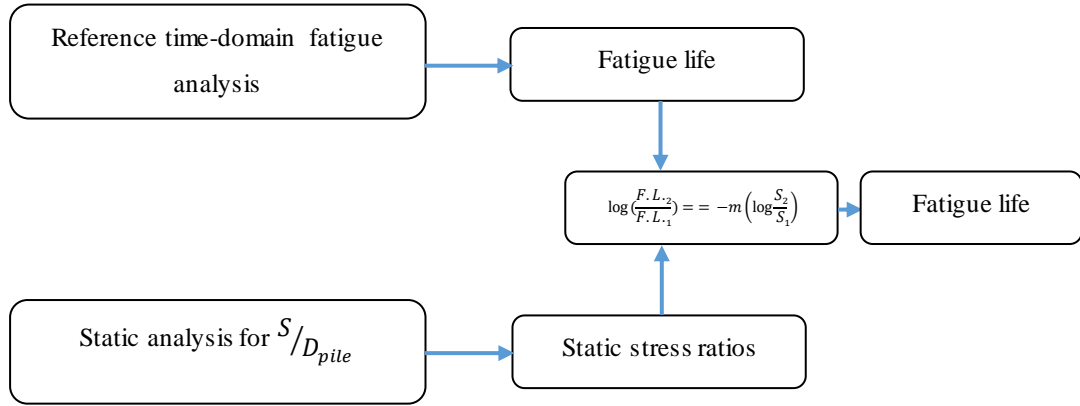
Figure 7-13. Schematic flow chart of the simplified fatigue analysis method to assess scour effects.

For each environmental state, the standard deviations of the wind and wave loads were statically applied to the wind turbine model in ABAQUS. The standard deviations are considered to characterise the variable component of the loads on the structure for each environmental state. Static analysis of these load combinations aims to capture the quasi-static response of the structure as shown in Equation (6-3). The stresses ratios were obtained at the same locations as in the fatigue analysis (i.e. $z_1 \approx$ -8m, $z_2 \approx$ -10.5m, and $z_3 \approx$ -12m). As before, the changes in the stresses,

as a result of scour, were considered in reference to the stresses obtained from the no scour scenario for each environmental state. Similar to the time-domain analysis, the variations in the static stress ratios of all environmental states were combined, using weighted average, to account for their probabilities of occurrence. Figure 7-14 shows the weighted average changes in the static stresses compared to the dynamic stress ratios shown in Figure 7-11(b).
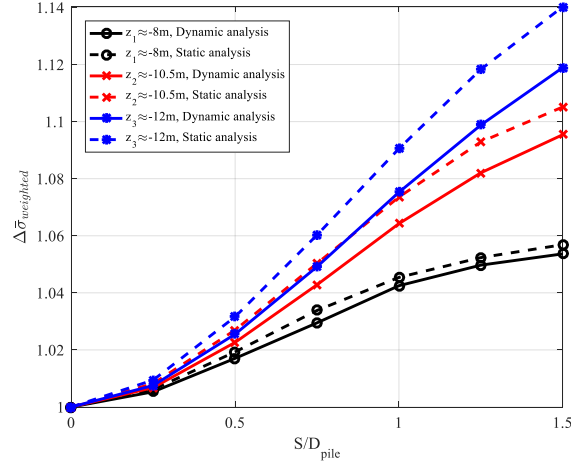
Figure 7-14. Comparison of the weighted average of the static stress ratios with the dynamic ratios for various scour depths at $z_1 \approx$ -8m, $z_2 \approx$ -10.5m, and $z_3 \approx$ -12m.

As can be seen, the two sets of curves follow a similar ascending trend with only a minor difference in the percentage change in the static and dynamic stress ratios. The maximum difference between the standard deviation ratios is less than 2% measured at $z_3 \approx$ -12m. At $z_1 \approx$ -8m, the deviation between static and dynamic stress ratios is less than 1%. The small, but distinct, percentage differences between the static and dynamic stress ratios at higher scour depths can be a result of the fluctuations in the shift in the location of maximum bending moment in the time-domain simulations and the more pronounced role of the dynamic amplification factor, due to higher changes in the natural frequency, at these depths.

With the establishment of the close match between the static and dynamic stress response ratios, the fatigue life of the wind turbine can be predicted from the analytical curve shown in Figure 7-12 for different scour depths. Figure 7-15 compares the calculated fatigue life ratios in the time-domain dynamic simulations with the prediction of the fatigue life ratios from the static analysis of the wind turbine.
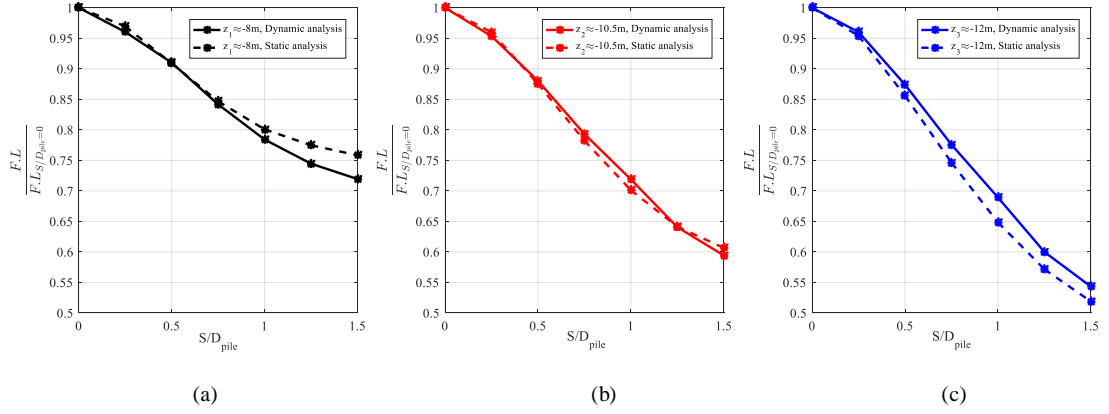
Figure 7-15. Comparison of fatigue life ratios between the dynamic (simulations) and static (analytical) analysis results at (a) $z_1 \approx$ -8m, (b) $z_2 \approx$ -10.5m, and (c) $z_3 \approx$ -12m.

As can be observed, a close match between the complete time-domain fatigue life ratios and those found using the static analysis of the wind turbine is obtained. Fatigue life ratios show a difference of up to 5% between the static and dynamic results. Also, for intermediate scour depths (i.e. up to 1.0D_{pile}), fatigue life ratios calculated at $z_1 \approx$ -8m and $z_2 \approx$ -10.5m show a smaller difference in their results while the highest differences are at $z_3 \approx$-12m. However, it should be noted that the difference between dynamic and static fatigue life ratios tend to grow with the scour depth.

Consideration of scour uncertainties and backfilling process in the fatigue limit state design of offshore wind turbines is a time-consuming task. With the approximate method, the fatigue life could be examined with much less effort, using the fatigue life of the wind turbine at no scour level as the benchmark, and the static analysis of the wind turbine, provided that the dynamic amplification of the support structure's response not be significantly affected by the occurrence of scour (i.e. the modal properties of the wind turbine experience minor changes).

7.5   Summary

In this chapter, a parametric study of the short and long-term influences of scour was performed using the static, modal and time-domain fatigue analyses of the NREL 5MW wind turbine. Modal analysis of the wind turbine support structure for various scour depths showed that the first natural frequency of the wind turbine experiences a lower level of influence from scour compared to the second mode. The change in the first natural frequency due to scour was marginal, especially for intermediate scour levels. The static analysis of the offshore wind turbine showed that occurrence of scour not only increases the bending moment in the monopile by up to 9%, it also shifts the location of the maximum bending moment down. For a maximum scour depth of 1.5D_{pile}, the location of maximum bending moment in monopile moved by approximately 6m. However, the extent of this shift is dependent on the soil profile (especially top soil layers). This phenomenon was found to be an important aspect of scour influence, as the occurrence of scour could have

different effects on a variety of section details (such as welds and bolts) within this relocation range.

Fatigue life at three different locations in the monopile was considered to take this shift in the location of maximum bending moment into account. The fatigue analysis showed that scour influences the fatigue damage in an offshore wind turbine significantly. This study demonstrated that a scour hole of $1.5D_{pile}$ could result in a maximum of 45% reduction in the fatigue life of the wind turbine structure. This amount of change in the fatigue life could lead to an unsafe level for the offshore wind turbine. The considered location for the fatigue life calculation also showed that the lowest location demonstrated the highest rate of change in fatigue life due to scour. In addition, comparison of fatigue damages showed that environmental states with higher fatigue damage contributions tend to be affected by the occurrence of scour slightly more. These findings are in part dependent on the water depth and soil profile used in this research and therefore, extra caution must be taken if higher water depths are considered, where the hydrodynamic loads have a more significant influence on the fatigue damage.

The backfilling of the scour hole can be done naturally or artificially, which could have cost saving effects on the design of offshore wind turbine structures. Here, it was shown that relative material density of the backfilled soil does not have a significant effect on the modal properties or fatigue life of the wind turbine. Therefore, the backfilled depth can be treated as an effective scour depth for simplicity in practice. This could be due to the soft layer at the top of the considered soil profile and the relative density of the backfilled soil could have a higher influence for stiffer top soils. The influence of backfilling period on the fatigue life extension of the wind turbine was also studied by linear interpolation of the fatigue damages. It was shown that backfilling extends the fatigue life differently depending on the backfilled depth and period. However, it generally results in a lower fatigue demand on the structural details, which leads to a more cost-effective design or a considerable extension to the life of the structure. Backfilling of the scour hole to lower scour depths showed a steeper rate of fatigue life extension.

In this study, it was shown that scour mainly influences the response of the system in a quasi-static manner, which leads to the change in the fatigue life of the wind turbine. Thus, a comparison was made between the changes in the fatigue life ratios from the dynamic analysis of the wind turbine in the time-domain against the results from the static analysis of the wind turbine, and a good match was found. Based on this finding, an approximate fatigue analysis method was proposed, which required one time-domain simulation as the reference and used the statically acquired stress ratios to calculate the fatigue life. It was argued that if the changes in the natural frequency of the wind turbine are small, this approach could be applied in practice to save significant computation time in analysing the effect for different scour and backfilling scenarios. In cases where a higher change in the natural frequency is observed, an intermediate scour depth

can be used as reference for the simplified method to ensure the variations in the dynamic amplification of the response as a result of the changes in the natural frequency are kept at a minimum.

8   Conclusions

Offshore wind energy generation has become one of the fastest growing means of providing renewable energy in the world. The support structure is a crucial part of an offshore wind turbine. Monopiles are currently the most commonly used structure type to support offshore wind turbines. Various aspects such as soil-structure interaction, grouted connections, damping and scour can influence the dynamic response of offshore wind turbines, and can potentially change their fatigue life. This thesis presents a comprehensive study of the factors that can influence the fatigue life of monopile-supported offshore wind turbines.

In this research, the NREL 5MW wind turbine was adapted and used as a reference model to carry out comprehensive fatigue analyses. The time-domain fatigue analyses were carried out in different stages, using a combination of different software packages. The wave load was calculated in MATLAB using a relevant wave spectrum. The incoming turbulent wind field was calculated in TurbSim and used as an input in FAST to calculate the wind load. The loads obtained from MATLAB and FAST were used as input for a beam element finite element model of the wind turbine with p-y curves to model soil-structure interaction in ABAQUS. Fatigue life was calculated in MATLAB by rainflow counting the stress signals and using the recommended S-N curve from DNV (2014). In the following, a summary of the findings is presented.

8.1   Soil-structure interaction

The influence of the soil on the short-term response of the wind turbine and its implications for the fatigue life of the structure was studied using the beam and solid (3D) finite element models of the NREL 5MW wind turbine. It was found that the overall stiffness of the offshore wind turbine is significantly influenced by the stiffness of the surrounding soil. The natural frequency of the wind turbine showed a sensitivity of up to 8% to the type of soil (from loose to dense sand soil types), close to the findings by Zaaijer (2006). The stiffness of the wind turbine in the models with p-y curves showed a good match with the elastic soil material definition in the 3D models. However, p-y curves overestimated the stiffness of soil at deeper layers compared to the 3D soil models. Application of p-y curves in the finite element models results in slightly higher stresses in the monopile, which lead to conservative fatigue life estimates. Given the computational costs associated with the 3D finite element models, p-y curves are still the most appropriate method for the fatigue analysis of offshore wind turbines. In practice, reduction of the initial stiffness of p-y springs in cohesionless soil can be used in the beam element models to model the influence of soil material nonlinearities seen in the 3D models.

8.2 Transition piece

The influence of the transition piece on the stiffness of the wind turbine was examined using a solid element model of the Opti-OWECS 3MW wind turbine. The presence of friction at the interface between the grout and steel cylinders in the finite element model proved to be crucial in predicting the mechanics of the transition piece. However, the value of the friction coefficient did not result in a significant change in the overall stiffness of the transition piece. The stiffness of the grouted connection was found to be effectively the same for elastic or nonlinear grout material models. Consideration of the transition piece in the wind turbine assembly revealed that reduction of grout strength or changes in the contact properties between grout and steel, which can occur in the long-term, have a small influence on the first natural frequency and the maximum stress level in the monopile. Therefore, omitting the transition piece damage in studies of fatigue life in the offshore wind turbine monopile yields accurate results.

8.3 Damping

The wind turbine operational regime and damping effects on the fatigue life were examined in the time-domain for a set of environmental states, which comprised more than 90% of the probabilities of occurrence. The influence of damping in limiting fatigue damage in offshore wind turbines was shown to be substantial. Variable damping application, as opposed to constant damping, in the fatigue analysis of offshore wind turbines was shown to reduce the fatigue damage of the environmental states above the rated wind speed, which also had higher damage contributions, and to increase the predicted fatigue life slightly. Nevertheless, as there are uncertainties attached to the damping estimation, the observed small change in fatigue life makes the constant damping assumption acceptable.

It was found that the fatigue damage is driven by a combination of hydrodynamic and aerodynamic loads for an operational wind turbine. For a non-operational turbine, the hydrodynamic loads had a more pronounced effect on the fatigue damage. In the stationary (non-operational) wind turbine, the blade pitch angles had a significant effect on the fatigue damage. Fatigue damage was driven by the wave load when the blades were feathered, while the contribution of aerodynamic loads was visible in the increased damage in the case of pitched-out-blades. Although the wind turbine experiences higher aerodynamic loads in operation, the presence of aerodynamic damping has a more significant influence on limiting the fatigue damage in the wind turbine structure. It is necessary to note that such variations in the fatigue damage in the operational and non-operational scenarios are based on the considered water depth and a more pronounced contribution of the hydrodynamic loads to the fatigue damage is expected in deeper waters. In addition, caution must be taken when applying the conclusions for the non-operational

scenarios considered in this research, as they are limited to the hypothetical prolongation of the fault scenarios.

For an increase of 7% in the overall damping of the system, a reduction of fatigue damage by up to 75% was observed for different environmental states. The predicted fatigue life of offshore wind turbines showed an almost linear increase with the level of damping, from 16 years at 4% overall damping to 53 years at 11% damping. From a practical point of view, supplemental damping (e.g. in the form of tuned mass damper) can extend the fatigue life of the offshore wind turbine substantially. In the case of significantly prolonged breakdown, a higher damage must be anticipated in the wind turbine structure. The reduction in the fatigue life was more substantial when higher damping was present in operational conditions.

A simplified method was proposed for monopile-supported offshore wind turbines in shallow to intermediate water depths, which uses a reference set of time-domain simulations for one damping level and the dynamic amplification of an equivalent single degree of freedom system, to predict the fatigue life for a range of damping levels. The limitations of this method for deeper waters were discussed and should be cautiously considered in practice. This method can be used to significantly reduce the computational costs involved in performing an accurate and well-grounded economic optimisation study of added damping in offshore wind turbines located in shallow to intermediate water depths.

8.4   Scour and backfilling

The influence of scour depths of up to $1.5D_{pile}$ (i.e. 9m) was studied using static, modal and fatigue analyses of the wind turbine. The first and second natural frequencies of the wind turbine showed only small changes. The static results showed that the occurrence of scour around the pile increases the maximum longitudinal stress in the pile by 9% and shifted its location down by up to 6m, as a result of the higher exposed length of the monopile and reduced soil resistance. It should be noted that such deviations in the stress are subject to the soil profile, reference wind turbine and location used and higher variations in the maximum stress can be expected at higher water depths and stiffer soil profiles.

In the time-domain fatigue analysis, the stress in the pile was considered at different depths to investigate the influence of the shift in the location of the maximum stress. Scour depth of $1.5D_{pile}$ caused a reduction of 29% in the fatigue life of the wind turbine at the originally considered point in the pile, while at the critical (lower) location, the fatigue life dropped by up to 45%. Accordingly, it was suggested that the fatigue life variability due to the shift in the location of maximum stress should be considered when designing offshore wind turbines, as it can influence the fatigue damage in the structural details significantly.

Backfilling of the scour hole was studied for different material densities and backfilled depths. Backfilling resulted in the recovery of the natural frequency and bending stresses, which appeared to be to a large degree independent of the backfilled material density. Backfilling with a relative material density of 40% (compared to the original soil) showed an almost complete recovery of the dynamic properties and fatigue life. Linear interpolation of the fatigue life for different natural or artificial backfilling scenarios showed that backfilled depth and period are crucial factors in the extension of the fatigue life in an offshore wind turbine. The effect of backfilling is not typically considered in the design of offshore wind turbines, but it has been proven as an important factor to benefit the operational life of the wind turbine.

The changes caused in the response of the offshore wind turbine were shown to be mainly of static or quasi-static nature, as only small changes in the first natural frequency occurred. The static variations in the longitudinal stress were compared with the variations in the time-domain simulations, using the standard deviation of the stress as proxy for the dynamic variations, and a close match was found. Consequently, it was suggested that if the changes in the natural frequency of the wind turbine are small, the fatigue life could be closely predicted by the static changes of the response. An approximate fatigue analysis method was proposed to predict the fatigue life using the statically acquired stress ratios, which requires a reference time-domain fatigue analysis. The calculated fatigue life ratios from the static analysis showed a good match with the full time-domain simulation results. In practice, this method reduces the computational costs associated with the scour/backfilling design optimisation studies substantially.

9 Future works

In this research, making use of solid element models of the soil and wind turbine was deemed impractical due to the high number of simulations required. A systematic incorporation of the soil nonlinearities, long-term cyclic evolution and damping in the fatigue analysis of the beam element models, which are more appropriate for the fatigue analysis of the wind turbine, is still an outstanding topic. The long-term evolution of the soil stiffness could be incorporated in the fatigue analysis by modifying the lateral resistance of the soil for different periods in their operational life.

The transition piece fatigue was found to be a local rather than a global matter. However, it can affect the serviceability of the wind turbine and fatigue of the tower. Investigation of the influence of damping on limiting fatigue damage in the transition piece can complement the conclusions made in this research.

Despite the higher anticipated damages by considering environmental loads as unidirectional, the study of the influence of directionality on the damage in the side-side direction, where limited aerodynamic damping is present, would be beneficial. From a complete fatigue life analysis, the possible combined benefits of added damping in the fore-aft and side-side directions for such cases could be studied.

Local scour was considered for the analysis of the monopile-supported offshore wind turbines in this research. On the other hand, global scour, which is more likely to occur around other support structure types (e.g. jackets, tripiles, tripods), results in a higher loss of stiffness in the soil, due to the removal of the overburden pressure on the deeper soil layers. This loss of stiffness can result in more significant short and long-term effects than local scour under fatigue load levels. In addition, the relative density of the backfilled material in the analysis of global scour can cause a more pronounced difference in the results.

The approximate methods presented here can be employed for a complete economic assessment of supplemental damping application and scour protection application against backfilling to explore various feasible optimisation solutions.

In addition, as some variations in the results can be expected for considering different reference parameters, it would be beneficial to assess the findings of this research against measureable operational data (if available) and compare the variations in the influence of damping and scour for different reference parameters such as wind turbine dimensions, water depth and soil profile.

References

1. Achmus, M. and Abdel-Rahman, K. (2005) 'Finite element modelling of horizontally loaded monopile foundations for offshore wind energy converters in Germany', in *Frontiers in Offshore Geotechnics*. Perth, Australia: Taylor & Francis, pp. 391–96. doi: 10.1201/NOE0415390637.ch38.

2. Achmus, M., Kuo, Y. S. and Abdel-Rahman, K. (2009) 'Behavior of monopile foundations under cyclic lateral load', *Computers and Geotechnics*, 36(5), pp. 725–735.

3. Adhikari, S. and Bhattacharya, S. (2011) 'Vibrations of wind-turbines considering soil-structure interaction', *Wind and Structures*, 14(2), pp. 85–112.

4. Adhikari, S. and Bhattacharya, S. (2012) 'Dynamic analysis of wind turbine towers on flexible foundations', *Shock and Vibration*, 19(1), pp. 37–56. doi: 10.3233/SAV-2012-0615.

5. Agarwal, P. and Manuel, L. (2008) 'Wave Models for Offshore Wind Turbines', in *Proceedings of 46th AIAA Aerospace Sciences Meeting and Exhibit*. Reston, Virigina: American Institute of Aeronautics and Astronautics, p. 15. doi: 10.2514/6.2008-1336.

6. Alati, N., Nava, V., Failla, G., Arena, F. and Santini, A. (2014) 'On the fatigue behavior of support structures for offshore wind turbines', *Wind and Structures*, 18(2), pp. 117–134. doi: 10.12989/was.2014.18.2.117.

7. Alexander, N. A. and Bhattacharya, S. (2011) 'The dynamics of monopile-supported Wind Turbines in nonlinear soil', in De Roeck, G., Degrande, G., Lombaert, G., and Muller, G. (eds) *Proceedings of the 8th International Conference on Structural Dynamics (EURODYN)*. Leuven, Belgium, pp. 4–6.

8. American Bureau of Shipping (2014) *Spectral-based Fatigue Analysis for Floating Production, Storage and Offloading (FPSO) Installations*. Houston, Texas.

9. American Bureau of Shipping (ABS) (2014) *Guide for the fatigue assessment of offshore structures*. Houston, TX, USA.

10. Andersen, M. S. and Petersen, P. (2004) 'Structural design of grouted connection in offshore steel monopile foundations', in *Proceedings of Global Wndpower*. Chicago,IL, USA: American Wind Energy Association (AWEA).

11. API (American Petroleum Institute) (2007) *Recommended Practice for Planning, Designing and Constructing Fixed Offshore Platforms — Working Stress Design*, *API Recommended Practice*.

12. Arany, L., Bhattacharya, S., Adhikari, S., Hogan, S. J. and Macdonald, J. H. G. (2015) 'An analytical model to predict the natural frequency of offshore wind turbines on three-spring flexible foundations using two different beam models', *Soil Dynamics and*

Earthquake Engineering, 74, pp. 40–45. doi: 10.1016/j.soildyn.2015.03.007.

13. Arany, L., Bhattacharya, S., Macdonald, J. H. G. and Hogan, S. J. (2016) 'Closed form solution of Eigen frequency of monopile supported offshore wind turbines in deeper waters incorporating stiffness of substructure and SSI', *Soil Dynamics and Earthquake Engineering*, 83, pp. 18–32. doi: 10.1016/j.soildyn.2015.12.011.

14. Arany, L., Bhattacharya, S., Macdonald, J. and Hogan, S. J. (2017) 'Design of monopiles for offshore wind turbines in 10 steps', *Soil Dynamics and Earthquake Engineering*, 92(November 2015), pp. 126–152. doi: 10.1016/j.soildyn.2016.09.024.

15. Arneson, L. A., Zevenbergen, L. W., Lagasse, P. F. and Clopper, P. E. (2012) *Evaluating Scour at Bridges, U.S. Department of Transportation, Federal Highway Administration*. Available at: http://www.fhwa.dot.gov/engineering/hydraulics/pubs/hif12003.pdf.

16. Arshad, M. and O'Kelly, B. C. (2015) 'Analysis and Design of Monopile Foundations for Offshore Wind-Turbine Structures', *Marine Georesources & Geotechnology*. Taylor & Francis, 34(6), pp. 503–525. doi: 10.1080/1064119X.2015.1033070.

17. Ashuri, T., Ponnurangam, C., Zhang, J. and Rotea, M. (2016) 'Integrated Layout and Support Structure Optimization for Offshore Wind Farm Design', *Journal of Physics: Conference Series*, 753(September), p. 92011. doi: 10.1088/1742-6596/753/9/092011.

18. ASTM (2011) 'Standard Practices for Cycle Counting in Fatigue Analysis', *ASTM International*, pp. 1–10. doi: 10.1520/E1049-85R11E01.2.

19. Bakmar, C. L. (2009) *Design of Offshore Wind Turbine Support Structures: Selected topics in the field of geotechnical engineering*. Aalborg university.

20. Benitz, M. a., Lackner, M. a. and Schmidt, D. P. (2015) 'Hydrodynamics of offshore structures with specific focus on wind energy applications', *Renewable and Sustainable Energy Reviews*, 44, pp. 692–716. doi: 10.1016/j.rser.2015.01.021.

21. Bhattacharya, S. (2014) 'Challenges in Design of Foundations for Offshore Wind Turbines', *Engineering & Technology Reference*, pp. 1–9. doi: 10.1049/etr.2014.0041.

22. Bhattacharya, S., Cox, J. A., Lombardi, D. and Muir Wood, D. (2013) 'Dynamics of offshore wind turbines supported on two foundations', *Proceedings of the Institution of Civil Engineers - Geotechnical Engineering*, 166(2), pp. 159–169. doi: 10.1680/geng.11.00015.

23. Bhattacharya, S., Lombardi, D. and Muir Wood, D. (2011) 'Similitude relationships for physical modelling of monopile-supported offshore wind turbines', *International Journal of Physical Modelling in Geotechnics*, 11(2), pp. 58–68. doi: 10.1680/ijpmg.2011.11.2.58.

24. Bilgili, M., Yasar, A. and Simsek, E. (2011) 'Offshore wind power development in Europe and its comparison with onshore counterpart', *Renewable and Sustainable Energy Reviews*, 15(2), pp. 905–915. doi: 10.1016/j.rser.2010.11.006.

25. Bisoi, S. and Haldar, S. (2014) 'Dynamic analysis of offshore wind turbine in clay considering soil–monopile–tower interaction', *Soil Dynamics and Earthquake Engineering*. Elsevier, 63, pp. 19–35. doi: 10.1016/j.soildyn.2014.03.006.

26. Blasques, J. P. and Natarajan, A. (2013) 'Mean load effects on the fatigue life of offshore wind turbine monopile foundations', in Brinkmann, B. and Wriggers, P. (eds) *Proceedings of the 5th International Conference on Computational Methods in Marine Engineering, MARINE 2013*. Hamburg, Germany: International Center for Numerical Methods in Engineering (CIMNE), pp. 818–829.

27. Borri, C., Biagini, P. and Marino, E. (2011) 'Large Wind Turbines in Earthquake Areas: Structural Analysis, Design/Construction & In-situ Testing', in Baniotopoulos, C. C., Borri, C., and Stathopoulos, T. (eds) *Environmental Wind Engineering and Design of Wind Energy Structures*. Vienna: Springer Vienna, pp. 295–350. doi: 10.1007/978-3-7091-0953-3.

28. Brennan, F. and Tavares, I. (2014) 'Fatigue design of offshore steel mono-pile wind substructures', *Proceedings of the Institution of Civil Engineers - Energy*, 167(4), pp. 196–202. doi: 10.1680/ener.14.00005.

29. Breusers, H. N. C., Nicollet, G. and Shen, H. W. (1977) 'Local Scour Around Cylindrical Piers', *Journal of Hydraulic Research*, 15(3), pp. 211–252. doi: 10.1080/00221687709499645.

30. Van Buren, E. and Muskulus, M. (2012) 'Improving Pile Foundation Models for use in Bottom-fixed Offshore Wind Turbine Applications', *Energy Procedia*, 24(1876), pp. 363–370. doi: 10.1016/j.egypro.2012.06.119.

31. Burton, T., Sharpe, D., Jenkins, N. and Bossanyi, E. (2001) *Wind Energy Handbook*, *JOHN WILEY & SONS, LTD*. Chichester, UK: John Wiley & Sons, Ltd. doi: 10.1002/0470846062.

32. BVG Associates (2010) *A Guide to an Offshore Wind Farm*, *The Crown Estate*. Available at: http://www.thecrownestate.co.uk/guide_to_offshore_windfarm.pdf.

33. Byrne, B., McAdam, R., Burd, H., Houlsby, G., Martin, C., C, L., Taborda, D., Potts, D., Jardine, R., Sideri, M., Schroeder, F., Gavin, K., Doherty, P., Igoe, D., Wood, A., Kallehave, D. and Gretlund, J. (2015) 'New design methods for large diameter piles under lateral loading for offshore wind applications', in *Third International Symposium on Frontiers in Offshore Geotechnics (ISFOG 2015)*. Oslo, Norway: CRC Press, pp. 705–710. doi: 10.1201/b18442-96.

34. Camp, T., Morris, J., van Rooij, R., Tempel, J. van der, Zaaijer, M. B., Henderson, A., Argyriadis, K., Schwaartz, S., Just, H., Grainger, W. and Pearce, D. (2003) *Design Methods for Offshore Wind Turbines at Exposed Sites*. Delft, Netherlands.

35. Carswell, W. (2012) *probabilitstic analysis of offshore wind turbine soil-structure*

interaction. University of Massachisetts Amherst.

36. Carswell, W., Johansson, J., Løvholt, F., Arwade, S. R., Madshus, C., DeGroot, D. J. and Myers, A. T. (2015) 'Foundation damping and the dynamics of offshore wind turbine monopiles', *Renewable Energy*, 80, pp. 724–736. doi: 10.1016/j.renene.2015.02.058.

37. Chakrabarti, S. K. (2005) *handbook of offshore engineering.* first edit, *Offshore Structure Analysis Inc.* first edit. Plainfield, IL, USA: Elsevier Science Ltd.

38. Collu, M., Brennan, F. P. and Patel, M. H. (2014) 'Conceptual design of a floating support structure for an offshore vertical axis wind turbine: the lessons learnt', *Ships and Offshore Structures*, 9(1), pp. 3–21. doi: 10.1080/17445302.2012.698896.

39. Corbetta, G., Ho, A., Mbistrova, A., Guillet, J. and Pineda, I. (2015) *The European Offshore Wind Industry: Key Trends and Statistics 1st Half 2015.*

40. Cuéllar, P., Mira, P., Pastor, M., Fernández Merodo, J. a., Baeßler, M. and Rücker, W. (2014) 'A numerical model for the transient analysis of offshore foundations under cyclic loading', *Computers and Geotechnics*, 59, pp. 75–86. doi: 10.1016/j.compgeo.2014.02.005.

41. Cui, L. and Bhattacharya, S. (2016) 'Soil–monopile interactions for offshore wind turbines', *Proceedings of the Institution of Civil Engineers - Engineering and Computational Mechanics*, 169(4), pp. 171–182. doi: 10.1680/jencm.16.00006.

42. Dallyn, P., El-Hamalawi, A., Palmeri, A. and Knight, R. (2015) 'Experimental testing of grouted connections for offshore substructures: A critical review', *Structures*, 3, pp. 90–108. doi: 10.1016/j.istruc.2015.03.005.

43. Dallyn, P., El-Hamalawi, A., Palmeri, A. and Knight, R. (2016) 'Experimental investigation on the development of wear in grouted connections for offshore wind turbine generators', *Engineering Structures*, 113, pp. 89–102. doi: 10.1016/j.engstruct.2015.11.028.

44. Damgaard, M., Andersen, L. V. and Ibsen, L. B. (2015) 'Dynamic response sensitivity of an offshore wind turbine for varying subsoil conditions', *Ocean Engineering*, 101, pp. 227–234. doi: 10.1016/j.oceaneng.2015.04.039.

45. Damgaard, M., Andersen, L. V., Ibsen, L. B., Toft, H. S. and Sørensen, J. D. (2015) 'A probabilistic analysis of the dynamic response of monopile foundations: Soil variability and its consequences', *Probabilistic Engineering Mechanics*, 41, pp. 46–59. doi: 10.1016/j.probengmech.2015.05.001.

46. Damgaard, M., Bayat, M., Andersen, L. V. and Ibsen, L. B. (2014) 'Assessment of the dynamic behaviour of saturated soil subjected to cyclic loading from offshore monopile wind turbine foundations', *Computers and Geotechnics*, 61, pp. 116–126. doi: 10.1016/j.compgeo.2014.05.008.

47. Damgaard, M., Ibsen, L. B., Andersen, L. V. and Andersen, J. K. F. (2013) 'Cross-wind

modal properties of offshore wind turbines identified by full scale testing', *Journal of Wind Engineering and Industrial Aerodynamics*, 116, pp. 94–108. doi: 10.1016/j.jweia.2013.03.003.

48. Dassault Systèmes Simulia (2012) 'ABAQUS CAE User's Manual', p. 1174.

49. Dassault Systèmes Simulia Corp. (2012) 'ABAQUS 6.12 user subroutine reference manual'. Providence, pp. 1–591.

50. Dedic, N. (2009) *Analysis of Grouted Connection in Monopile Wind Turbine Foundations Subjected to Horizontal Load Transfer*. Aalborg, East denmark.

51. Deign, J. (2012) *Monopile worries mount Grouted joint doubts linger*, *Wind Energy Update*. Wind Energy Update. Available at: http://social.windenergyupdate.com/turbine-supply-chain/monopile-worries-mount-grouted-joint-doubts-linger (Accessed: 10 April 2012).

52. Depina, I., Hue Le, T. M., Eiksund, G. and Benz, T. (2015) 'Behavior of cyclically loaded monopile foundations for offshore wind turbines in heterogeneous sands', *Computers and Geotechnics*, 65, pp. 266–277. doi: 10.1016/j.compgeo.2014.12.015.

53. Det Norske Veritas (2013) *Design of Offshore Wind Turbine Structures*. Norway.

54. Det Norske Veritas (2014) *Fatigue design of offshore steel structures*. Norway.

55. Devriendt, C., Jordaens, P. J., De Sitter, G. and Guillaume, P. (2012) 'Damping estimation of an offshore wind turbine on a monopile foundation', in *Proceedings of the EWEA 2012 Conference*. Copenhagen, Denmark.

56. Dong, W., Moan, T. and Gao, Z. (2011) 'Long-term fatigue analysis of multi-planar tubular joints for jacket-type offshore wind turbine in time domain', *Engineering Structures*, 33(6), pp. 2002–2014. doi: 10.1016/j.engstruct.2011.02.037.

57. Dong, W., Moan, T. and Gao, Z. (2012) 'Fatigue reliability analysis of the jacket support structure for offshore wind turbine considering the effect of corrosion and inspection', *Reliability Engineering & System Safety*, 106, pp. 11–27. doi: 10.1016/j.ress.2012.06.011.

58. Dou, H. and Byrne, P. M. (1996) 'Dynamic response of single piles and soil-pile interaction', *Canadian Geotechnical Journal*, 33(1), pp. 80–96. doi: 10.1139/t96-025.

59. Downing, S. and Socie, D. (1982) 'Simple rainflow counting algorithms', *International Journal of Fatigue*, 4(1), pp. 31–40. doi: 10.1016/0142-1123(82)90018-4.

60. Drake, K. R. (2017) '[Personal Communication]'. University College London, London.

61. Du, J., Li, H., Zhang, M. and Wang, S. (2015) 'A novel hybrid frequency-time domain method for the fatigue damage assessment of offshore structures', *Ocean Engineering*, 98, pp. 57–65. doi: 10.1016/j.oceaneng.2015.02.004.

62. EAU (1996) *Recommendations of the Committee for Waterfront structures, Harbour and Waterways*. 7th edn. Berlin: Ernst & Sohn.

63. El-Kafafy, M., De Sitter, G., Devriendt, C. and Weijtjens, W. (2014) 'Monitoring resonant frequencies and damping values of an offshore wind turbine in parked conditions', *IET Renewable Power Generation*, 8(4), pp. 433–441. doi: 10.1049/iet-rpg.2013.0229.

64. Esteban, M. D., Diez, J. J., López, J. S. and Negro, V. (2011) 'Why offshore wind energy?', *Renewable Energy*, 36(2), pp. 444–450. doi: 10.1016/j.renene.2010.07.009.

65. Etube, L. S. (1998) *Variable Amplitude Corrosion Fatigue and Fracture Mechanics of Weldable High Strength Jack-Up steels*. University College London.

66. Etube, L. S., Brennan, F. P. and Dover, W. D. (2001) 'Stochastic service load simulation for engineering structures', *Proceedings of the Royal Society A: Mathematical, Physical and Engineering Sciences*, 457(2010), pp. 1469–1483. doi: 10.1098/rspa.2000.0719.

67. Ferguson, M. C. (editor), Kuhn, M., Bussel, G. J. W. van, Bierbooms, W. A. A. M., Cockerill, T. T., Goransson, B., Harland, L. A., Vugts, J. H. and Hes, R. (1998) *A typical design solution for an offshore wind energy conversion*. Delft, The Netherlands.

68. Fontana, C. M., Carswell, W., Arwade, S. R., DeGroot, D. J. and Myers, A. T. (2015) 'Sensitivity of the Dynamic Response of Monopile-Supported Offshore Wind Turbines to Structural and Foundation Damping', *Wind Engineering*, 39(6), pp. 609–628. doi: 10.1260/0309-524X.39.6.609.

69. Gaudiosi, G. (1999) 'Offshore wind energy prospects', *Renewable Energy*, 16(1–4), pp. 828–834. doi: 10.1016/S0960-1481(98)00267-5.

70. Georgiadis, M. (1983) 'Development of p-y curves for layered soils', in *Proceedings of Geotechnical Practice in Offshore Engineering*. New York, USA: Americal Society of Civil Engineers (ASCE), pp. 536–545.

71. Goyal, A. and Chopra, A. K. (1989) 'Simplified Evaluation of Added Hydrodynamic Mass for Intake Towers', *Journal of Engineering Mechanics*, 115(7), pp. 1393–1412. doi: 10.1061/(ASCE)0733-9399(1989)115:7(1393).

72. Guo, Z., Yu, L., Wang, L., Bhattacharya, S., Nikitas, G. and Xing, Y. (2015) 'Model Tests on the Long-Term Dynamic Performance of Offshore Wind Turbines Founded on Monopiles in Sand', *Journal of Offshore Mechanics and Arctic Engineering*, 137(4), p. 41902. doi: 10.1115/1.4030682.

73. Gupta, A. and Singh, R. P. (1986) *Fatigue Behaviour of Offshore Structures*. Edited by C. A. Brebbia and S. A. Orszag. Berlin, Heidelberg: Springer Berlin Heidelberg (Lecture Notes in Engineering). doi: 10.1007/978-3-642-82899-7.

74. Halfpenny, A. (1998) *Dynamic analysis of both on and offshore wind turbines in the frequency domain*. University of London. Available at: http://discovery.ucl.ac.uk/1317858/.

75. Halfpenny, A. (1999) 'A frequency domain approach for fatigue life estimation from

finite element analysis', in *International Conference on Damage Assessment of Structures (DAMAS 99)*. Dublin.

76. Hansen, M. H., Thomsen, K., Fuglsang, P. and Knudsen, T. (2006) 'Two methods for estimating aeroelastic damping of operational wind turbine modes from experiments', *Wind Energy*, 9(1–2), pp. 179–191. doi: 10.1002/we.187.

77. Hasselmann, K., Barnett, T. P., Bouws, E., Carlson, H., Cartwright, D. E., Enke, K., Ewing, J. A., Gienapp, H., Hasselmann, D. E., Kruseman, P., Meerburg, A., Muller, P., Olbers, D. J., Richter, K., Sell, W. and Walden, H. (1973) 'Measurements of Wind-Wave Growth and Swell Decay during the Joint North Sea Wave Project (JONSWAP)', *Ergnzungsheft zur Deutschen Hydrographischen Zeitschrift Reihe*, A(8), pp. 1–95.

78. Henderson, A. R. and Vugts, J. H. (2001) 'Prospects for floating offshore wind energy', in *Proceedings of European Wind Energy Conference (EWEC)*. Copenhagen, Denmark, pp. 627–630.

79. Høgedal, M. and Hald, T. (2005) 'Scour assessment and design for scour for monopile foundations for offshore wind turbines', in *Proceedings of Copenhagen Offshore Wind Conference*. Copenhagen, Denmark.

80. IEC (2005) *Wind Turbines - Part 1: Design requirements*, *International Electromechanical Commission (IEC)*. Geneva, Switzerland. doi: 10.1055/s-2007-985912.

81. IEC (2009) *Wind Turbines - Part 3: Design requirements for offshore wind turbines*, *European Committee for Electrotechnical Standardization*. Brussels, Belgium.

82. International Zinc Association (2011) *Corrosion Protection for Off-Shore Wind Energy Applications*. Available at: http://www.galvinfo.com/Thermal_Spraying/cp_os_wind_apps.html (Accessed: 2 January 2017).

83. Jankowiak, T. and Lodygowski, T. (2005) 'Identification of parameters of concrete damage plasticity constitutive model', *Foundations of Civil and Environmental Engineering*, 6, pp. 53–69.

84. Jensen, M. S., Juul Larsen, B., Frigaard, P., DeVos, L., Christensen, E. D., Asp Hansen, E., Solberg, T., Hjertager, B. H. and Bove, S. (2006) *Offshore Wind Turbines situated in Areas with Strong Currents*. Esbjerg, Denmark.

85. Jonkman, J., Butterfield, S., Musial, W. and Scott, G. (2009) *Definition of a 5-MW reference wind turbine for offshore system development*, *National Renewable Energy Laboratory*. Colorado, USA.

86. Kaldellis, J. K. and Zafirakis, D. (2011) 'The wind energy (r)evolution: A short review of a long history', *Renewable Energy*, 36(7), pp. 1887–1901. doi: 10.1016/j.renene.2011.01.002.

87. Kampitsis, A. E., Giannakos, S., Gerolymos, N. and Sapountzakis, E. J. (2015) 'Soil–pile interaction considering structural yielding: Numerical modeling and experimental validation', *Engineering Structures*. Elsevier Ltd, 99, pp. 319–333. doi: 10.1016/j.engstruct.2015.05.004.

88. Kooijman, H. J., Lindenburg, C., Winkelaar, D. and Hooft, E. . van der (2003) *DOWEC 6 MW PRE-DESIGN, Aeroelastic modelling of the DOWEC 6 MW pre-design in PHATAS*. The Netherlands.

89. Koukoura, C., Brown, C., Natarajan, A. and Vesth, A. (2016) 'Cross-wind fatigue analysis of a full scale offshore wind turbine in the case of wind–wave misalignment', *Engineering Structures*, 120, pp. 147–157. doi: 10.1016/j.engstruct.2016.04.027.

90. Koukoura, C., Natarajan, A. and Vesth, A. (2015) 'Identification of support structure damping of a full scale offshore wind turbine in normal operation', *Renewable Energy*, 81, pp. 882–895. doi: 10.1016/j.renene.2015.03.079.

91. Kuo, Y., Achmus, M. and Abdel-rahman, K. (2012) 'Minimum Embedded Length of Cyclic Horizontally Loaded Monopiles', *Journal of Geotechnical and Geoenvironmental Engineering*, (March), pp. 357–363. doi: 10.1061/(ASCE)GT.1943-5606.0000602.

92. Kurian, V. and Ganapathy, C. (2010) 'Monopile Foundations for Offshore Wind Turbines', in *Proceedings of International Conference on Sustainable Building and Infrastructure, ICSBI*. Kuala Lumpur, Malaysia.

93. Lee, Y.-S., Choi, B.-L., Lee, J. H., Kim, S. Y. and Han, S. (2014) 'Reliability-based design optimization of monopile transition piece for offshore wind turbine system', *Renewable Energy*, 71, pp. 729–741. doi: 10.1016/j.renene.2014.06.017.

94. Lindenburg, C. (2002) *Aeroelastic Modelling of the LMH64-5 Blade*. The Netherlands.

95. Lombardi, D., Bhattacharya, S. and Muir Wood, D. (2013) 'Dynamic soil–structure interaction of monopile supported wind turbines in cohesive soil', *Soil Dynamics and Earthquake Engineering*, 49, pp. 165–180. doi: 10.1016/j.soildyn.2013.01.015.

96. Lotsberg, I. (2013) 'Structural mechanics for design of grouted connections in monopile wind turbine structures', *Marine Structures*, 32, pp. 113–135. doi: 10.1016/j.marstruc.2013.03.001.

97. Lotsberg, I., Serednicki, A., Lervik, A. and Bertnes, H. (2012) 'Design of grouted connections for monopile offshore structures', *Stahlbau*, 81(9), pp. 695–704. doi: 10.1002/stab.201201598.

98. Low, Y. M. (2011) 'Extending a time/frequency domain hybrid method for riser fatigue analysis', *Applied Ocean Research*, 33(2), pp. 79–87. doi: 10.1016/j.apor.2011.02.003.

99. Lozano-Minguez, E., Kolios, A. J. and Brennan, F. P. (2011) 'Multi-criteria assessment of offshore wind turbine support structures', *Renewable Energy*. Elsevier Ltd, 36(11), pp. 2831–2837. doi: 10.1016/j.renene.2011.04.020.

100. Malhotra, S. (2010) 'Supporting the Winds of Change', *Civil Engineering Magazine Archive*, 80(8), pp. 76–94. doi: 10.1061/ciegag.0000307.

101. Marino, E., Giusti, A. and Manuel, L. (2017) 'Offshore wind turbine fatigue loads: The influence of alternative wave modeling for different turbulent and mean winds', *Renewable Energy*, 102, pp. 157–169. doi: 10.1016/j.renene.2016.10.023.

102. Marino, E., Lugni, C. and Borri, C. (2013) 'The role of the nonlinear wave kinematics on the global responses of an OWT in parked and operating conditions', *Journal of Wind Engineering and Industrial Aerodynamics*. Elsevier, (ii), pp. 1–14. doi: 10.1016/j.jweia.2013.09.003.

103. Matsuishi, M. and Endo, T. (1968) 'Fatigue of metals subjected to varying stress', *Proceedings of Kyushu Branch of Japan Society of Mechanical Engineers*. Fukuoka, Japan, pp. 37–40.

104. Matutano, C., Negro, V., López-Gutiérrez, J.-S. and Esteban, M. D. (2013) 'Scour prediction and scour protections in offshore wind farms', *Renewable Energy*, 57, pp. 358–365. doi: 10.1016/j.renene.2013.01.048.

105. Michalopoulos, V. (2015) *Simplified fatigue assessment of offshore wind support structures accounting for variations in a farm*. Delft University of Technology.

106. Michalopoulos, V. and Zaaijer, M. B. (2015) 'Simplified Fatigue Assessment of Offshore Wind Support Structures Accounting for Variations in a Farm', in *Proceedings of European Wind Energy Association (EWEC) Conference*. Paris, France, pp. 1–9.

107. Mohammadi, S. F., Galgoul, N. S., Starossek, U. and Videiro, P. M. (2016) 'An efficient time domain fatigue analysis and its comparison to spectral fatigue assessment for an offshore jacket structure', *Marine Structures*, 49, pp. 97–115. doi: 10.1016/j.marstruc.2016.05.003.

108. Moriarty, P. J. and Hansen, a C. (2005) *AeroDyn Theory Manual*, *Renewable Energy*. Golden, Colorado, USA. doi: 10.1146/annurev.fl.15.010183.001255.

109. Mostafa, Y. E. (2012) 'Effect of Local and Global Scour on Lateral Response of Single Piles in Different Soil Conditions', *Engineering*, 4(6), pp. 297–306. doi: 10.4236/eng.2012.46039.

110. Murchison, J. M. and O'Neill, M. W. (1983) *An evaluation of p-y relationships in sands*. University of Houston.

111. Murchison, J. M. and O'Neill, M. W. (1984) 'Evaluation of p-y relationships in cohesionless soils, analysis and design of pile foundations.', in *Proceedings of the Symposium in Conjunction with the ASCE National Convention*. ASCE, pp. 174–191.

112. Musial, W., Butterfield, S. and Boone, A. (2004) 'Feasibility of Floating Platform Systems for Wind Turbines', in *Proceedings of 23rd ASME Wind energy Symposiumnergy Symposium*, pp. 476–486.

113. El Naggar, M. H. and Novak, M. (1995) 'Nonlinear lateral interaction in pile dynamics', *Soil Dynamics and Earthquake Engineering*, 14(2), pp. 141–157. doi: 10.1016/0267-7261(94)00028-F.

114. Nehal, R. S. (2001) *Foundation Design Monopile 3.6 & 6.0 MW wind turbines*. Amstelveen, The Netherlands.

115. Niesłony, A. (2009) 'Determination of fragments of multiaxial service loading strongly influencing the fatigue of machine components', *Mechanical Systems and Signal Processing*, 23(8), pp. 2712–2721. doi: 10.1016/j.ymssp.2009.05.010.

116. Nikitas, G., Arany, L., Aingaran, S., Vimalan, J. and Bhattacharya, S. (2017) 'Predicting long term performance of offshore wind turbines using cyclic simple shear apparatus', *Soil Dynamics and Earthquake Engineering*, 92(September 2016), pp. 678–683. doi: 10.1016/j.soildyn.2016.09.010.

117. NREL (2015) *NWTC Information Portal (FAST)*, *NREL*. Available at: https://nwtc.nrel.gov/FAST (Accessed: 25 March 2016).

118. NREL (2016) *NWTC Information Portal (TurbSim)*, *NREL*. Available at: https://nwtc.nrel.gov/TurbSim (Accessed: 25 March 2016).

119. Pappusetty, D. and Pando, M. A. (2014) 'Finite Element Analyses of Offshore Monopile Deflection Accumulation under Harmonic Loading', in *Proceedings of the Soil Behavior Fundamentals to Innovations in Geotechnical Engineering*. Reston, VA, pp. 585–596. doi: 10.1061/9780784413265.047.

120. Pedersen, R. and Jørgensen, M. (2012) 'Grouted Connections with Shear Keys: Numerical modelling with ABAQUS', *Proceedings of the 25TH Nordic Seminar on Computational Mechanics*, (October).

121. Petersen, B., Pollack, M., Connell, B., Greeley, D., Davis, D., Slavik, C. and Goldman, B. (2010) *Evaluate the Effect of Turbine Period of Vibration Requirements on Structural Design Parameters: Technical Report of Findings*. Groton, CT, USA.

122. Petersen, T. U., Mutlu Sumer, B., Fredsøe, J., Raaijmakers, T. C. and Schouten, J.-J. (2015) 'Edge scour at scour protections around piles in the marine environment — Laboratory and field investigation', *Coastal Engineering*, 106, pp. 42–72. doi: 10.1016/j.coastaleng.2015.08.007.

123. Pierson, W. J. and Moskowitz, L. (1964) 'A proposed spectral form for fully developed wind seas based on the similarity theory of S. A. Kitaigorodskii', *Journal of Geophysical Research*, 69(24), pp. 5181–5190. doi: 10.1029/JZ069i024p05181.

124. Prakhya, G., Zhang, C. and Harding, N. (2012) 'Grouted connections for monopiles – limits for large wind turbines', *The Structural Engineer*, 90(3), pp. 30–45.

125. Prendergast, L. J., Gavin, K. and Doherty, P. (2015) 'An investigation into the effect of scour on the natural frequency of an offshore wind turbine', *Ocean Engineering*, 101, pp.

1–11. doi: 10.1016/j.oceaneng.2015.04.017.

126. Prendergast, L. J., Hester, D., Gavin, K. and O'Sullivan, J. J. (2013) 'An investigation of the changes in the natural frequency of a pile affected by scour', *Journal of Sound and Vibration*, 332(25), pp. 6685–6702. doi: 10.1016/j.jsv.2013.08.020.

127. Reese, L. C., Cox, W. R. and Koop, F. D. (1974) 'Analysis of Laterally Loaded Piles in Sand', in *Proceedings of Offshore Technology Conference*. Houston, TX, USA: Offshore Technology Conference, pp. 473–480. doi: 10.4043/2080-MS.

128. Reese, L. C., Cox, W. R. and Koop, F. D. (1975) 'Field Testing and Analysis of Laterally Loaded Piles in Stiff Clay', in *Proceedings of Offshore Technology Conference*. Houston, TX, USA: Offshore Technology Conference, pp. 671–690. doi: 10.4043/2312-MS.

129. Rezaei, R., Fromme, P. and Duffour, P. (2017) 'Fatigue Life Sensitivity of Monopile-Supported Offshore Wind Turbines to Damping', *Submitted to Renewable Energy*, pp. 1–25.

130. Saleem, Z. (2011) *Alternatives and modifications of Monopile foundation or its installation technique for noise mitigation*. Delft, Netherlands.

131. Salzmann, D. J. C. and Tempel, J. van der (2005) 'Aerodynamic damping in the design of support structures for offshore wind turbines', in *Proceedings of the Offshore Wind Energy Conference*. Copenhagen, Denmark, pp. 1–9.

132. Schafhirt, S., Page, A., Eiksund, G. R. and Muskulus, M. (2016) 'Influence of Soil Parameters on the Fatigue Lifetime of Offshore Wind Turbines with Monopile Support Structure', *Energy Procedia*, 94(January), pp. 347–356. doi: 10.1016/j.egypro.2016.09.194.

133. Schaumann, P. and Böker, C. (2005) 'Can jackets and tripods compete with monopiles', in *Contribution to Copenhagen Offshore Wind*. Copenhagen, Denmark, pp. 26–28.

134. Schaumann, P., Böker, C., Bechtel, A. and Lochte-Holtgreven, S. (2011) 'Support Structures of Wind Energy Converters', in Baniotopoulos, C. C., Borri, C., and Stathopoulos, T. (eds) *Environmental Wind Engineering and Design of Wind Energy Structures*. Vienna: Springer Vienna, pp. 191–253. doi: 10.1007/978-3-7091-0953-3.

135. Schaumann, P., Lochte-Holtgreven, S. and Steppeler, S. (2011) 'Special fatigue aspects in support structures of offshore wind turbines', *Materialwissenschaft und Werkstofftechnik*, 42(12), pp. 1075–1081. doi: 10.1002/mawe.201100913.

136. Schaumann, P., Wilke, F. and Lochte-Holtgreven, S. (2008) 'Nonlinear structural dynamics of offshore wind energy converters with grouted transition piece', in *Proceedings of European Wind Energy Conference (EWEC)*. Brussels, Belgium.

137. Schijve, J. (2009) 'Fatigue Properties', in *Fatigue of Structures and Materials*. Dordrecht: Springer Netherlands, pp. 141–169. doi: 10.1007/978-1-4020-6808-9_6.

138. Seidel, M. (2014) 'Substructures for offshore wind turbines - Current trends and developments', in *Festschrift Peter Schaumann*. Hannover, Germany, pp. 363–368. doi: 10.2314/GBV:77999762X.

139. Shadlou, M. and Bhattacharya, S. (2016) 'Dynamic stiffness of monopiles supporting offshore wind turbine generators', *Soil Dynamics and Earthquake Engineering*, 88, pp. 15–32. doi: 10.1016/j.soildyn.2016.04.002.

140. Sheng, J. and Chen, S. (2010) 'Fatigue load simulation for foundation design of offshore wind turbines due to combined wind and wave loading', in *Proceediings of 2010 World Non-Grid-Connected Wind Power and Energy Conference*. Nanjing, China: IEEE, pp. 1–6. doi: 10.1109/WNWEC.2010.5673107.

141. Sheppard, R. and Puskar, F. (2011) 'Inspection Guidance for Offshore Wind Turbine Facilities', in *Proceedings of Offshore Technology Conference*. Houston, TX, USA, pp. 1–10.

142. Shirzadeh, R., Devriendt, C., Bidakhvidi, M. a. and Guillaume, P. (2013) 'Experimental and computational damping estimation of an offshore wind turbine on a monopile foundation', *Journal of Wind Engineering and Industrial Aerodynamics*, 120, pp. 96–106. doi: 10.1016/j.jweia.2013.07.004.

143. Shirzadeh, R., Weijtjens, W., Guillaume, P. and Devriendt, C. (2015) 'The dynamics of an offshore wind turbine in parked conditions: a comparison between simulations and measurements', *Wind Energy*, 18(10), pp. 1685–1702. doi: 10.1002/we.1781.

144. Sørensen, S., Ibsen, L. and Frigaard, P. (2010) 'Experimental evaluation of backfill in scour holes around offshore monopiles', in *Frontiers in Offshore Geotechnics II*. CRC Press, pp. 617–622. doi: 10.1201/b10132-84.

145. Sørensen, S. P. H. and Ibsen, L. B. (2013) 'Assessment of foundation design for offshore monopiles unprotected against scour', *Ocean Engineering*, 63, pp. 17–25. doi: 10.1016/j.oceaneng.2013.01.016.

146. Stancich, R. (2011) *Monopile retrofits and designs going forward Room for grout Wind Energy Update*, *wind energy update*. Available at: http://social.windenergyupdate.com/offshore/monopile-retrofits-and-designs-going-forward-room-grout.

147. Stieng, L. E. S., Hetland, R., Schafhirt, S. and Muskulus, M. (2015) 'Relative Assessment of Fatigue Loads for Offshore Wind Turbine Support Structures', *Energy Procedia*, 80(1876), pp. 229–236. doi: 10.1016/j.egypro.2015.11.426.

148. Sumer, B. and Fredsøe, J. (2002) *The Mechanics of Scour in the Marine Environment*, *World scientific*. Edited by P. Liu. Singapore: World Scientific Publishing Co. Pte. Ltd.

149. Sumer, B. M., Fredsoe, J. and Christiansen, N. (1992) 'Scour around Vertical Pile in Waves', *Journal of Waterway Port Coastal and Ocean Engineeringharvard*, 118(1), pp.

15–31.

150. Sun, X., Huang, D. and Wu, G. (2012) 'The current state of offshore wind energy technology development', *Energy*, 41(1), pp. 298–312. doi: 10.1016/j.energy.2012.02.054.

151. Tarp-Johansen, N. J., Andersen, L., Christensen, E., Mørch, C., Kallesøe, B. and Frandsen, S. (2009) 'Comparing Sources of Damping of Cross-Wind Motion', in *Proceedings of European Offshore Wind 2009 : Conference & Exhibition*. Stockholm, Sweden: The European Wind Energy Association, pp. 1–10.

152. Tempel, J. van der (2006) *Design of support structure for offshore wind turbines*. Delft University of Technology.

153. Tempel, J. van der and Molenaar, D. (2002) 'Wind Turbine Structural Dynamics - A Review of the Principles for Modern Power Generation, Onshore and Offshore', *Wind Engineering*, 26(4), pp. 211–222. doi: 10.1260/030952402321039412.

154. Tempel, J. van der, Zaaijer, M. and Subroto, H. (2004) 'The effects of Scour on the design of Offshore Wind Turbines', in *Proceedings of the 3rd International Conference on Marine Renewable Energy*. Blyth, UK, pp. 53–62.

155. Valamanesh, V. and Myers, A. T. (2014) 'Aerodynamic Damping and Seismic Response of Horizontal Axis Wind Turbine Towers', *Journal of Structural Engineering*, 140(11), p. 4014090. doi: 10.1061/(ASCE)ST.1943-541X.0001018.

156. Veldkamp, H. F. and Tempel, J. van der (2005) 'Influence of wave modelling on the prediction of fatigue for offshore wind turbines', *Wind Energy*, 8(1), pp. 49–65. doi: 10.1002/we.138.

157. Versteijlen, W., Metrikine, A., Hoving, J. S., Smidt, E. and De Vries, W. E. (2011) 'Estimation of the vibration decrement of an offshore wind turbine support structure caused by its interaction with soil', in *Proceedings of the EWEA Offshore 2011 Conference*. Amsterdam, The Netherlands: European Wind Energy Association.

158. Waveclimate.com (2016) *Offshore Location*. Available at: http://www.waveclimate.com (Accessed: 11 April 2016).

159. Weinert, J., Smolka, U., Schümann, B. and Cheng, P. W. (2015) 'Detecting Critical Scour Developments at Monopile Foundations Under Operating Conditions', in *Proceedings of the European Wind Energy Association Annual Event, EWEA 2015*. Paris, France, pp. 135–139.

160. Whitehouse, R. J. S. (1998) *Scour at marine structures - A manual for practical application*. London: Thomas Telford publications.

161. Whitehouse, R. J. S., Harris, J. M., Sutherland, J. and Rees, J. (2011) 'The nature of scour development and scour protection at offshore windfarm foundations', *Marine Pollution Bulletin*, 62(1), pp. 73–88. doi: 10.1016/j.marpolbul.2010.09.007.

162. Yeter, B., Garbatov, Y. and Guedes Soares, C. (2016) 'Evaluation of fatigue damage model predictions for fixed offshore wind turbine support structures', *International Journal of Fatigue*, 87, pp. 71–80. doi: 10.1016/j.ijfatigue.2016.01.007.

163. Zaaijer, M. (2002) *Tripod support structure-pre-design and natural frequency assessment for the 6 MW DOWEC*, *TU Delft, DOWEC*. Delft, Netherlands.

164. Zaaijer, M. (2005) *Design methods for offshore wind turbines at exposed sites (OWTES)-Sensitivity analysis for foundations of offshore wind turbines*, *Section wind energy, WE*. Delft, The Netherlands.

165. Zaaijer, M. (2006) 'Foundation modelling to assess dynamic behaviour of offshore wind turbines', *Applied Ocean Research*, 28(1), pp. 45–57. doi: 10.1016/j.apor.2006.03.004.

166. Zaaijer, M. and Tempel, J. van der (2004) 'Scour protection: a necessity or a waste of money?', in *Proceedings of the 43 IEA Topixal Expert Meeting*. Skaerbaek, Denmark, pp. 43–51.

167. Zdravković, L., Taborda, D., Potts, D., Jardine, R., Sideri, M., Schroeder, F., Byrne, B., McAdam, R., Burd, H., Houlsby, G., Martin, C., Gavin, K., Doherty, P., Igoe, D., Wood, A., Kallehave, D. and Gretlund, J. (2015) 'Numerical modelling of large diameter piles under lateral loading for offshore wind applications', in *Proceedings of 3rd International Symposium on Frontiers in Offshore Geotechnics (ISFOG 2015)*. Oslo, Norway: CRC Press, pp. 759–764. doi: 10.1201/b18442-105.

168. Ziegler, L., Schafhirt, S., Scheu, M. and Muskulus, M. (2016) 'Effect of Load Sequence and Weather Seasonality on Fatigue Crack Growth for Monopile-based Offshore Wind Turbines', *Energy Procedia*, 94(January), pp. 115–123. doi: 10.1016/j.egypro.2016.09.204.

169. Ziegler, L., Voormeeren, S., Schafhirt, S. and Muskulus, M. (2015) 'Sensitivity of Wave Fatigue Loads on Offshore Wind Turbines under Varying Site Conditions', *Energy Procedia*, 80(17–18), pp. 193–200. doi: 10.1016/j.egypro.2015.11.422.

Appendix-A: P-y curves

According to DNV (2013), p-y relationship for a vertical pile in cohesionless soil is found from Equations (A-1) and (A-2). In these Equations the parameters A, k, γ', and D_{pile} are factors for the static or cyclic loading, modulus of subgrade reaction, submerged unit weight of soil and pile diameter, respectively.

$$p = A p_u \tanh\left(\frac{kX}{A p_u} y\right).$$
(A-1)

The ultimate static lateral resistance, p_u, is defined as:

$$p_u = \begin{cases} (C_1 X + C_2 D)\gamma' X & for\ 0 < X \le X_R, \\ C_3 D \gamma' X & for\ X > X_R \end{cases},$$
(A-2)

where, C_1, C_2, and C_3 depend on the friction angle of the soil. X is the depth below the surface, and X_R is the depth below the value of $(C_1 X + C_2 D)\gamma' X$ exceeds $C_3 D\gamma' X$.

According to DNV (2013), p-y relationship for vertical piles in cohesive soil under cyclic loading is found from Equations (A-3), (A-4) and (A-5).

$$for\ X > X_R \qquad p = \begin{cases} \dfrac{p_u}{2}\left(\dfrac{y}{y_c}\right)^{\frac{1}{3}} & for\ y \le 3y_c \\ 0.72 p_u & for\ y > 3y_c \end{cases}.$$
(A-3)

$$for\ X \le X_R \qquad p = \begin{cases} \dfrac{p_u}{2}\left(\dfrac{y}{y_c}\right)^{\frac{1}{3}} & for\ y \le 3y_c \\ 0.72 p_u \left(1 - \left(1 - \dfrac{X}{X_R}\right)\dfrac{y - 3y_c}{12 y_c}\right) & for\ 3y_c < y \le 15 y_c \\ 0.72 p_u \left(\dfrac{X}{X_R}\right) & for\ y > 15 y_c \end{cases}.$$
(A-4)

The static ultimate lateral resistance is calculated as:

$$p_u = \begin{cases} (3 s_u + \gamma' X)D + J s_u X & for\ 0 < X \le X_R, \\ 9 s_u D & for\ X > X_R \end{cases},$$
(A-5)

where, s_u is the undrained shear strength of the soil, γ' is the effective unit weight of the soil and J is a dimensionless empirical constant ranging between 0.25 and 0.5. In addition, X refers to the depth below the seabed, D_{pile} is the pile diameter and $y_c = 2.5\varepsilon_c D$ in which ε_c corresponds to the one-half maximum stress in laboratory undrained compression tests of undisturbed soil samples.

X_R is the depth below which the first component of static ultimate lateral resistance exceeds the second component.

Appendix-B: Verification of the fatigue analysis

A variable amplitude harmonic stress signal was considered to verify the fatigue damage calculation method. Figure B-1 shows the stress signal used. As can be seen, the stress signal comprises of three sub-records of 30MPa, 15MPa and 10MPa amplitudes, which all have the same frequency of 0.25Hz. The length of each sub-record is 100s, resulting in a 300s signal in total.
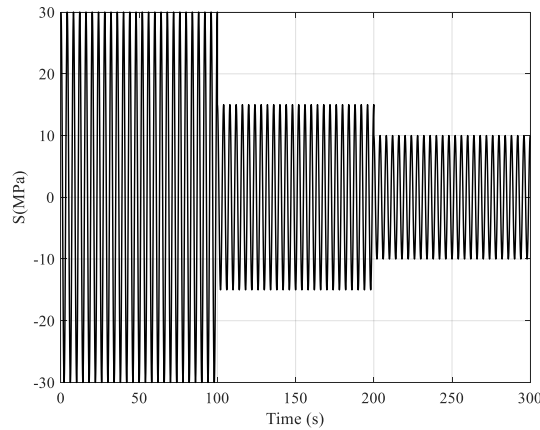

Figure B-1. Variable amplitude harmonic stress signal used for the verification of the fatigue analysis methodology.

The first step in the fatigue analysis is defining the S-N curve. As mentioned before, S-N curve for structural detail class E was used. The parameters used for the definition of this S-N curve are presented in Table B-1, and the resultant S-N curve is shown in Figure B-2.

Table B-1. S-N curve parameters for structural detail class E, according to DNV (2014).

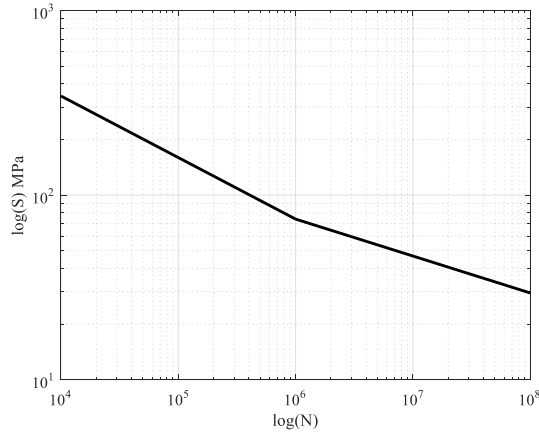| $N \leq 10^6$		$N \geq 10^6$		Thickness component	Hotspot consideration
$Log(\bar{a}_1)$	m_1	$Log(\bar{a}_2)$	m_2	k	SCF
11.61	3.0	15.35	5.0	0.2	1.13

Figure B-2. S-N curve for structural design class E.

Rainflow counting the signal was performed in MATLAB. The process comprised of cycle rate determination and rainflow counting of the cycle rates. At the first step, the turning points of the signal were detected. The amplitude, mean and cycle rate of the detected local extremes (from the turning points) were then calculated using a rainflow counting script. Figure B-3(a) shows the detected turning points in the signals, while Figure B-3(b) shows the histogram of the rainflow counted cycle amplitudes.

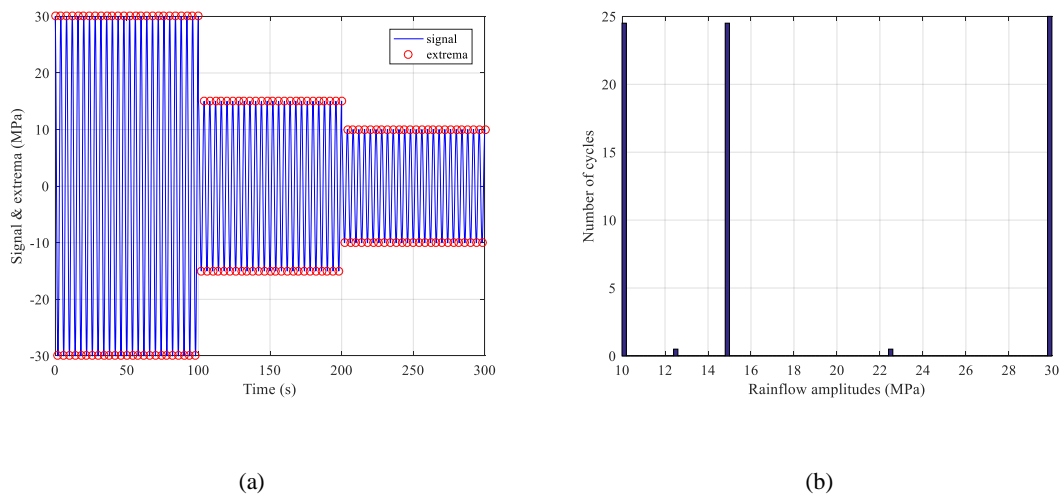

(a)   (b)

Figure B-3. (a) Detected turning points in the stress signal and (b) histogram of the rainflow counted stress signal amplitudes using the detected local extrema.

Figure B-3(a) shows that the local extrema script captures all the turning point in the signal perfectly. Note that in (b), the stresses amplitudes are plotted. The stress range for fatigue damage calculations were found by multiplying these amplitudes by two. In Figure B-3(b), in addition to the number of cycles counted for each stress amplitude, two half-cycles can be seen, whose amplitude is between each two consecutive stress amplitudes. These half cycles are caused by the transition between a higher stress cycle to the lower stress cycle, which only occurs twice in the used signal (i.e. at 100s and at 200s). At these transition points, the stress cycle is slightly

increased than the subsequent stress amplitude. For example, at 100s, the stress signal is reduced from cycles of 30MPa amplitude to cycles of 15MPa amplitude, resulting in one half-cycle of 22.5MPa amplitude. A similar scenario occurs at 200s.

Once the stress signal was rainflow counted, the fatigue resistance (N) for each stress cycle was found using a MATLAB script. Subsequently, the damage in the pile was calculated by summing the ratios of the stress cycles and cycles to failure. The fatigue damage by this signal was found to be 9×10^{-6}, resulting in a fatigue life of approximately 1 year.

Knowing the number of cycles and the stress amplitudes, the analytically calculated fatigue damage was compared with the fatigue damage from the MATLAB scripts and a match was found.

Appendix-C: Influence of wave diffraction on the fatigue damage

The influence of the diffraction effects on the wave loading, which was shown to over-estimate the hydrodynamic loads (by assuming constant inertia coefficient C_m=2.0, section 3.5.2) for environmental states with lower wave lengths, was discussed in Chapter 6. In this section, a detailed comparison of the fatigue damage contribution of different environmental states for the models with and without the diffraction effects are presented. The wind turbine was considered to be in operation and a representative total damping of 6% was considered for the models in this analysis. The wind loading per environmental state is identical in both models while the wave loading is different (i.e. with and without diffraction effects as shown in Table 3-6). Figure C-1(a) shows the normalised fatigue damage per environmental state and Figure C-1(b) shows the normalised contribution of the environmental states' damages for the two models.
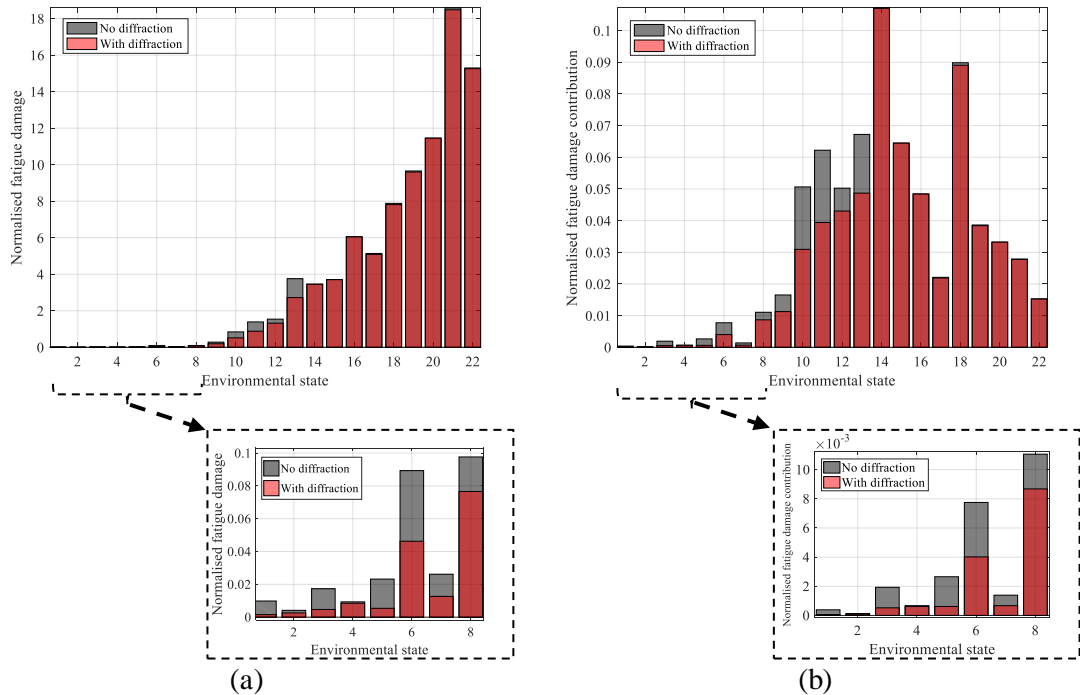

Figure C-1. (a) Normalised damage and (b) normalised contribution of environmental states' damages compared for the two models with and without diffraction effects considered for wave loading. The fatigue damage of environmental states 1-8 are magnified to the bottom of both figures.

Figure C-1(a) shows the largest difference in the damage of the environmental states corresponds to the environmental states 1-13. The damage contributions of environmental states 1-8 are low compared to the higher environmental states, which is in agreement with the results shown in Table 1. However, a significantly larger reduction in damage (by 50%) is observed for these environmental states. Figure C-1(b) shows that environmental states 1-8 do not cause a considerable change in the fatigue damage due to their low contribution. However, the intermediate environmental states (i.e. environmental states 10-13) show a more significant

reduction in the fatigue damage. The fatigue life of the wind turbine without diffraction effects (i.e. constant inertia coefficient C_m=2.0) is approximately 28 years while consideration of the diffraction effects in the wave loading increases the fatigue life to 31 years. This results in a 10% over-conservatism in the calculation of fatigue damage.

Appendix-D: Dynamics of offshore wind turbines in deeper water

In this section, a wind turbine with only wave loads applied is considered to explore the limitations of the simplified method for wind turbines in deeper waters. Following Drake (2017), the wind turbine is represented by a lumped mass model as shown in Figure D-1.
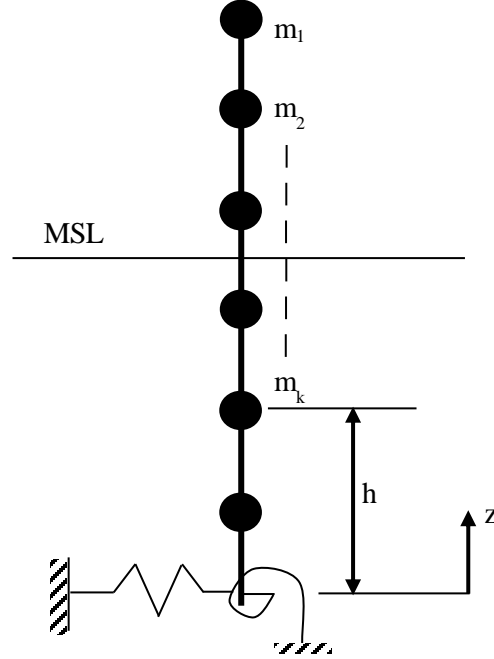

Figure D-1. Simplified multi degree of freedom schematic of an offshore wind turbine structure.

The dynamic shear and bending moment at a given section of a lightly damped offshore tower with only the wave loads considered in deep waters are governed by the combination of wave forces and inertial forces. For the structural representation shown in Figure D-1, the dynamic moment can be expressed as:

$$DM(h, \omega_i) = M(h, \omega_i) + \sum_{k=1}^{K} m_k(z_k - h)\omega_i^2 \underline{x_k}(\omega_i), \qquad \text{(D-1)}$$

where DM is the dynamic moment, M is the wave moment at location k, ω_i is the frequency of the ith Fourier component and $\underline{x_k}(\omega_i)$ is the Fourier component of horizontal displacement at location k.

Assuming that the displacements can be well represented by the response of the first mode, the horizontal component of the displacement can be presented as shown in Equation (D-2).

$$\underline{x}_k(\omega_i) = \phi_1(z_k)\underline{n}_1(\omega_i), \tag{D-2}$$

where $\phi_1(z_k)$ is the mode shape magnitude at location k and $\underline{n}_1(\omega_i)$ is the modal response, which is defined in Equation (D-3).

$$\underline{n}_1(\omega_i) = \frac{F_1^*(\omega_i)}{\omega_1^2 M_1^*} \cdot \frac{1}{\left(1 - \left(\frac{\omega_i}{\omega_1}\right)^2\right) + 2j\zeta_1\left(\frac{\omega_i}{\omega_1}\right)}, \tag{D-3}$$

where $F_1^*(\omega_i)$ is the Fourier component of generalised wave force in the first mode, M_1^* is the generalised mass in the first mode, ω_1 is the first mode natural frequency, ζ_1 is the modal damping of the first model (damping ratio) and $j = \sqrt{-1}$.

Combining Equations (D-1) and (D-2) results in the following expression for the dynamic moment at location k:

$$
\begin{aligned}
DM(h,\omega_i) \\
= M(h,\omega_i) + F_1^*(\omega_i).\left(\frac{\omega_i}{\omega_1}\right)^2 . \frac{\sum_{k=1}^{K} m_k(z_k - h)\phi_1(z_k)}{M_1^*} \cdot \frac{1}{\left(1 - \left(\frac{\omega_i}{\omega_1}\right)^2\right) + 2j\zeta_1\left(\frac{\omega_i}{\omega_1}\right)}.
\end{aligned}
\tag{D-4}
$$

For two identical structures (A and B) with different damping levels, the ratio of the dynamic amplifications is given by Equation (D-5).

$$\frac{[DM(h,\omega_i) - M(h,\omega_i)]_B}{[DM(h,\omega_i) - M(h,\omega_i)]_A} = \frac{\left(1 - \left(\frac{\omega_i}{\omega_1}\right)^2\right) + 2j\zeta_A\left(\frac{\omega_i}{\omega_1}\right)}{\left(1 - \left(\frac{\omega_i}{\omega_1}\right)^2\right) + 2j\zeta_B\left(\frac{\omega_i}{\omega_1}\right)} \tag{D-5}$$

According to Equation (D-5), for locations above the mean sea level, $M(h,\omega_i)$ is zero and the dynamic bending moment will be solely due to inertial forces. However, below the mean sea level a deviation is seen between the ratio of dynamic amplification factors and the dynamic moments as a result of the external wave force moment. To test the deviation of the response of the system from the dynamic amplification factor ratios, as shown in Equation D-5, the offshore wind turbine was simplified and studied as a four degree of freedom system as shown in Figure D-2.
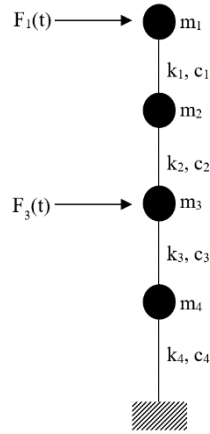
Figure D-2. An example four degree of freedom system with identical masses, springs and dashpots.

For simplicity, this system consists of 4 equal masses which are connected using identical springs and dashpots. The masses, springs and dashpots were tuned so that the system possesses the same first natural frequency as that of the 5MW NREL wind turbine.

The steady state response of the system can be found using Equation D-6.

$$[X] = [D(\omega)]^{-1}[f],$$
(D-6)

where, $[X]$ is the steady-state response amplitude vector, $[D(\omega)]$ is the impedance matrix and is defined in Equation D-7 and $[f]$ is the force amplitude vector assuming that all the external forces are harmonic loads and applied in-sync. An external force was applied to m_1 and at m_3 to represent the wind load and the wave load respectively. Two loading scenarios were considered in this analysis to examine the limitations of the simplified method; only wave load applied and wave and wind loads applied together.

$$[D(\omega)] = ([K] - \omega^2[M] + j\omega[C]),$$
(D-7)

where, $[K]$ is the stiffness matrix, $[M]$ is the mass matrix, $[C]$ is the damping matrix and ω is frequency.

For two structures (A and B) damped at 5% and 8% of critical damping in the first mode, the ratio of the steady state responses was compared with the dynamic amplification factor ratio of the first mode. To obtain these modal damping levels, the dashpot constants were calculated using Equation D-8.

$$\zeta_i = \frac{C_i}{2\sqrt{K_i M_i}},$$
(D-8)

Where C_i, K_i and M_i are the damping, stiffness and mass modal matrices of the system.

Figure D-3 shows the comparison of the dynamic amplification ratio with the steady state response ratio of m_4 (i.e. in an offshore wind turbine this mass would be located below the location of the wave load) for the two loading scenarios considered in this study.
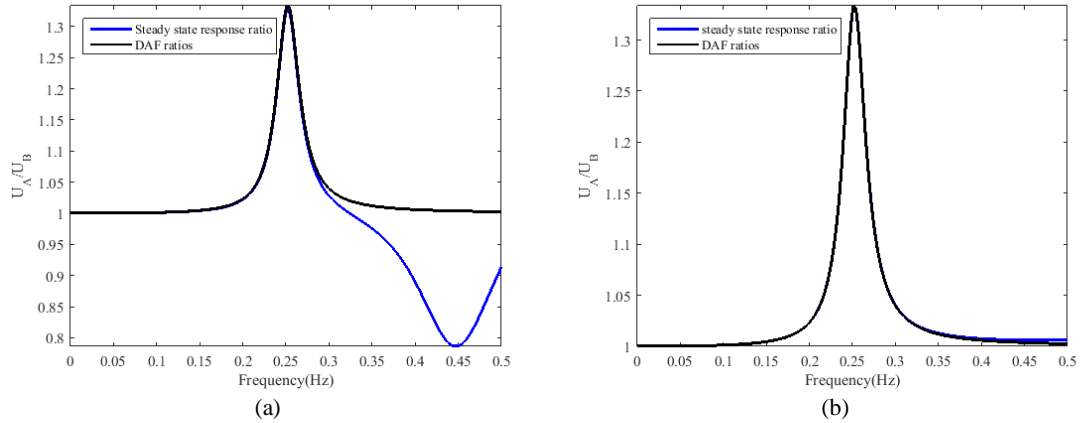

Figure D-3. Comparison of the steady state response ratio of structures A and B with the dynamic amplification factor ratio at m_4 for (a) wave load applied only and (b) wave and wind loads applied.

Figure D-3(a) shows that when only the hydrodynamic load acts on the structure, there is a significant deviation between the dynamic amplification ratio and the steady state response ratio for frequencies above the first mode of the system. However, a close match between the two curves is observed for force frequencies up to and slightly higher than the first natural frequency. The reason for the large deviation was shown and discussed earlier in this section. On the other hand, Figure D-3(b) shows that the consideration of wind load on the structure plays a substantial role as the large deviation seen in Figure D-3(a) is reduced to a marginal amount. As the wind and wave load amplitudes were considered to be equal here, a simple study of the load magnitudes showed that the wave load has to be at least three times the wind load for the deviation to increase to a significant level. Otherwise, the deviation between the steady state response and dynamic amplification ratios appears to be insignificant with the application of the wind load. In an operational offshore wind turbine, the wind load on the structure is always significant compared to the wave load especially for monopile supported offshore wind turbines, which are typically constructed in shallow to intermediate water depth. For an alternative structural configuration, the validity of the simplified method introduced in Chapter 6 can be examined by a similar simplified study conducted in this section.